The University Of Sheffield.

Effects of Gurney Flap on Supercritical and Natural Laminar Flow Transonic Aerofoil Performance

Ho Chun Raybin Yu
March 2015

MPhil Thesis

Department of Mechanical Engineering
The University of Sheffield

Project Supervisor: Prof N. Qin

Thesis submitted to the University of Sheffield in partial fulfilment of the requirements for the degree of Master of Philosophy

Abstract

The aerodynamic effect of a novel combination of a Gurney flap and shockbump on RAE2822 supercritical aerofoil and RAE5243 Natural Laminar Flow (NLF) aerofoil is investigated by solving the two-dimensional steady Reynolds-averaged Navier-Stokes (RANS) equation. The shockbump geometry is predetermined and pre-optimised on a specific designed condition. This study investigated Gurney flap height range from 0.1% to 0.7% aerofoil chord length. The drag benefits of camber modification against a retrofit Gurney flap was also investigated. The results indicate that a Gurney flap has the ability to move shock downstream on both types of aerofoil. A significant lift-to-drag improvement is shown on the RAE2822, however, no improvement is illustrated on the RAE5243 NLF. The results suggest that a Gurney flap may lead to drag reduction in high lift regions, thus, increasing the lift-to-drag ratio before stall.

Dedication

I dedicate this thesis to my beloved grandmother Sandy Yip who passed away during the course of my research, thank you so much for the support, I love you grandma. This difficult journey would not have completed without the deep understanding, support, motivation, encouragement and unconditional love from my beloved parents Maggie and James and my brother Billy. I am indebted to my high school best friend who has supported me over the last few years, Tapiwa Only Chidongo. I would like to thank Ben Hinchliffe, my friend and co-worker, for the entertaining technical discussions, encouragement and support. I would like to express my thanks to friends and colleagues who offered support and guidance through this difficult time.

Acknowledgements

First and foremost, I would like to express my sincere gratitude to my supervisor Prof. Ning Qin for all his encouragement, valuable comments, motivation and advice throughout the research study. I would like to thank Airbus UK and ESPRC for the financial support.

I would like to acknowledge and thank the Advanced Simulation Research Centre for allowing me to perform my simulations on their cluster computer and providing any assistance requested. A big thank you to Nathan Harper for the IT support.

I must also thank my industrial supervisors and Project Co-ordinator from Airbus, Dr Stefano Tursi and Dr Mahbubul Alam and Murray Cross, for the project management and project direction support. I would like to express my deepest gratitude to Ian Whitehouse and Norman Wood, aerodynamics experts from Airbus, for all encouragement and technical support. I have learned so much from you both.

Contents Page

1. Introduction - Problem

In the current, highly competitive and economically uncertain air transport industry, cost is one of the main obstacles. The cost is contributed from several sources, such as fuel price and material cost, of which both are constantly rising. The government also imposes penalties on high greenhouse gas emission. In order to tackle these problems, aircraft with higher fuel efficiency are necessity.

At the cruise condition of a typical airliner the biggest problem is drag. Although these aeroplane are cruising at a transonic region, due to the curvature of the aerofoil, the flow accelerates on the upper surface and results in a velocity higher than Mach 1 over the aerofoil. This causes a shock to form on the wing, which reduces the effectiveness of the aerofoil by wave drag (pressure drag due to compressibility effects) and leads to flow separations.

Shock is a major obstacle during transonic flight, any form of shock alteration (i.e. delay, weakening) is beneficial. This study looked deeply into the application of Gurney flap at the transonic condition. Gurney flap is a well known flow control device in the motor sport industry for drag reduction and down force increment. Its usage is not limited to only the automotive, there are extensive studies demonstrating the benefits of this device for aircraft in take-off and landing configuration, however, there are limited publications available on the transonic condition. In a recent publication, Yu et al (2011)[14] suggested that a Gurney flap may delay shock during cruise.

The main aim of this project is to provide a novel device(s)/system(s) with the means of flow control to reduce drag (especially during cruise condition) and enhance aerodynamic performance. Thus, ultimately providing a positive and beneficial impact to the environment.

1.1 Aim

- Provide a novel solution(s) to tackle the current transonic flow problem and improve aerodynamic performance through the flow control method, with appropriate verification and validation.

1.2 Objectives

- Literature review on the current flow control device/ system, identifying areas which require further development. Conclude with a firm direction of research.

- Investigate, explore and understand the fluid behaviour on the chosen area of flow control. Establish hypothesises with a cause and effects. This includes experimental analysis, verification and validation.

- Explore and develop a novel flow control method/ system for the transonic aerodynamic condition.

- Estimate the beneficial impact and contribution.

1.3 Project Planning

This research project uses a scientific approach to investigate and finalise its results, and Computational Fluid Dynamics (CFD) simulation as the experimental tool. This approach consists of three stages: hypothesis – the predicted and expected outcome, observation – the results/data, analysis – analysis of obtained data and relationship – discussion of the relationship between obtained data and hypothesis.

There are four main, interrelated phases for this research project: the literature review of aerodynamic theory (flow control devices), design, simulation/experiment and optimisation. The initial phase of background investigation provides a solid foundation for the project's directions, goals and aims. The next stage is the design of flow control device(s) and its initial effects prediction. The third stage involves experimental analysis. The final stage is to conclude, validate the proposed predictions and provide optimisation of the design. The overall processes of the project are illustrated in the flow chart below (figure 1.1).

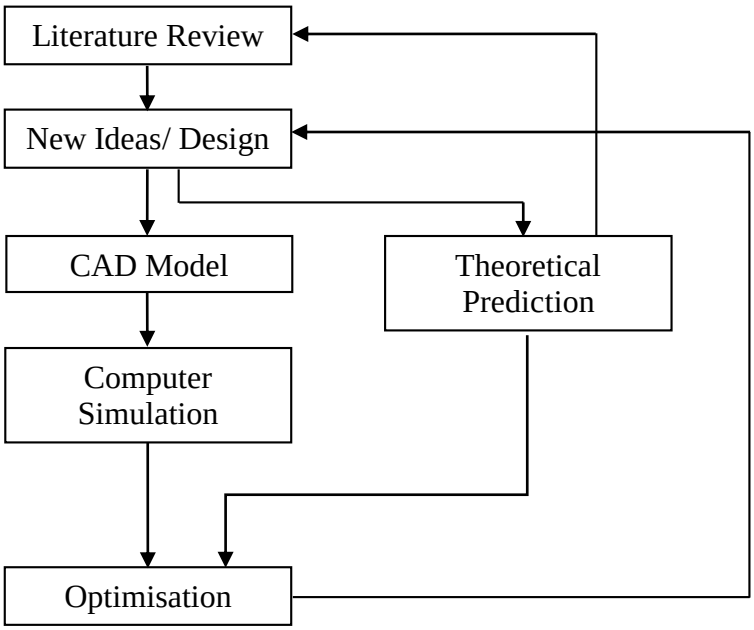

Figure 1.1: Design Process Structure

2. Literature Review

2.1 Flow Control

The topic of flow control is a broad and important subject, it can be defined as the ability to manipulate a flow field (fluid – including liquid and gases) to perform a desired need of beneficial requirement. Flow control can be defined into two main types; Passive and Active. Passive devices are usually a one-off installation and require no external source of power or energy. These devices will only generate the desire effect during the specific designed condition. Therefore, they are cheap to equip but they are not adaptable or flexible in the flow control and causes extra parasitic drag when they are not in use. On the other hand, Active Flow Control system is more flexible and adaptable in all conditions, therefore no or very little parasite drag in undesired condition but cost penalty will occur due to energy consumption. These devices or systems will only perform will the aid of external power/ energy. Therefore, it is necessary to consider that the benefits gained by the effective control device must be greater than the cost required by the device.

In order to achieve the desired performance from a particular flow control device/ system, engineers must pay extra attention to understanding the problem that they encounter. It is important to provide the best method to resolve such undesired flow conditions. Therefore, it is necessary to have a clear motive or goal and have a good knowledge of different types of flow control mechanisms with their possible achievements. [20]Typically, these goals can be categorised into three distinctive topic: Transition Delay/ Advancement, Separation Prevention/ Provocation and Turbulence Suppression/ Enhancement. They all have some degrees of influence features in either Drag Reduction, Lift Enhancement, Mixing Augmentation or Noise Suppression. For a more detailed breakdown of the flow

control classification, energy expenditure and the control loop involved can be used to distinguish.

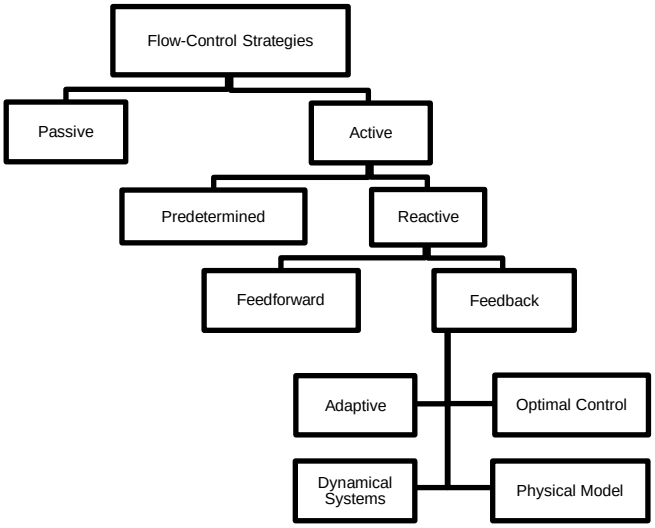

Figure 2.1 [20]Classification of flow-control strategies.

Therefore flow control can be defined as Active and Passive, below is a list of flow control devices for various applications;-

Drag Reduction

- Winglets / Wingtip fences
- Riblets
- Shockbump

Separation Control

- Wing Fences/ Stall Fences/ Boundary Layer Fences/ Vortilon
- Vortex Generators

- Gurney flap
- Passive Suction (Velocity Profile Modifiers – changing the $\left.\frac{\partial^2 u}{\partial y^2}\right|_{y=0}$ to negative)
- Moving walls (turning cylinder)
- Turbulator
- Passive Blowing through leading edge slats and trailing flaps
- Delta Wing

Transition Control

- Wall Motion (Compliant Coating)
- Deturbulator
- Suction
- Shaping => aerofoil profile
- Wall heating/ cooling

Lowering/ affects the near wall viscosity

- Surface heating for liquid/ surface cooling for gas
- Surface-film boiling
- Cavitation
- Sublimation
- Wall injection of lower/ higher viscosity fluid
- Shear thinning/ thickening addictive

Other Flow control devices

- Leading Edge Cuffs
- Stall Strips
- Leading Edge Slat
- Fixed Slot
- Dog tooth leading edge
- Notched leading edge
- Dimples

2.2 Shaping

The wing of an aircraft provides lift, enabling it to fly. Aerofoil is the term used to describe the cross-section shape of a wing. The aerofoil design is critical, any changes to the profile can cause substantial effects on the performance of lift, drag and pressure distribution of the wing.

[39][40]Aerofoil Nomenclature

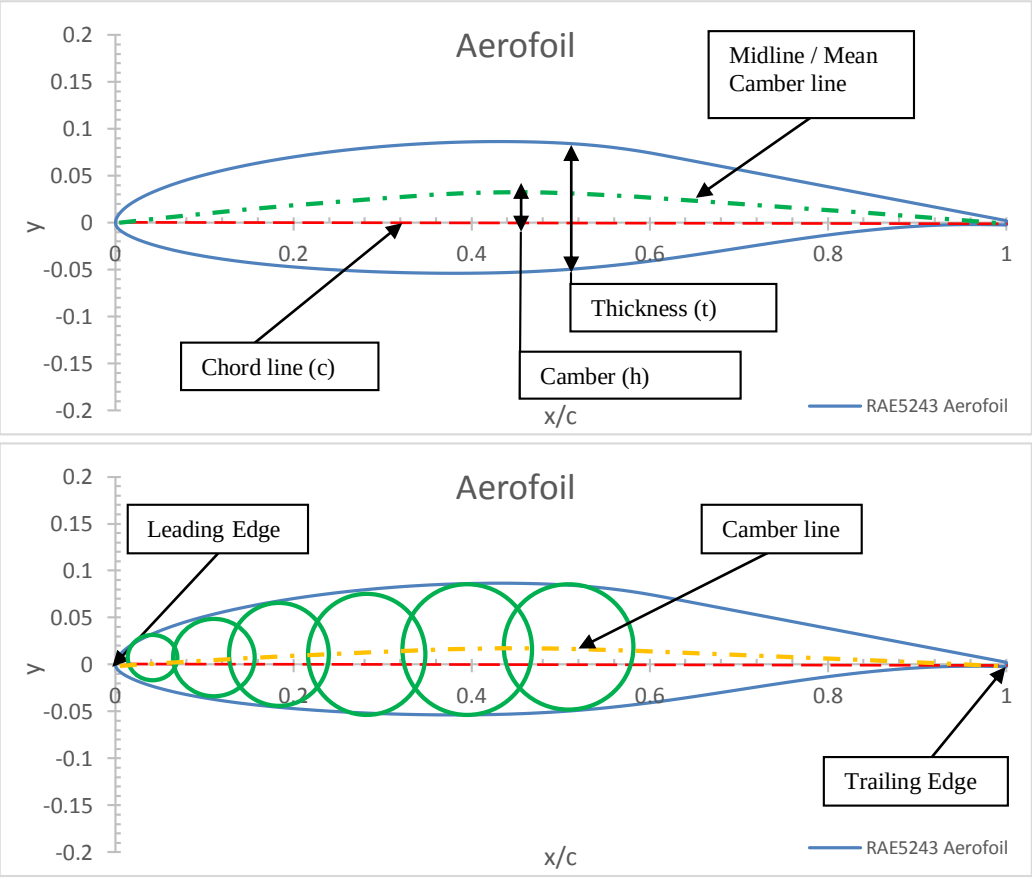

Figure 2.2.1 Aerofoil nomenclature

The front of the aerofoil is called the Leading Edge and rear of the aerofoil is known as the Trailing Edge. The distance between the Leading Edge and Trailing Edge is described as a Chord. The length of the aerofoil, normal to the cross-section from one end to the other, is called the span. The camber of an aerofoil is usually described as a percentage

or a ratio, it is the maximum displacement of mean camber line from the chord (h/c). The Mean Camber Line or Midline is the locus of centre point of the straight lines perpendicular across the chord. Thus, the camber line is the bisector of the aerofoil profile thickness distribution from the leading edge to the trailing edge. The Mean Camber Line or Midline is commonly describe as the Camber Line in some text books.

Transonic Flight Regime

In a transonic flight regime, this is usually between a Mach number of 0.8 to 1.0, this is the condition in which the velocities of flow exist, surrounding and flowing past the aircraft that are concurrently below, at, and above the speed of sound. It is defined as the range of speeds between the critical Mach number, when the local Mach is at or above supersonic and the freestream Mach number remains subsonic.

The term Critical Mach (M_{cr}) describes the freestream Mach number at which a local Mach equal to 1 is first obtained. The aircraft may be flying with a freestream Mach number of less than 1. However, due to the curvature of the aerofoil, the flow is compressed and accelerated. Thus, the local Mach number could be much higher than the freestream velocity. The local peak Mach number is also the point of minimum surface pressure. By travelling above the critical Mach number, the aerofoil will experience localised shock and an increase of pressure drag. For jetliners, thickness-to-chord ratio (t/c) is usually between 0.1 and 0.15. The thinner aerofoil provides a higher critical Mach number.

In the transonic cruise condition, the occurrence of shockwave increases drag of the aerofoil. The sharp pressure increases across the shock, creating a strong adverse pressure

gradient, which results in flow separation. The free-stream Mach number at which C_d begins to increase rapidly is defined as Drag-divergence Mach number ($M_{drag\ divergence}$); $M_{cr} < M_{drag\text{-}divergence} < 1$.

Supercritical Aerofoil

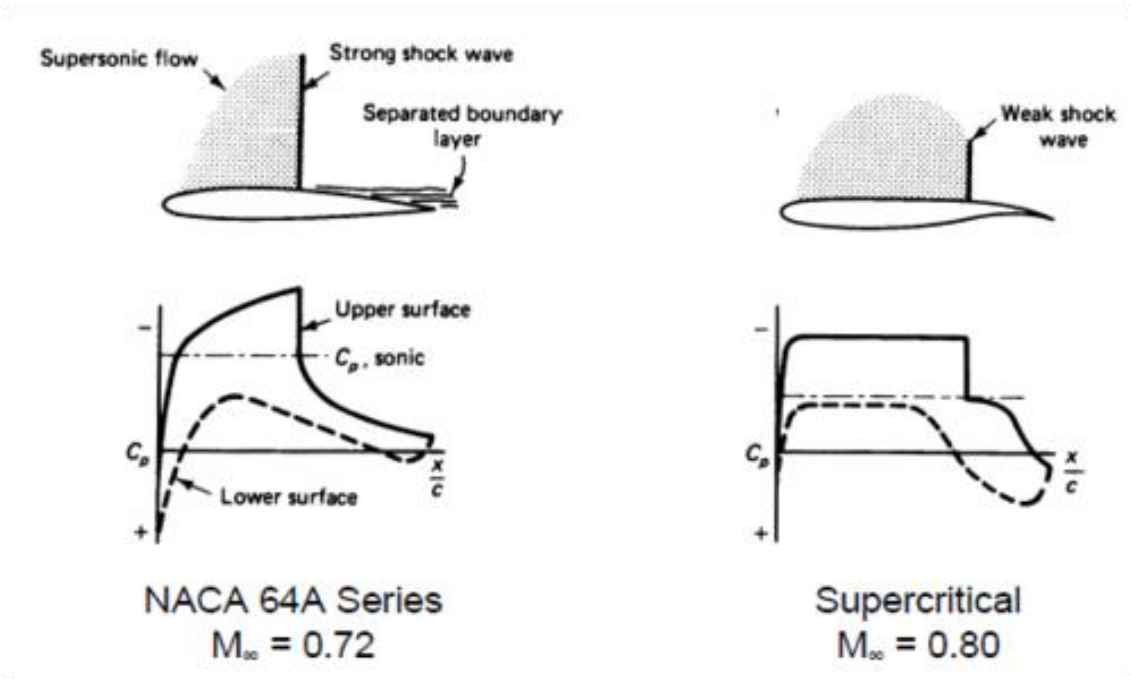

Figure 2.2.2
[21]Conventional vs Supercritical Aerofoil

Supercritical aerofoil is a specially designed aerofoil, targeting performance enhancement at transonic Mach number conditions. Supercritical aerofoil generates less drag in comparison to conventional aerofoil by shaping the pressure distribution. This type of aerofoil features a flatter upper surfaces, which allows a more constant suction to be distributed across the aerofoil, causing a weaker shock and delayed shockwave, hence, drag reduction.

Natural Laminar Flow aerofoil

[20]The Natural Laminar Flow aerofoil (NLF) uses the benefits of lower skin friction at the laminar boundary layer, which implies lower drag. However, its main challenge is to maintain at the laminar boundary layer.

According to the Rutan Voyager's unrefuelled flight, it was equipped with NLF to 50% chord. Depending on the shape, angle of attack, Reynolds number, surface roughness and other factors, the boundary layer either becomes turbulent shortly after the point of minimum pressure or separates first then undergoes transition. There are many limitations to this device, such as: crossflow instabilities and leading edge contamination on swept wings, insect and other particular debris, ice formation, high unit Reynolds numbers at lower cruise altitudes, and performance degradation at higher angles of attack due to the necessarily small leading edge radius of NLF aerofoils.

The boundary layer that is kept laminar to extremely high Reynolds numbers is very sensitive to environmental factors such as roughness, freestream turbulence, radiated sound and so forth. But the flow can be made reliable and durable with careful and conscientious design.

2.3 Gurney Flap

Gurney flap, it is a high lift separation control device; a small simple flat plate positioned perpendicular to the trailing edge of the aerofoil, pointing toward the high pressure surface. Such devices have existed since the 1930s, it was first patented by E.F. Zaparka in the USA[16]. Zaparka not only pioneered the static version but also suggested a movable

version of the mini flap. It was not put into practical use until late 1960s, when Daniel Gurney installed the horizontal plate pointing upward to the rear spoiler end of his Indy 500 cars to increase down force and reduce drag. It also provided additional benefits to cornering and straight-away speed.

Apart from its

application in a conventional fixed wing vehicle, this device is also extensively used in rotary wing aircraft to increase their stabiliser effectiveness. The first helicopter equipped with a Gurney flap was the Sikorsky S-76B; it was installed on the trailing edge of the tail stabiliser (NACA 2414) to promote maximum upward lift [1]. Gurney flaps are also used in wind turbines to increase the output, but the separated unstable flow behind the flap may lead to noise level increment. These examples are all related to low Mach number flows. The Gurney flap was first introduce to aerospace by Liebeck (1978)[2]. Later, Lockheed filed a patent in 1985, claiming that a small wedge flap at the trailing edge improves lifts and reduces drag during cruise condition [18]. The predecessors' work led Henne (1990)[17] into his divergent trailing edge (DTE) invention. Some viewed the DTE as a derivative of the Gurney flap. Such a device was applied to a McDonnel Douglas MD-11 to enhance its transonic performance.

In general, the addition of Gurney flaps will benefit from an increase of the maximum lift coefficient (C_{Lmax}), and decrease the zero lift angle of attack (α_0) [3-8]. But it increases the nose-down pitching moment (C_M) in low angle of attack [3-8]. However, drag may increase and lift may become enhanced, so it is essential to evaluate the aerodynamic efficiency (lift-to-drag ratio).

Gurney flap dimensions are usually described in terms of its height in terms of the chord length. The principle of the Gurney flap operates by altering the Kutta condition at the trailing edge. This is because the flap itself alters the stagnation point at the trailing edge toward the pressure surface, which results in a pressure difference at the trailing edge, and ultimately provides an increase in lift. With the addition of a Gurney flap, two regions of separated flow occur. On the immediate aft the flap laid a pair of counter-rotating vortices, which are alternately shed in a von Kármán Vortex Street. A trapped vortex is also present and shed in front of the flap. (these vortex locations are purely dependent on the angle of incident and flow velocity) Therefore, as a result of this downstream vertical wake, the upper flow (low pressure side) remains attached to the trailing edge, and ultimately reduces flow separation. These vortices were initially predicted by Liebeck et

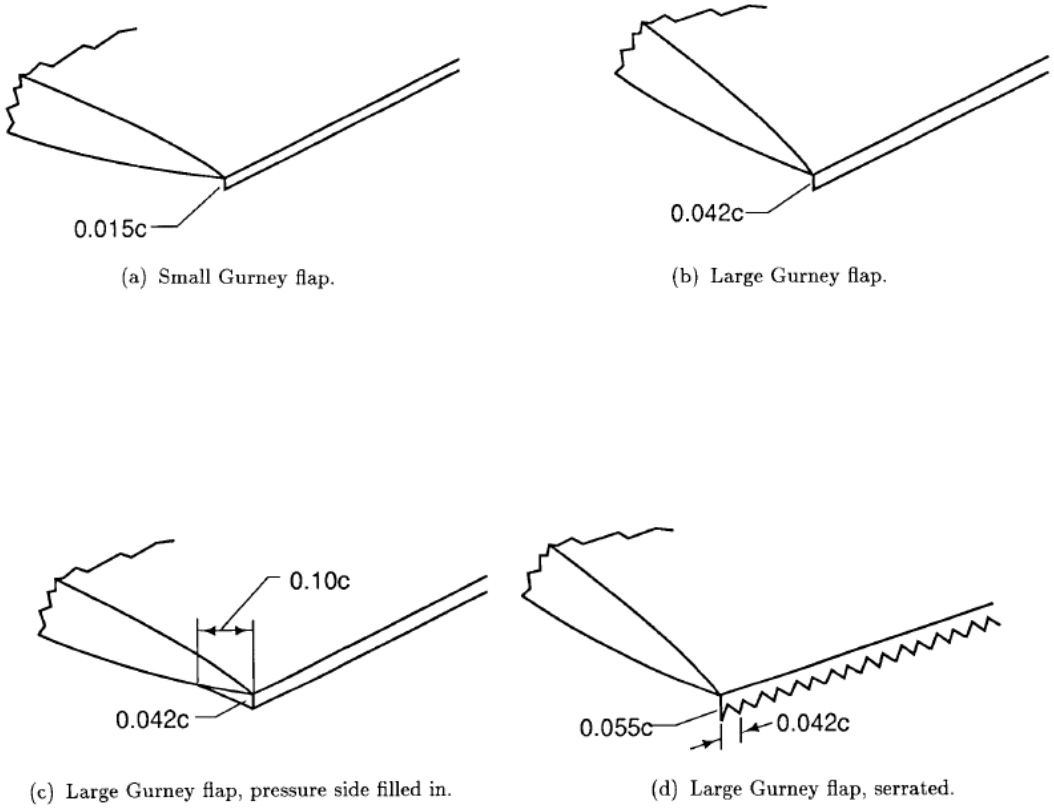

(a) Small Gurney flap.

(b) Large Gurney flap.

(c) Large Gurney flap, pressure side filled in.

(d) Large Gurney flap, serrated.

Figure 2.3.1 [9]Gurney flap models tested.

al (1978) [2], and later validated by NASA (1988) [9] via a low Reynolds Number (Re=8,588) water tunnel, using a NACA 0012 aerofoil with 4 different geometries (Figure 2.3.1). The performance of the Gurney flap will diminish at, or after, the stall region.

This is due to the upper surface flow being fully separated from the trailing edge, and having the Gurney flap positioned in the vortex wake. Therefore, it could provide an influence to the flow around the aerofoil. From their study, it was found that the maximum lift-to-drag ratio can be offered when the Gurney flap height is equal to the boundary layer thickness.

Liebeck et al (1978)[2] concluded that with a 1.25% chord Gurney flap installed on a Newman aerofoil, the lift would increase along with a slight reduction in drag. Larger flap heights were also investigated, which resulted in greater lift increment but were accompanied by the increase of drag. The drag becomes noticeably substantial when flap height exceeds approximately 2% chord. It was noted that separation bubbles occur in the vicinity of the trailing edge at a moderate lift coefficient, or thick trailing edges. Although the water tunnel test of the Gurney flap from NASA (1988)[9] was several orders of magnitude different to Liebeck's initial investigation, the effect was qualitatively agreed. Kroo (1999)[22] suggested Miniature trailing-edge effectors (MiTEs) are a deployable version of Gurney flaps that are located at, or near, the trailing edge of an aerofoil, only to be deployed when required. They are typically segmented into small spanwise elements that can be individually activated. Jeffrey et al. (2000, 2001)[3][4] also validated Liebeck's hypothesis using laser-Doppler measurements at Southampton University (although the trapped vortex was not clearly displayed). The build-up of pressure immediately in front of the flap will result in a reduction of the upper surface (low pressure surface) suction but will produce the same lift. It is believed that the Split and Zap flaps may operate in a similar principle to the Gurney flap, therefore both flow fields are similar.

Based on the experimental study of Storms et al. (1994)[5], it was shown that the maximum lift coefficient was increased from 1.49 to 1.96 by the addition of a Gurney flap to a NACA 4412 aerofoil in low Reynolds Number conditions (Re ~ $2x10^6$). Four

different flap heights were investigated (0.5, 1.0, 1.5 and 2.0% chord) along with two deployable configurations with the hinge line forward of the trailing edge by 1.0 and 1.5 flap heights. The drag coefficient was decreased at the maximum lift condition. But drag increases during low-to-moderate lift coefficients. The results also indicated an additional nose-down pitching moment associated with the increase of Gurney flap height. Therefore, a Gurney flap can effectively promote lift of a single-element aerofoil with very little drag penalty. From the experiment of Bloy et al. (1995)[23], their results showed that the performance of an aerofoil (NACA 63_2-215) with a small 45º trailing edge flap is better than the same aerofoil with a similarly sized Gurney flap. By comparing both flaps we see that, the 45º flap is less prone to drag. From the range of tested specimens, the 2% chord 45º flap offered the highest lift, along with the higher lift-to-drag ratio compared with the entire Gurney flap specimen range. It was concluded that the peak lift-to-drag ratio of 45º flap is comparable to the aerofoil without flap, but offering a high lift coefficient. Bloy et al. (1997)[8] carried out an experimental study of 5 different types full-span 2% chord length trailing edge flaps (45º wedge flap, 45º flap, 90º wedge flap, 90º Gurney flap and square section – Figure 2.3.2) on a NACA 5414 aerofoil at 52m/s with Reynolds number $0.57x10^6$. It was concluded that apart from the 45º flap and 45º wedge flap, which produced slightly less lift enhancement, all the other flaps promoted the maximum lift in a similar manner. The reduced lift promotion of the 45º flap is caused by the 1.4% increase in chord length. This study also showed that the 45º flaps provide a better lift-to-drag ratio across the range of incident angles than a 90º Gurney flap. The lift-to-drag performance of the test section can be enhanced by the 45º wedge flap. The maximum lift-to-drag ratio of the 45º wedge flap is slightly less than the plain aerofoil. Giguere et al. (1995) [24] constructed a variety of experiments and indicated that the optimum Gurney flap height scale was with the pressure surface boundary-layer thickness at trailing edge. The optimisation was carried out in respect to the largest lift-to-drag ratio.

Therefore, in order to achieve to best performance, the Gurney flap should be submerged within the boundary layer. From the optimum height scaling, a very large Gurney flap (10 ~ 20% chord) may be expected at low Reynolds number. Although this can be optimise drag still increases during cruise (low angle of attack). Niu et al. (2010)[25] provided a numerical solution to the unsteady 2D Navier-Stokes equations, coupled with a force-element theory to categorise the individual fluid element contributions in the aerodynamic enhancements from a Gurney flap on a NACA 4412 aerofoil. The numerical study results were compared and validated with Storms et al's. (1994)[5] study. It was indicated that if the Gurney flap is above 2% chord this will result in drastic increases in lift; this is due to the volume and the surface vorticity. The Gurney flap also produces a negative source from the surface vorticity to substantially cancel out the drag coming from the volume vorticity. The lift and drag component is contributed by both volume vorticity and surface vorticity. Although the contribution of volume vorticity is more significant, surface vorticity is the key in lift-to-drag ratio optimisation as it contributes oppositely to both lift and drag.

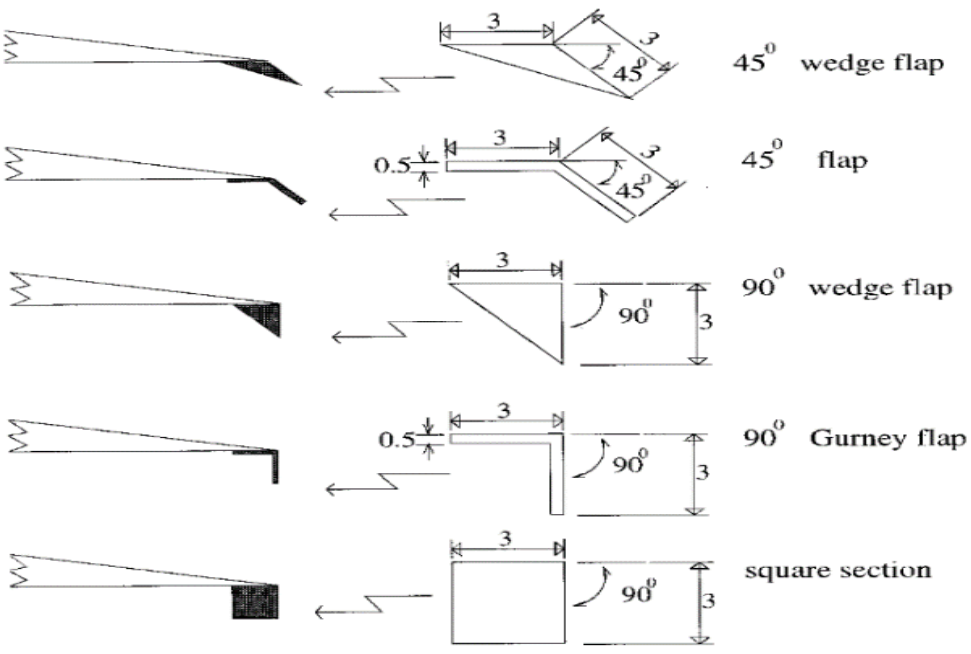

Figure 2.3.2 Dimensions of trailing-edge flaps from Bloy et al. (1997)[8] tested.

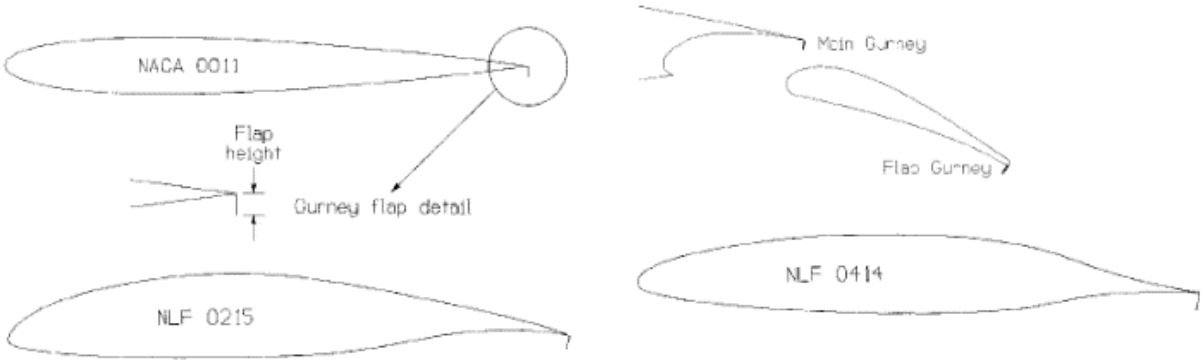

Figure 2.3.3 The selection of aerofoil used in Myose et al. (2008) [26]'s experiment.

The benefits of an additional Gurney flap in three-dimension\s is not as promising as the two-dimensional results. Although the Gurney flap can provide additional lift in all conditions, in the three-dimensional scenario the increase in Gurney flap height is not as effective in extra additional lift coefficient as it is for the two dimensional aerofoil section cases. An extensive low speed wind tunnel analysis on the effect of a Gurney flap on two-dimensional aerofoil, three-dimensional wings and a reflection plane model was studied by Myose et al.(1998)[26]. The study included a traditional high lift device, slotted flap, and addition of a nacelle and fuselage to simulate real life aircraft configuration. There were four different aerofoil sections used in the study. NACA 0011 and cambered GA(W)-2 aerofoil were used for a single-element test, GA(W)-2 aerofoil were also analysed in the two-element test with a 25% chord slotted flap along with a deflection of 10^{o}, 20^{o} and 30^{o}. The following two are used in the three-dimensional analysis, A NLF 0414 straight wing with different spanwise location (inboard, outboard, midspan, full and clean) and length of Gurney flaps and a tapered NLF 0215 was mounted with a fuselage and nacelle. The Gurney flap was attached to the trailing edge for all cases, and at in the slotted flap scenario, the Gurney flap attached to the main aerofoil and the flap itself. Figure 2.3.3 refers to the aerofoil layout. Figure 2.3.4 describes the test conditions, including Reynolds number. By comparison with the baseline of clean aerofoil, evidence shows that the Gurney flap enhanced the maximum lift. But drag penalty occurs,

associated with lift addition. The Gurney flap located at the gap between the slotted flap (trailing edge element) showed very little performance improvement. On the other hand, positioning the Gurney flap at the slotted flap showed a much larger improvement in lift. From the Gurney flap spanwise positioning analysis of the NLF 0414 showed that the length of the Gurney flap increases the lift and drag linearly, but there are very little effects in different positions. It is interesting to note that, the three-dimensional analysis of NLF 0215 tapered wing with both 1.2% chord and 2.5% chord height Gurney flap experienced almost identical lift and drag increase throughout the range of alpha. The same characteristics were also displayed for the reflective wing model (NLF 0215 + fuselage + nacelle).

Configuration	q, lb/ft^2	Chord Reynolds no.	Mach no.	α range, typical increment	Gurney height, % chord
NACA 0011 symmetric	25	2.2×10^6	0.13	−2 to +20, 1 deg	1, 2, 4
GA(W)-2 two-element	35	2.3×10^6	0.16	−8 to +16, 1, deg	1
NLF 0414 straight	20	1.2×10^6	0.12	−6 to +29, 1, deg	1.7, 3.3
three-dimensional	50	1.6×10^6	0.19	——	——
NLF 0215 tapered	25	0.9×10^6	0.13	−10 to +24, 2, deg	1.2, 2.5
three-dimensional		(mean chord)			(% mean chord)

Figure 2.3.4 The Gurney flap test condition in Myose et al. (1998)[17] ' study.

The wake stabilization technique was used in an attempt to reduce the drag penalty caused by the addition of the Gurney flap. In Meyer et al.(2006)[7]'s study, they concluded that the three-dimensional Gurney flap clearly shows drag reduction. They applied slits, holes and vortex generators individually to the Gurney flap as a wake stabilization device. Both numerical simulations and wind tunnel experiments were conducted. There were three different wings (laminar glider aerofoil, High lift profile and a simplified swept constant chord half model with typical airliner sections) used in the investigation, all with Reynolds number of 1.0×10^6 and a Gurney flap height of 0.67% chord. From the slits

analysis, it shows that the absolute wake instability which was caused by the buff trailing-edge was almost completely disappeared. The additional slits led to a significant of 25% decrease in drag. But the lift is slightly reduced due to the bleed air through the slits, which made the flap to appear smaller. Nevertheless, at large incidents, the improvement from the slits is less noticeable. This is because during high incident, the wake from the aerofoil became strongly asymmetric. Therefore, the drag cannot be further reduced by instability suppression in the wake. Interestingly, as the absolute instability of the wake reduced, the wing flutter and noise levels are also reduced. But despite the advantage of drag reduction from slits, there are penalties; the Gurney flap becomes less rigid and loses its stiffness. The addition of holes in the Gurney flap retains the mechanical stiffness and reduces drag. From Meyer et al's. (2006)[7] results, it showed that the flap with additional holes displayed a better perform drag polar than the convectional full Gurney flap. There was slightly less extra lift generated than with a conventional Gurney flap, this is due to the bleed air. Although the wake instability elimination was not as thorough as the slit specimen, it is good enough to cause a substantial amount of drag reduction. Vortex generators (VGs) were also used as a drag reduction device by the means disturbing the periodic flow field in the wake caused by the Gurney flap. The geometry of the VGs Gurney flap may be found in figure 2.3.5. As shown from the diagram, there are two rows of VGs, upper and bottom surface. Because of such positioning, the wake of the Gurney flap is altered in such a way that the periodic separation should no longer appear. There is no centre disturbance caused, but only upper and lower edge, which is fairly different to the holes and slits scenario. With the addition of VGs, there are no benefits to maximum lift, but a slight reduction in drag. Therefore,

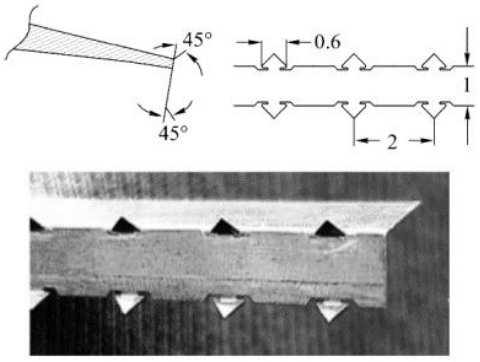

Figure 2.3.5[7] The Gurney flap with vortex generators.

this provides an efficient improvement of 0.001 reductions in minimum drag coefficient when compared with the clean Gurney flap.

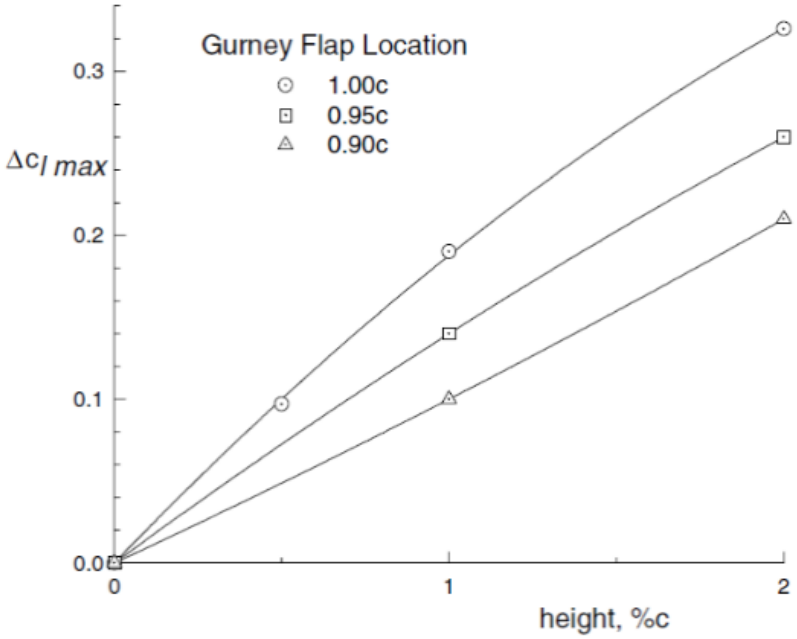

Figure 2.3.6 [27] Change in maximum lift coefficient with varying Gurney flap heights and chordwise locations. Maughmer et al. (2008)

A two-dimensional study on various chordwise positions and heights of Gurney flaps were looked at by Maughmer et al. (2008)[27]. The study consists of both wind tunnel and computational fluid dynamic analyses. The specimen used was a 12%-thick S903 aerofoil, the S903 section is specially design for laminar flow condition. The experiment consisted of 3 variables in chordwise locations of 0.90 chord, 0.95 chord and 1.00 chord, and 3 variable flap height of 0.5% chord, 1% chord and 2% chord, altogether of 9 different configurations. The investigation was carried out in a low speed, low turbulence wind tunnel, the test were run at 150ft/s (45.72m/s) with a chord Reynolds number of $1.0x10^6$. Two cases were looked at: extended laminar-flow and fixed-transition. The study concluded that at a higher angle of incident, the influence of the Gurney flap spread

increasingly forward. This meant more lift was generated due to a reduced recovery of adverse gradients on the suction surface, therefore pushing the point of flow separation to the aft of the aerofoil. For the extended laminar-flow condition, the minimum drag varies almost linearly with the Gurney flap height, but the flap location has less influence on the drag component. On the other hand, for the fixed-transition condition, the increase in drag due to the Gurney flap is less critical. The alterated chordwise position of the Gurney flap had very little difference on the drag cause when compared with the flap placed at the end of the trailing edge, but the maximum extra lift generated is reduced and moved further in toward the aerofoil. This means the lift-to-drag ratio is actually reduced with position shifted away from the trailing edge. Figure 2.3.6 indicates that as the flap positioned got closer to the maximum chord, a higher maximum lift was shown.

A study on perforated Gurney flap on NACA 0012 aerofoil was conducted by Lee (2009)[28], in an attempt to reduce the induced drag. The experiment was carried out at a low speed wind tunnel, with a Reynolds number of 0.232×10^6. Extensive amounts of Gurney flap height (1.6%, 3.2%, 5.5%, 6.7%, 8.8%, 10% and 12% chord) and porosities (0%, 23%, 40% and 50%, based on the open to closed area of the flap surface) were investigated. It was shown that by comparing with the convectional flap, the perforation significantly reduced the wake size and unsteadiness compared with the solid flap. The experimental data indicated that the perforated flap has a better stall angle delay characteristic than a solid flap. The stall angle was delayed to 11.5^o, 11.8^o and 12.7^o with perforation porosities of 23%, 40% and 50% respectively, in contrast with a solid flap the stall angle is only 10.7^o. The suction surface pressure recovery is enhanced by the perforation. This is due to the disruption of the wake flow behind the flap by jet flow induced by the perforation. This effect also reduced the flap-induced camber effects. In

comparison to the convectional Gurney flap, the perforated flap showed an increase in adverse pressure at the trailing edge location, and induced an earlier boundary-layer separation from the suction surface. Both suction surface pressure and lower surface pressure experienced a reduction as the porosities increases. The increase of porosities will reduce the extent and the near wake intensity/ size, and also the velocity deficit. This also led to a weaker fluctuating intensity. The perforation condition led to lift reduction but a reduced nose-down pitching moment in comparison with a non-perforation flap. As the perforation intensity increases, the maximum lift coefficient, drag coefficient and maximum nose-down pitching moment coefficient also decreases. The lift decrement of the flap is caused by the reduction in trailing edge loading. But it is very important to note that the decrease in drag is more than the loss in lift, therefore, the perforated flap will lead to more efficiency (higher lift-to-drag ratio) than the conventional Gurney flap.

Beijing University of Aeronautics and Astronautics (2009)[11] investigated the effects of a plasma actuator Gurney flap (Figure 2.3.7) on a NACA 0012 aerofoil by solving the Reynolds-averaged Navier-Stokes equation (RANS). The chord length of the aerofoil is 1m and the freestream velocity is 10m/s, with a Reynolds number of 0.684×10^6. The plasma actuator is modelled by adding body-force source term to the momentum equations. The inspiration of this novel device is to solve or reduce the problem of the induced drag caused by the Gurney flap. This is because the use of a static Gurney flap will always produce parasitic drag and never retain the same drag coefficient as a clean aerofoil. The construction of this plasma actuator Gurney flap consisted of a typical single dielectric-barrier discharge (SDBD) plasma actuator placed vertically to the 0.3% chord (3mm)

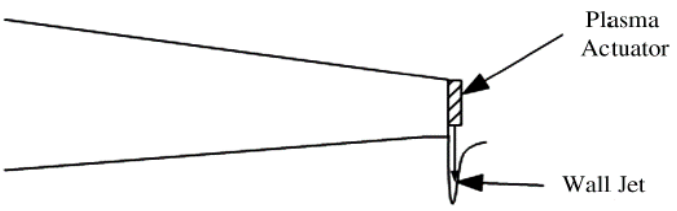

Figure 2.3.7 [11]Plasma Actuator Gurney Flap.

thickness trailing edge. The strength of the plasma actuator is represented by a non-dimensional parameter D_c (this is a representation of the electrical force to the inertial force). A plasma actuator strength of $D_c = 9.14$ was investigated. When the plasma actuator is switch on, its motion will generate a jet stream vertically downward. This device effectively acts just like the jet Gurney flap but without the complication of mechanical blowing systems.

From their verification analysis (in lift and pitching moment) with previous research, it was suggested that the plasma actuator Gurney flap with the strength of $D_c = 9.14$ is equivalent to a 0.78% chord conventional Gurney flap and a jet Gurney flap with the blowing momentum coefficient $C_\mu \approx 0.01$. The results suggested that the plasma Gurney flap performs the same way as a conventional Gurney flap, with enhanced maximum lift and nose-down pitching moment, but with less drag penalty. In comparison to the jet Gurney flap, the plasma Gurney flap produces the function but with additional benefits of no moving parts, very fast action and more flexibility. The flow pattern and the loading variation on the aerofoil obtained from the plasma flap are very similar to the conventional Gurney flap. The reduction of drag penalty is due to the disappearance of the von Karman vortex street downstream of the trailing edge. Therefore, the aerofoil efficiency is improved; achieving a higher lift-to-drag ratio. Also, similar stall ineffectiveness is also identified in the plasma actuator flap, but it was suggested that its performance can be improved during post stall by means of an unsteady plasma Gurney flap, it must act according to the aerofoil's separated vortex-shedding frequency and the shear-layer instability frequency. But this required further investigation to verify the improvement suggestion.

A recent study by Schuele et al. (2010)[10] looked at the high lift flow control behaviour with a combination of dielectric barrier discharge (DBD) plasma actuators and the addition of a Gurney flap. The investigation was conducted at very low Reynolds numbers of 3,000< Re< 20,000 on a flat and 8% camber plate. In the experiment, DBD was installed at the leading edge as an active device. A 10% and 20% chord Gurney flap was employed at the trailing edge as a passive device. It is an alternative form of jet Gurney flap. Their flap consists of a plasma actuator on the trailing edge. When the actuator is switched on, a fast jet will be induced. The DBD plasma actuators are to promote the maximum lift coefficient and increase the stall angle. Therefore, the combined effect for both controller devices is a cumulative one; the DBD actuators stall delaying mechanism was also effective in the passively controlled case. The result indicated that from the conventional semi-empirical models to the very low Reynolds number, the large Gurney flap (10% chord) provided a 20% increase in the maximum lift and an improvement in aerofoil efficiency. It was concluded that a Gurney flap generates better improvement in lift-to-drag ratios at low Reynolds numbers, but the plasma actuators were enhanced at higher Reynolds numbers.

Rosemann et al (2003)[18] from DLR investigated the effects on a Gurney flap and divergent trailing edge on VC-opt aerofoil for transonic condition, M = 0.755, Re = $5x10^6$. The flap heights studied were 0.25%C, 0.50%C, 0.75%C and 1.00%C. Their results suggested increases of drag at a small angle of attack, but at high lift regions it lead to a significant drag reduction. It was observed that the effect on pressure distribution is the development of pressure difference between upper and lower surfaces by the modified flow condition at the trailing edge. Shock was also shown to have been delayed and is more resistant to separation.

The transonic performance of supercritical aerofoil (RAE2822) with a Gurney flap was investigated by Yu et al (2011) [22]. Their results suggested that with the aid of a Gurney flap, the shock wave position shifted backward on the suction surface at the same incident angle and created a wider supersonic region, which significantly increases the lift coefficient. The lift-to-drag ratio also benefited, with a 10.7% increase in maximum L/D for a flap h = 0.25% chord length.

From the reviews shown, Gurney flaps can be employed at the trailing edge with a guaranteed lift increment at the same angle of attack, but they are accompanied by drag penalties. All variants of the Gurney flap displayed a lift enhancement effect. However, most of these studies were all conducted in low speed and low Reynolds conditions. [8]NASA (1988) suggested that altering aerofoil camber, thickness (increase) may lead to drag reduction. The drag penalty is mostly introduced by the flow separation downstream of the trailing edge. This device can be very important to high lift configurations, as a very small device with little weight can enhance a substantial amount of lift. The weight reduction of traditional high lift devices can lead to less design and manufacturing complexity. Also, this can be deployed during cruise conditions, as lift increases greater loads can be transported and a reduced thrust is needed to maintain the lift. Ultimately, this can provide a large saving in cost. This can also be a safety feature, with studies showing that a Gurney flap may lead to a delayed stall angle. There are various ways to enhance the aerodynamic efficiency of a Gurney flap: a less than 0.5% chord for the flap height, a plasma actuator jet flap and perforated Gurney flap. The work of a plasma Gurney flap can be expanded, as it requires very little energy input and it is rapid, efficient (small drag penalty) and flexible. The combination of jet and perforated Gurney flaps can be quite interesting.

3. Research Methodology

3.1 Research Methodology

In the broad subject of aerodynamics, in particular for transonic aircraft aerodynamics, flow behaviours may be analysed in three different ways: Wind Tunnel testing, Numerical Simulations and actual Flight Tests. Wind Tunnel testing existed over 100 years ago; it is a way for scientists to simulate flow on the ground in a controlled manner. The wind tunnel consists of a converging and diverging nozzle to obtain the desired flow velocity and a working section where the model is placed for testing. This type of analysis often provides a good estimation of what is happening to the flow and surrounding conditions. Nevertheless, it requires a high manufacturing cost for an accurate model. During transonic cruise conditions, the Reynolds number is often very high and a cryogenic wind tunnel may be used to replicate high Reynolds number conditions. This will often associate with the penalty of high maintenance and running costs. During the test, models are mounted on a controller to adjust its angle of attack, and the support rod/ controller may cause a disruption to the flow, and may lead to inaccurate results. Not to the mention that the wall effects and turbulence intensity of the wind tunnel are very different to actual flight conditions. On the other hand, Numerical Simulations, often referred to as CFD (Computational Fluid Dynamics), provide a solution by solving the governing equation, and a specific turbulence model. The CAD model is required, then grids/mesh are added to the surroundings and the calculation is based on the grid. This method is clean and easy to implement into different flow conditions, turbulent intensity can be adjusted and wall effects can be neglected, but it may require high computational costs for large calculations. Both wind tunnel testing and CFD calculation can only produce a ‘very good’ replica of what is happening in real life situations. This is because during real flight the weather is

constantly changing which affects temperatures, density, pressures and causes wind, gust and turbulence. These variables are neglected in both simulations. The most accurate evaluation is a flight test. This is usually the final stage of evaluation after extensive hours of CFD and wind tunnel studies. This is the most crucial part as this will give an indication of what is actually happening during the cruise condition. It is also very dangerous for the pilots and engineers on board as the aircraft/ aerodynamic modification are in the air for the first time.

A density based RANS 2nd order finite volume flow solver, TAU, was used to tackle the fluid problem throughout this report. Geometries/models are constructed and prepared through RAVEn. Unstructured mesh are used throughout the study and are generated by SOLAR. The software are accessed remotely via VPN connection to the cluster at ASRC (Advanced Simulation Research Centre, Bristol, United Kingdom). The simulations and mesh generations were performed on the HPC (High Performance Computer) cluster.

Shock is a major obstacle during transonic flight, inducing wave drag, potential flow separation and sudden drag rise. Therefore any means of controlling/weakening/altering the shock wave for transonic wings is of strong interest. This project emphasised the behaviour of 2D transonic aerodynamics. This report is split into two interrelated fundamental bases: Supercritical aerofoil – RAE2822 and Natural Laminar Flow (NLF) aerofoil RAE5243. Each is then subdivided into further detailed investigation. Both supercritical and NLF cases are initiated through solver and mesh verification, followed by wind tunnel data validation.

This project is highly focused on the aerodynamics behaviour triggered by a Gurney flap at transonic conditions. Investigations such as lift constraint studies, Gurney flap vs

camber line alteration, shockbump vs Gurney flap and the deflection of the Gurney flap are discussed in this report.

3.2 Governing Equation[31]

The Navier-Stokes equation is the governing equations of CFD. The equation is derived from the conversation law of the physical properties of fluid; mass, energy and momentum.

The Navier-Stokes equations for the three dimensional case can be written in conservative form as

$$\frac{\partial}{\partial t}\iiint_V \vec{W} dV = -\iint_{\partial V} \bar{\bar{F}} \cdot \vec{n} dS \tag{3}$$

$$\vec{W} = \begin{pmatrix} \rho \\ \rho u \\ \rho v \\ \rho w \\ \rho E \end{pmatrix}$$

Where *t* is the time, *V* denotes an arbitrary control volume with the boundary ∂V and the outer normal vector $\vec{n}$. The $\vec{W}$ is the vector of the conserved quantities. The density is represented as ρ, E as the internal energy and u, v, w are the velocities in x, y, z coordinate directions.

The flux density tensor, $\bar{\bar{F}}$, is composed of flux vectors in the three coordinate directions;

$$\bar{\bar{F}} = \left(\vec{F}_i^c + \vec{F}_v^c\right) \cdot \vec{e}_x + \left(\vec{G}_i^c + \vec{G}_v^c\right) \cdot \vec{e}_y + \left(\vec{H}_i^c + \vec{H}_v^c\right) \cdot \vec{e}_z \tag{4}$$

The $\vec{F}^c, \vec{G}^c, \vec{H}^c$ denotes Flux vectors and superscript c represents Corrective. The e_x, e_y and e_z are unit vectors in the coordinate directions. The indices *i* and *v* denote the inviscid and viscous contributions respectively. The viscous contributions are neglected when considering the Euler equations. The viscous and the inviscid fluxes are;-

$$\vec{F}_i^c = \begin{pmatrix} \rho u \\ \rho u^2 + p \\ \rho uv \\ \rho uw \\ \rho Hu \end{pmatrix}, \vec{F}_v^c = \begin{pmatrix} 0 \\ \tau_{xx} \\ \tau_{xy} \\ \tau_{xz} \\ u\tau_{xx} + v\tau_{xy} + w\tau_{xz} + \kappa_l \frac{\partial T}{\partial x} \end{pmatrix} \tag{5}$$

$$\vec{G}_i^c = \begin{pmatrix} \rho v \\ \rho uv \\ \rho v^2 + p \\ \rho vw \\ \rho Hv \end{pmatrix}, \vec{G}_v^c = \begin{pmatrix} 0 \\ \tau_{xy} \\ \tau_{yy} \\ \tau_{yz} \\ u\tau_{xz} + v\tau_{yy} + w\tau_{yz} + \kappa_l \frac{\partial T}{\partial y} \end{pmatrix} \tag{6}$$

$$\vec{H}_i^c = \begin{pmatrix} \rho w \\ \rho uw \\ \rho vw \\ \rho w^2 + p \\ \rho Hw \end{pmatrix}, \vec{H}_v^c = \begin{pmatrix} 0 \\ \tau_{xz} \\ \tau_{yz} \\ \tau_{xx} \\ u\tau_{xz} + v\tau_{yz} + w\tau_{zz} + \kappa_l \frac{\partial T}{\partial z} \end{pmatrix} \tag{7}$$

The pressure is determined by the equation of state;-

$$p = (\gamma - 1)\rho\left(E - \frac{u^2+v^2+w^2}{2}\right) \tag{8}$$

The temporal change of the conservative variables $\overrightarrow{W}$ from equation 3 can be derived from;-

$$\frac{\partial}{\partial t}\overrightarrow{W} = -\frac{\iint_{\partial V} \bar{\bar{F}} \cdot \vec{n} dS}{\iiint_V dV} \tag{9}$$

The change of the flow conditions in a control volume V is given by the flux over the control volume boundary ∂V related to the size of V. For a control volume fixed in time and space, the equation (9) can be written as;-

$$\frac{d}{dt}\overrightarrow{W} = -\frac{1}{V}\cdot\vec{Q}^{F} \tag{10}$$

The $\vec{Q}^{F}$ represents the fluxes over the boundaries of the control volume. If the boundary is divided into n faces, then $\vec{Q}^{F}$ can be represented a;-

$$\vec{Q}^{F} = \sum_{i=1}^{n}\vec{Q}_{i}^{F} = \sum_{i=1}^{n}\left(\vec{Q}_{i}^{F,c} - \vec{D}_{i}\ \right) \tag{11}$$

The term $\vec{Q}_{i}^{F,c}$ denotes the inviscid fluxes over the respective face. Hence, in order to determine the temporal change of the flow quantities in a control volume, the convective fluxes over the control volume boundaries have to be determined. For upwind schemes the dissipative terms $\vec{D}_{j}$ are zero, but for central schemes additional dissipative terms have to be computed.

3.3 Numerical Method[31]

The basis of the numerical investigation throughout this thesis is performed by DLR TAU flow solver. The DLR TAU code was developed by *Deutsches Zentrum für Luft- und Raumfahrt e.V.* (German Aerospace Center), it was originally created for subsonic and transonic flow and validated for complex configurations under such Mach ranges. The code itself is well established and widely used as a general purpose tool for a wide range

of aerodynamic and aero-thermodynamic problems. The solver enables one to handle viscous flow around complex objects, from subsonic conditions to hypersonic flow regimes. TAU code has the ability to couple with other disciplines which enables it to perform complex multidisciplinary simulations. The Reynolds averaged Navier-Stokes (RANS) equations are discretised by a finite volume technique via tetrahedra, pyramids, prisms and hexahedra mesh. Prismatic elements are used for the boundary layer while tetrahedra mesh are used in inviscid flow regions.

The TAU flow solver is a three-dimensional, parallel, hybrid, multi-grid code. It is implemented in a finite volume scheme for solving the compressible time-accurate Reynolds-averaged Navier-Stokes (RANS) equations. The numerical scheme is based on a second order finite volume formulation, where inviscid terms are computed employing either a central scheme with scalar or matrix artificial dissipation or a variety of upwind schemes using linear reconstruction. The flow variables are stored on the vertices of the initial grid. This type of spatial discretization is called ‘cell vertex’ with a dual metric which is computed during the pre-processing step. The TAU code uses explicit time stepping, the multi-step Runge-Kutta scheme and implicit time stepping with a LU-time scheme. In terms of accelerating the convergence to a steady state, a local time-stepping concept, a different residual smoothing algorithm and a geometrical multi-grid method are implemented.

The fluxes calculation may be determined by either an upwind or a central scheme. There are several flux discretization functions available in an upwind scheme: Van Leer, AUSMDV, AUSMP, Roe, AUSM Van Leer, EFM and MAPS+. The central method has two different dissipation models: scalar dissipation and matrix dissipation. The viscous fluxes for the one equation turbulence models with central schemes are discretised using

central difference. In the two equation models, the central scheme uses an upwind version discretisation for their viscous fluxes.

The pre-processor generates a data structure which enables the solver to perform simultaneously in several sub-domains. In a time-accurate simulation, a global as well as a dual time-stepping scheme are implemented. The dual time stepping scheme follows the Jameson Scheme approach, in which the Runge-Kutta scheme is slightly modified to avoid instabilities while dealing with small physical time steps. The time using dual-time discretisation can be chosen to be first, second or third order.

The turbulence model implemented in the supercritical aerofoil study is the one-equation transport model according to the Spalart-Allmaras model (SA)[32]. The model uses only local quantities for calculating turbulent transport, which makes it suitable for unstructured methods. The SA model is robust, efficient and able to handle various flowfield; including scenarios in which small flow separation and reattachment occur. In this model, the eddy viscosity is directly determined from the single transport equation. The model has been examined extensively. In the high-lift condition, the SA model performs similarly to higher-order models and better than algebraic and other one-equation models [33]. However, in the Natural Laminar Flow aerofoil study the reference uses a 2 equation model. Therefore, in addition to the one-equation SA model, a 2 equation k-ω Linearized Explicit Algebraic Stress Model was also used in the investigation and for validation purposes.

Lift Constrained Simulations

This study looked at the Gurney Flap's performance and behaviour from the prospective different angle of attack, Mach number and geometrical modification. However, the

performance comparison is not true if the angle of attack is selected as a base / constant and drag is a variable. This is because the lift force may differ even it is at the same angle of attack. The lift constrained simulation was introduced to this investigation, the lift force will remained constant and other aerodynamics parameter will differ. This makes the comparison true and feasible. The aerofoil/geometry will be set at its desired lift coefficient. Prior to lift constrained simulation, a set of different angle attack aerodynamics data must be obtained. Based on the desired lift coefficient required, the input angle of attack can be roughly estimated through the data previously obtained. The principle of the lift constrained simulation is that the simulation is split into two sections: fixed iteration and auto iteration. The fixed iteration is basically the angle of attack manually inserted, the calculation continuous until the convergence criteria archives. Once, the convergence requirement is met, the auto iteration of the angle will start. The angle iteration calculation is done in steps, it will continue to fluctuate until the desired lift coefficient and convergence criteria are met.

Example of the lift constrain output.

```
 Markers: 3
      Type: farfield
Angle alpha (degree): 2.75
Constant alpha/clift (0/1): 1
Targeted clift: 0.81
Lift iteration period: 200
Lift iteration start: 10000
      Name: FARFIELD_ZONE
                        Angle alpha (degree): 2.7657
                        Angle alpha (degree): 2.7805
                        Angle alpha (degree): 2.79399
                        Angle alpha (degree): 2.80599
                        Angle alpha (degree): 2.81657
                        Angle alpha (degree): 2.82588
                        Angle alpha (degree): 2.834
                        Angle alpha (degree): 2.84116
                        Angle alpha (degree): 2.84749
```

Angle alpha (degree): 2.85313
Angle alpha (degree): 2.85817
Angle alpha (degree): 2.86275
Angle alpha (degree): 2.86692
Angle alpha (degree): 2.87071
Angle alpha (degree): 2.87421
Angle alpha (degree): 2.87743
Angle alpha (degree): 2.88041
Angle alpha (degree): 2.88314
Angle alpha (degree): 2.88564
Angle alpha (degree): 2.88794
Angle alpha (degree): 2.89003
Angle alpha (degree): 2.89195
Angle alpha (degree): 2.8937
Angle alpha (degree): 2.8953
Angle alpha (degree): 2.89676
Angle alpha (degree): 2.8981
Angle alpha (degree): 2.89933
Angle alpha (degree): 2.90045
Angle alpha (degree): 2.90149
Angle alpha (degree): 2.90244
Angle alpha (degree): 2.90332
Angle alpha (degree): 2.90413
Angle alpha (degree): 2.90487
Angle alpha (degree): 2.90555
Angle alpha (degree): 2.90618
Angle alpha (degree): 2.90676

block end

Flow Solver Setting

Below is the extract of the setting file used in this study for TAU code.

SOLVER

Inviscid flux discretization type:	Upwind
Central dissipation scheme:	Scalar_dissipation
Coarse grid upwind flux:	Van_Leer
Upwind flux:	AUSMDV
Reconstruction of gradients:	Least_square

Relaxation ----------: -

Relaxation solver:	Backward_Euler

Backward Euler ----------: -

Linear solver:	Lusgs

Linear preconditioner: (none)
Implicit overrelaxation omega: 1.0
Implicit overrelaxation beta: 1

LUSGS ----------: -
Sgs stages maximum: 3
Lusgs increased parallel communication (0/1): 1
Lusgs treat whirl implicitly (0/1): 0
Order of upwind flux (1-2): 2
Order of additional equations (1-2): 1
Increase memory (0/1): 1
Solver/Dissipation ----------: -
Matrix dissipation terms coefficient: 0.5
2nd order dissipation coefficient: 0.5
Inverse 4th order dissipation coefficient: 64
Ausm scheme dissipation: 0.25
Limiter freezing convergence: 0
Preconditioning: (none)
Cut-off value: 1.5

Timestepping Start/Stop ----------: -
Output period: 100000
Maximal time step number: 100000
Minimum residual: 1e-6
Matching iteration period: 10

Timestep Settings ----------: -
Number of Runge-Kutta stages: 3
CFL number: Variable from 20 to 100

MG-Smoothing ----------: -
Residual smoother: Point_explicit
Correction smoother: Point_explicit
Correction smooth epsilon: 0.2
Residual smooth epsilon: 0.2002
Correction smoothing steps: 2
Residual smoothing steps: 2
Smoothing relaxation steps: 2

MG Start up ----------: -
Multigrid start level: 1

References ----------: -
Reference temperature: 273.15
Reference Mach number: 0.730
Reynolds number: 6.50e+06
Reynolds length: 0.61
Prandtl number: 0.72
Gas constant gamma: 1.4

References ----------: -

Reference temperature:	273.15
Reference Mach number:	0.730 (0.67 For NLF case)
Reynolds number:	6.50e+06 (19e+06 For NLF case)
Reynolds length:	0.61 (1 For NLF case)
Prandtl number:	0.72
Gas constant gamma:	1.4
Geometry ----------: -	
Grid scale:	1.0
Reference relation area:	0.0
Reference length (pitching momentum):	1.0
Reference length (rolling/yawing momentum):	1.0
Origin coordinate x:	0.0
Origin coordinate y:	0.0
Origin coordinate z:	0.0
Turbulence ----------: -	
Turbulence model version:	SAO (or Wilcox_k-w in NLF validation case)
Maximum turbulence production/destruction:	1000
Boussinesq modification for k-production (0/1):	0
Kato Launder modification factor:	1
Turbulence equations use multigrid (0/1):	0
Ratio mue-t/mue-l:	0.1
Maximum limit mue-t/mue-l:	20000
Turbulent intensity:	0.001
Reference bl-thickness:	1e+22

4. Investigations and Discussion

4.1 Supercritical Aerofoil (Validation)

The purpose of this investigation is to understand the flow behaviour of the RAE2822 aerofoil during transonic conditions. The data obtained will be used as the base control and then compared with flow characteristics caused by geometric modification. This section provides verification and validation of the mesh and data for the baseline aerofoil.

Problem definition

Reference temperature: 273.15K

Reference Mach number: 0.73

Reynolds number: 6.50×10^6

Reynolds length: 0.61

Angle of attack: 2.79^o (Corrected angle for CFD, 3.19^o used in wind tunnel)

Verification Process

A mesh independent study was constructed to validate the solver's accuracy on partial differentiation. The problem definition is based on AGARD's experimental data [13].

The study analysed the output solution difference in 11 different mesh sizes; ranging from ~20,000 cells to ~4 million cells mesh. The unstructured meshes used are displayed in figure 4.1.1 and 4.1.2. The farfield from the aerofoil is set to 100 chord length. This is an industry standard default provide by the software, to eliminate any possible walls effect. The solver was set to Upwind Backward Euler scheme, and the 1 equation Spalart-Allmaras turbulence model was applied. The first cell height was set at 1.61×10^{-6}, in order

to achieve y+ ≈ 1 as required by the turbulence model. The convergence criteria were set at $1x10^6$ and maximum of 200,000 iterations.

In table 4.1.1, the results indicate that as the mesh size increases, the output solution will tend towards being exact. This is because as the mesh size tends toward infinity, the errors between the partial differentiation with tend toward zero, as the distance between each node is reduced. This implies that with a very fine mesh output, the solution would be very similar to the Navier-Stoke equation. However, using infinite size mesh will reduce the error caused by the governing equations, but result in a time and financial penalty. It is important to remember that the Navier-Stoke equation only provides a very good estimate of flow features. It is not an exact solution of the flow physics. It is interesting to note that the difference in C_L and C_D between ~50,000 cells grid and ~4,000,000 cells grid is only 4.46% and 1.62% respectively. Then, by increasing the mesh size to ~250,000 cells, the difference between ~4,000,000 cells for C_L and C_D is only 1.74% and 1.80% respectively. Figure 4.1.3 and 4.1.4 indicates lift and drag convergence as more cells are inserted into the mesh. Thus, the 'exact solution' for this scenario is ~4,000,000 cells grid, with $C_L = 0.8131$, $C_D = 0.0166$ and shock location x/c = 0.5264.

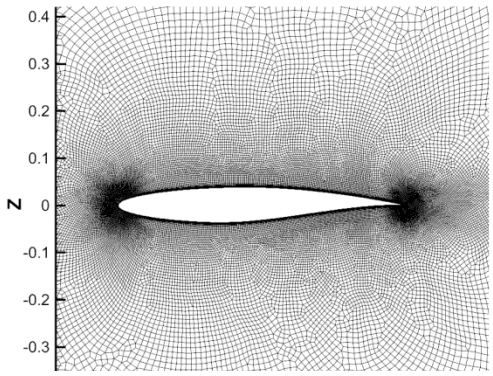

Figure 4.1.1 RAE2822 with 149,986 surface elements grid.

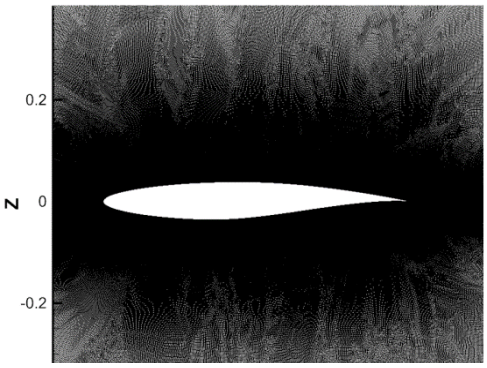

Figure 4.1.2 RAE2822 with 3,873,611 surface elements grid.

Table 4.1.1 – Mesh independent study and comparison with data

				Difference between Biggest and Smallest Mesh		Compared with Data	
Surface Elements	C_L	C_D	Max y+	Delta-C_L	Delta-C_D	W/T C_L	W/T C_D
19,614	0.7226	0.01960	0.9658	11.17%	18.12%	10.01%	16.65%
52,135	0.7772	0.01686	1.0423	4.46%	1.62%	3.22%	0.36%
89,931	0.7894	0.01673	1.0462	2.96%	0.86%	1.70%	0.39%
149,986	0.7959	0.01641	1.0611	2.16%	1.08%	0.89%	2.31%
252,808	0.7993	0.01629	1.0642	1.74%	1.80%	0.46%	3.02%
534,035	0.8043	0.01634	1.0723	1.13%	1.51%	0.16%	2.73%
820,390	0.8075	0.01643	1.0759	0.74%	0.98%	0.55%	2.22%
1,424,841	0.8099	0.01649	1.0793	0.44%	0.62%	0.86%	1.86%
1,808,283	0.8109	0.01652	1.0794	0.32%	0.42%	0.98%	1.66%
2,038,897	0.8113	0.01652	1.0790	0.26%	0.43%	1.03%	1.68%
3,148,634	0.8128	0.01656	1.0805	0.09%	0.18%	1.21%	1.42%
3,873,611	0.8134	0.01659	1.0803	0.00%	0.00%	1.30%	1.25%

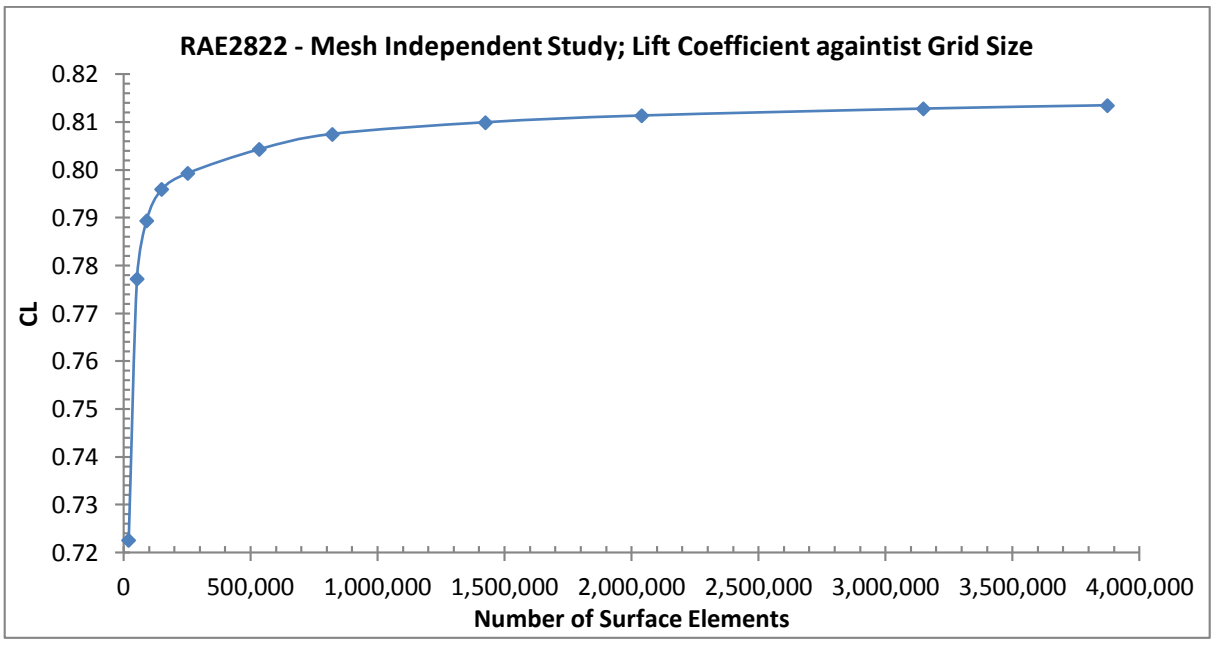

Figure 4.1.3 Graph showing the change in lift coefficient with the increase of surface elements.

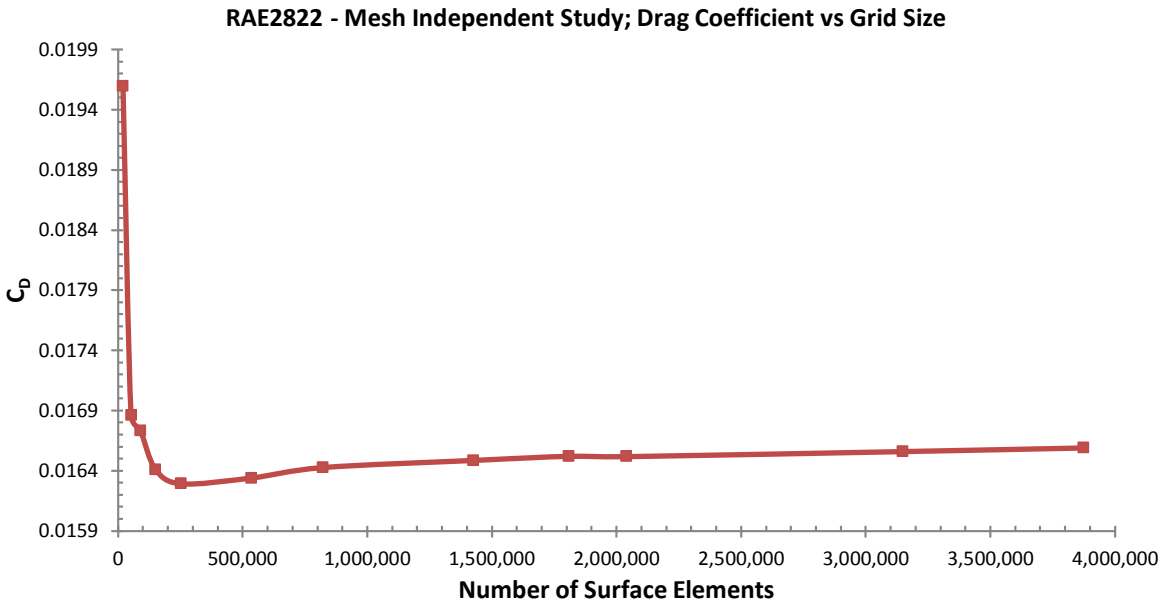

Figure 4.1.4 Graph showing the change in drag coefficient with the increase of surface elements.

Based on final lift and drag coefficients, several manual local refinements were attempted at the shock and wake region to reduce computational time with less elements mesh. The shock location was determined by a filtering algorithm process proposed by Lovely and Haimes (1999)[29]. A 'wake line' was also added to the geometry to provide further accuracy in a coarse mesh. In the refinement study, 5 different meshes were generated: "100%" spacing with Wakeline and Shockline (figure 4.1.5); "100%" spacing with Wakeline and Shockline refinement; "100%" spacing with Wakeline, Shockline refinement spacing and leading edge and trailing edge refinement; "50%" spacing with Wakeline and Shockline (figure 4.1.6) and "25%" spacing with Wakeline. From the simulation produced, in a highly refined mesh it is clear that there is no need for shock location refinement as the existing grid is already fine enough.

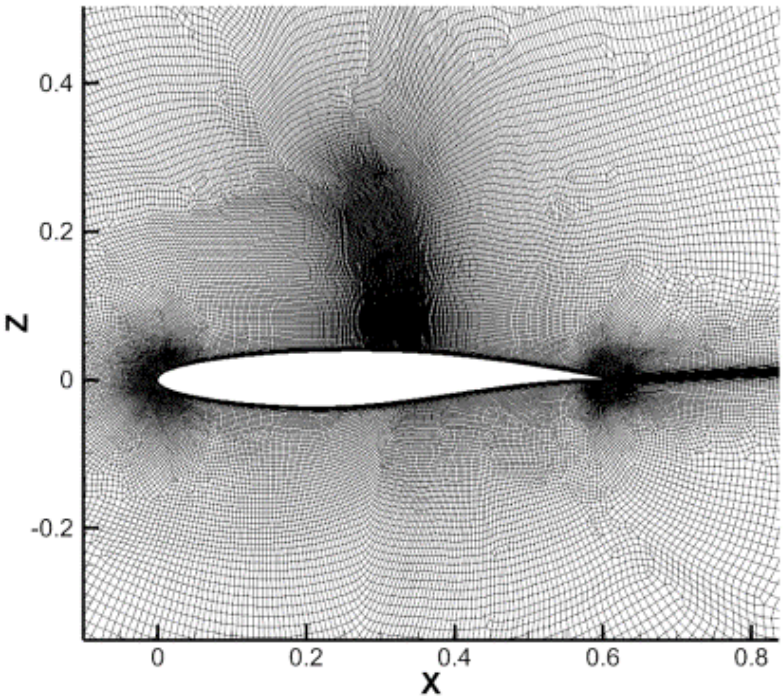

Figure 4.1.5 RAE2822 aerofoil with manual refinement at shock and wake region, “100%” spacing with Wakeline and Shockline.

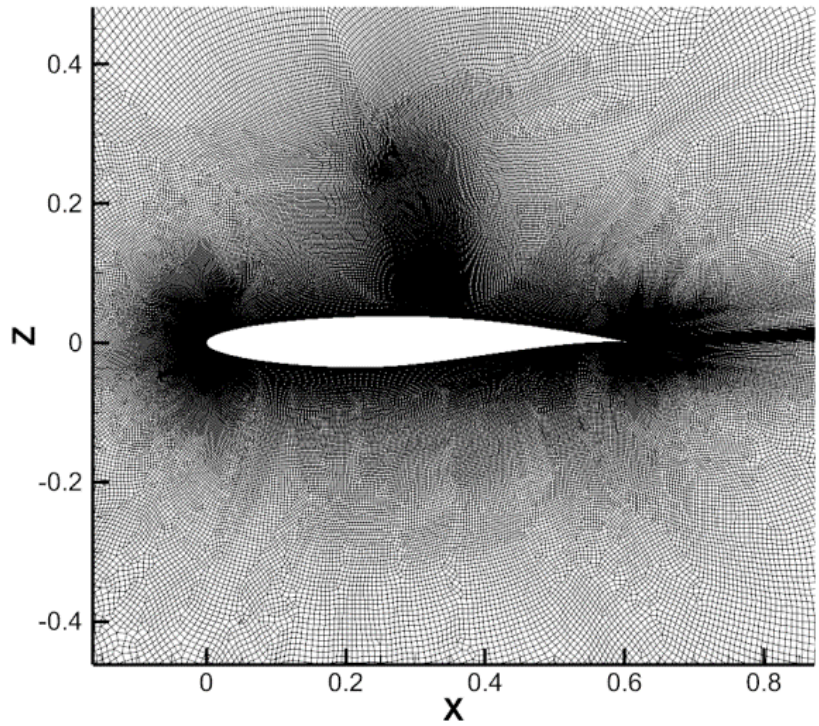

Figure 4.1.6 RAE2822 aerofoil with manual refinement at shock and wake region, “50%” spacing with Wakeline and Shockline.

Validation

The C_L and C_D values obtained from wind tunnel experiments are 0.803 and 0.0168, respectively [13]. The simulation results are compared with wind tunnel data, along with surface pressure distribution. The simulation and wind tunnel data pressure plot displays a positive correlation, however, in figure 4.1.7, the shock location is slightly under predicted from CFD simulation.

The coarse grid predicted the shock location at x/c = 0.50274, slightly earlier than the finer grid. This is because as grid size increases the shock position begins to shift. With the cells spacing getting very close (~800,000 cells and above) the shock position shifting is also negligible. The shock location difference between 4,000,000 cells and 800,000 cells is only $x/c = 3x10^{-3}$.

Taking the finest mesh solution and comparing with experimental data, the results are represented in Table 4.1.2. The CFD solution displayed is a very good match with wind tunnel data, with only 1.30% difference in C_L and C_D. It is interesting to note that at ~500,000 cells mesh, the C_L is the closest match to experimental values. It is only 0.16% different, but C_D show a difference of 2.73%. This is because both CFD and wind tunnel data will only provide a rough estimate of the flow features; both contain errors. Wind tunnel testing contains several induced errors, such as wall effects, turbulence intensity, and temperature fluctuation. The choice of mesh size is critical. Dense mesh can lead to a more reliable result, however due to the extra cost it is essential to balance the expense against the potential for errors.

From all the results shown, the discrepancy between computed and experimental results are very small. We can therefore conclude that the results obtained from the baseline clean aerofoil configuration are valid and accurate. However, the pressure distribution on the suction surface is slightly different than the wind tunnel data. The CFD result displayed a stronger suction at the leading edge, and a more rapid change in pressure during the shock region than the wind tunnel data.

Table 4.1.2 Data Comparison

Method	Alpha	CL	Δ CL (%)	CD	Δ CD (%)	Shock location
AGARD data[14]	3.19°	0.8030		0.0168		0.5200
S-A model, Tau solver	2.79°	0.8134	1.30	0.0166	1.25	0.5264

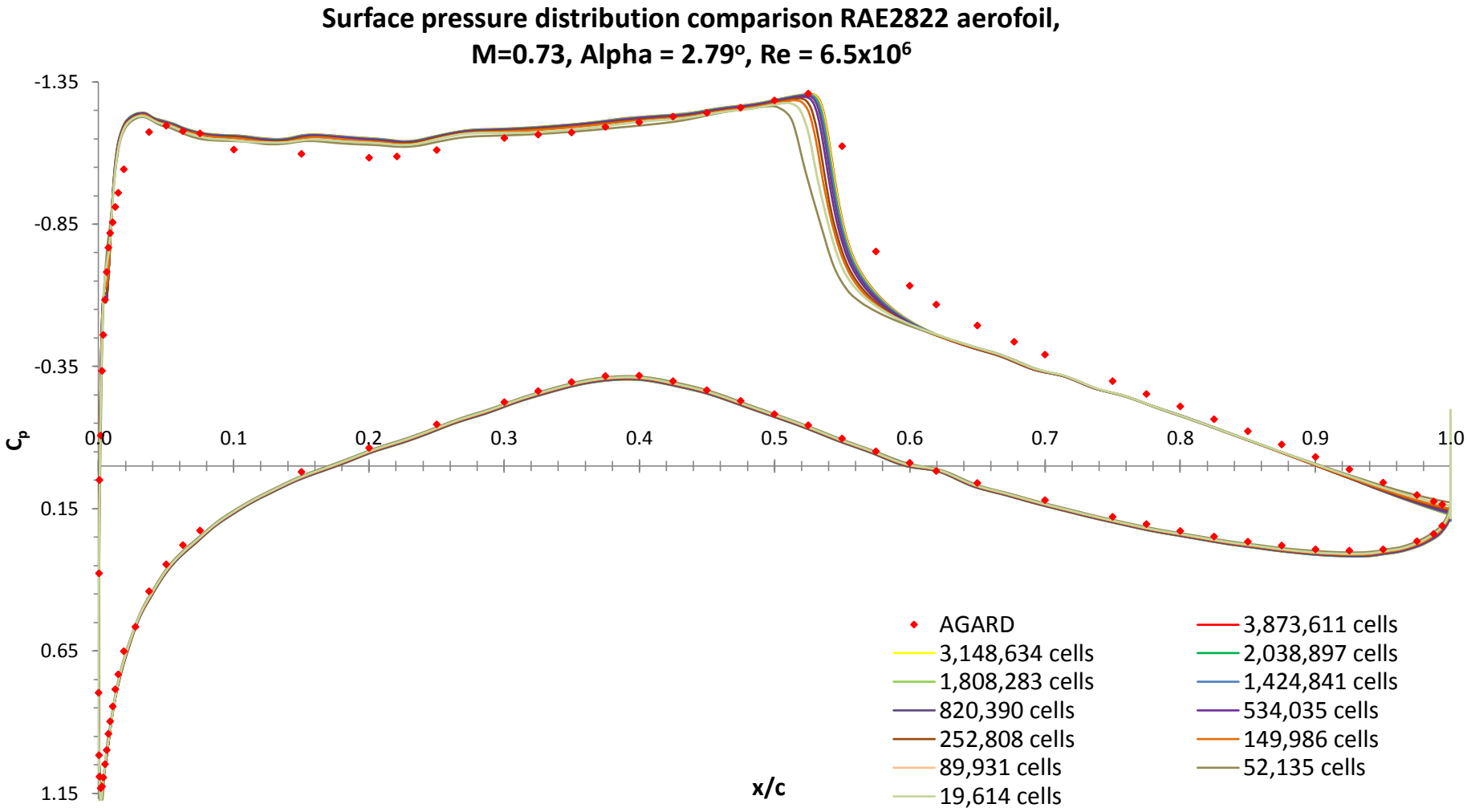

Figure 4.1.7 Pressure distribution plot: Mesh independent study

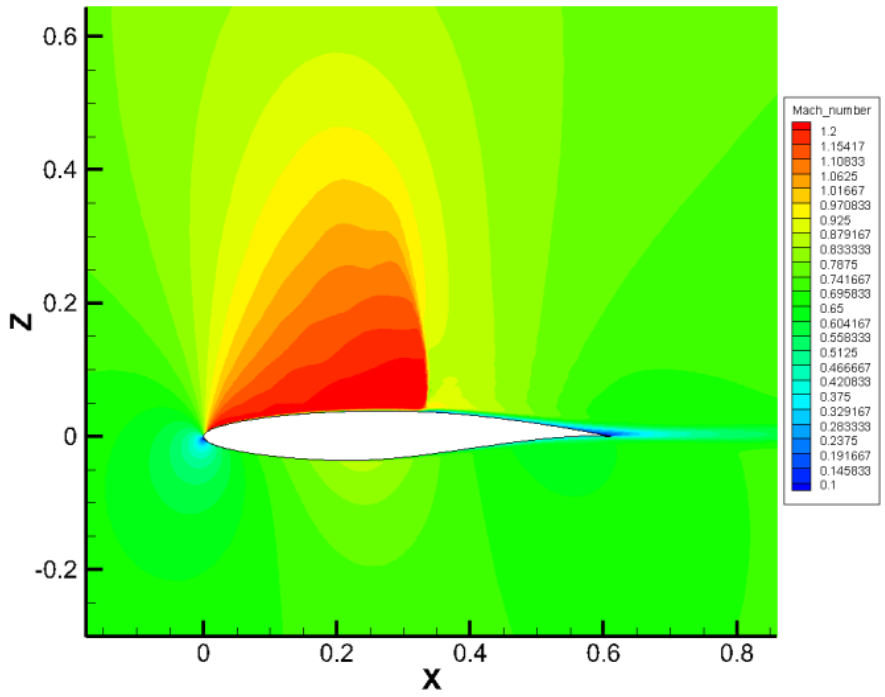

Figure 4.1.8 Mach number contour

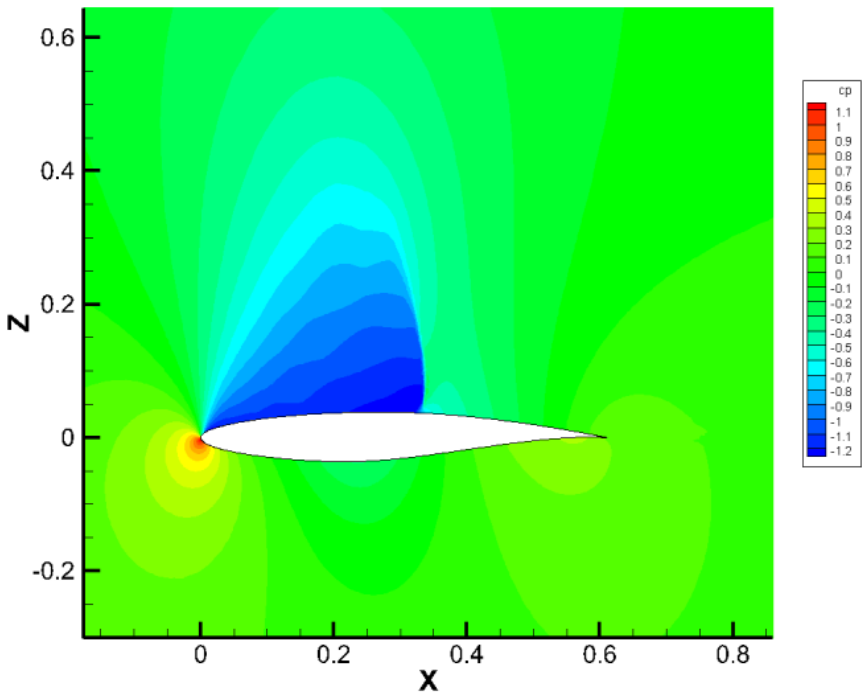

Figure 4.1.9 Pressure Coefficient

Comparison with AGARD's wind tunnel (C_L = 0.803, C_D = 0.0168) indicates a close relationship with the results of highly refined mesh of C_L = 0.813 and C_D = 0.0166. The ΔC_L = 1.23%, ΔC_D = 1.20%. The shock location from the wind tunnel test is also given as 0.52 x/c. Therefore, it can be concluded that the results obtained from the baseline clean aerofoil configuration are valid and accurate. However, the pressure distribution on the suction surface is slightly different than the wind tunnel data. The CFD result displayed a stronger suction at the leading edge, and a more rapid change in pressure during the shock region than the wind tunnel data.

Turbulence Model Selection

There are 5 turbulence models available within the TAU solver: Spalart-Allmaras (SA); Sparalart-Allmaras modified (SAM); Wilcox kω; Menter Baseline model and the Menter SST model. The selection process uses a 220,000 cell mesh with a farfield of 25 chord length. This is because of the high computational cost when using high density mesh. The simulations are tested with the same conditions described previously, against a different turbulence model. The residual convergence criteria are set to $1x10^{-6}$ maximum iteration 100,000. The simulation will terminate when any of the criteria reach maximum iteration.

Table 4.1.3 Turbulence Model Comparison
(i)

	Iterations	C_L	C_{Lp}	C_{Lv}	C_D	C_{Dp}	C_{Dv}	C_M	Max Y+
Spalart-Allmaras (SA)	14192	0.792	0.792	1.048E-05	0.0167	1.108E-02	5.651E-03	-0.175	1.0573
Spalart-Allmaras modified (SAM)	100000	0.795	0.795	-6.235E-06	0.0166	1.108E-02	5.562E-03	-0.176	1.0431
Wilcox kω (2equation)	100000	0.843	0.843	-3.831E-05	0.0193	1.288E-02	6.459E-03	-0.189	1.0584
Menter Baseline model (2equarion)	18866	0.813	0.813	-1.994E-05	0.0178	1.180E-02	5.971E-03	-0.181	1.0631
Menter SST model (2equation)	100000	0.778	0.778	-1.059E-05	0.0163	1.070E-02	5.625E-03	-0.171	1.0413

(ii) – Comparison with experimental data

	Delta C_L	Delta C_D	Total Run Time (s)	Time per Iteration (s)
Spalart-Allmaras (SA)	1.32%	0.39%	970	0.0683
Spalart-Allmaras modified (SAM)	0.94%	0.95%	6930	0.0693
Wilcox kω (2equation)	4.99%	15.09%	7526	0.0753
Menter Baseline model (2equarion)	1.24%	5.77%	1441	0.0764
Menter SST model (2equation)	3.17%	2.83%	7907	0.0791

The wind tunnel data for this specific condition is $C_L = 0.803$ and $C_D = 0.0168$.

Table 4.1.3, with the Spalart-Allmaras modified, Wilcox kω and Menter SST turbulence model displays difficulties in reaching to the set convergence criteria for this specific mesh. The maximum y+ in all simulation is very close to 1. With a slight alteration to the mesh, it is possible that future simulations with the previous named turbulence model might converge within 100,000 iterations. It is also possible that the simulations have not being running long enough to achieve the convergence criteria. Therefore, the comparison of 'Total Run Time' is rejected. The Spalart-Allmaras model performed fastest, with only 0.0683s per iteration. The slowest model was Menter SST 2 equation turbulence model, with 0.0791s. Both the SA and the SAM turbulence models provide very similar results to the experimental data. The SA model showed the best correlation in C_D, with just 0.39% difference, but a 1.32% difference in C_L. On the other hand, the SAM model showed an approximately 1% discrepancy for both lift and drag. However, the Wilcox kω and Menter SST models display a larger difference as well as an increased time penalty. The SA model is widely used and optimised for the aerospace application [19]. With computation time cost and accuracy taken into account, the SA model was selected. This model and aerofoil was also selected in Yu et al's (2011) [14] transonic investigation.

4.2 Supercritical Aerofoil Gurney Flap study

The main function of the Gurney flap is lift enhancement. By the use of the Gurney flap, the same lift can be produced while a reducing of alpha. It was shown by Yu et al (2011) [14] that in addition, a Gurney flap may increase surface suction and delay shock. This is an important feature in shock control. The author believes this is an area that can be further developed and possibly integrated with other shock control devices to enhance the benefits of drag reduction.

4.2.1 Lift constrained investigation

RAE2822 supercritical aerofoil is used as the baseline, comparing its flow features with the additional of GF. The height of GF is typically measure in respect to chord length. In the investigation, 11 different flap heights were used; two upward GFs (0.1%c, 0.25%c) and seven downward (01%c, 0.2%c, 0.3%c, 0.4%c, 0.5%c, 0.6%c, 0.7%c) GFs. The thickness of the GFs remained constant. The meshes are generated through SOLAR and TAU is used to solve RANS equations with one-equation S-A turbulence model for this problem.

Mesh independent analysis was conducted on Gurney flap cases and clean aerofoil cases (see previous section), it is clearly shown that beyond 1.8million cells, the solution has very small alterations and tends toward exact. Then by considering time and computation cost, the ~1.8million cells grid size was selected for this single point optimisation study. The simulation parameter is set to cruise condition for the RAE2822, which is M = 0.73, Re = 6.50 x 10^6 (based on a chord length of 0.61m) and C_L = 0.81. This is because the C_L

obtained at alpha 2.79^{o} is approx. = 0.81. The simulation for clean aerofoil was also re-run with lift constrained.

Results

Under the lift constrained condition, the 1.8million mesh baseline aerofoil shows a characteristic of C_D = 0.01644, L/D = 49.24, max Mach = 1.297, shock location x/c = 0.524 and alpha = 2.783^{o}.

From the results obtained, in figure 4.2.1.1, it is interesting to note that there is very little effect on C_p distribution with upward GFs. Slight decrease in lift-to-drag ratio was observed along with a slight increase in maximum Mach number on the suction surface. The pressure drag component was shown to have increased as shock strength increased. An increase of pressure (reduction of suction) was expected on the upper trailing edge of the upwards GFs, but the graphical results did not represent that hypothesis. However, in the figure 4.2.1.5 a vortex is clearly seen on the upper surface of the aerofoil. This means C_p must not be the same as the baseline. The problem may be caused by the trailing edge stagnation point. Currently, these problems have not been further investigated. It is clearly seen in Figure 4.2.1.4 for the downward GFs that shock is delayed downstream. In this particular case, the 0.6%c GF resulted in a maximum drag reduction of 21 counts (C_d = 0.002169). The drag reduction occurred because the shock was weaker and moved further downstream, which resulted in a large decrease in the pressure drag component.

Figure 4.2.1.3 shows a drag component break down of various GF heights. Vortices were introduced from the flap, which resulted an increase in C_{Dv}. The increase in C_{Dv} was relatively small in comparison to the pressure drag. Therefore, the total drag was reduced. In this investigation, it indicates that even a 0.1%C height GF, shock is still delayed and

results in a large reduction in pressure drag. Nevertheless, drag will not infinitely decrease along with growing flap height. There is an optimum position: when using the flap beyond optimum height drag penalty will increase. It is believed that this phenomenon may be caused by the unsteady vortex shedding aft of the flap. In the current investigation of small GF >1%C, they are set performed using a steady solver and the calculations are fully converged. This implies the flow is steady.

The surface skin friction plot in figure 4.2.1.2 suggests that shock induced separations are reduced with downward GF. The immediate after shock, the C_f curve, displays a rapid decrease in skin friction then increases slowly again. Unlike the baseline case, however it did not reach zero (when flow separation occurred). Instead it retained a very small amount of skin friction, and with an increase of flap height, the flow attachment became firmer. This is seen in figure 4.2.1.2 where the bottom peak travel further upward in relation to flap height increment. This indicates the flows remain attached when a downward GF are installed.

For all the GF cases, there are two main vortices shown: clockwise vortex shed immediately in front of the flap and a large clockwise vortex at the top trailing edge off the suction surface. In some scenarios, in particular when the flap height is very short, there is a third vortex, situated under the large vortex aft of the GF, and it is not fully developed (figure 4.2.1.6). Its development can be seen in the streamline plot. It is believed that a further increase in flap height will result in the third vortex being fully developed and combined with the two main vortices. This triggers Karman Vortex Street and the flow conditions will become unsteady. The addition of downward GF can lead to the effective angle of attack being reduced. The range of maximum Mach decrease as the downward GF height increases. The reduction of shock strength and shock delay is

believed to be caused by the 'putting force' coming from the large vortex immediate aft the flap. The vortex pushes the flow rearward, which enhances attachment flow after the shock. The vortices created from the flap can be seen as increased camber and effective chord length.

For the conditions M = 0.73, Re = 6.50 x 10^6 and C_L = 0.81, the optimum flap height is 0.6%c. The 0.6%c suggest a 15.21% increase in L/D, max Mach reduced to 1.249 and shock was delayed to x/c = 0.588.

From the findings of this study, the small upward GF produced very little effect on pressure distribution but the overall drag is increased. All downward GF test show weakening and delay of shockwaves, leading to drag reduction. The angle of attack is also reduced for any given lift.

The GF is in fact an alteration of the chord: increased camber. In effect, it alters the Kutta condition of an aerofoil. It is a lift enhancement device and it was expected to have an increase in L/D. The shock delay caused by the downward GF can be explained as an effect of the increased camber and accompanied with the rotating vortex at the trailing edge. It is believed that the rotating vortex provides a "pulling" force to the suction / upper surface, forcing the flow to attach along the surface. At the same time the flow velocity is also increased by this force. This explanation requires further evidence and analysis to support.

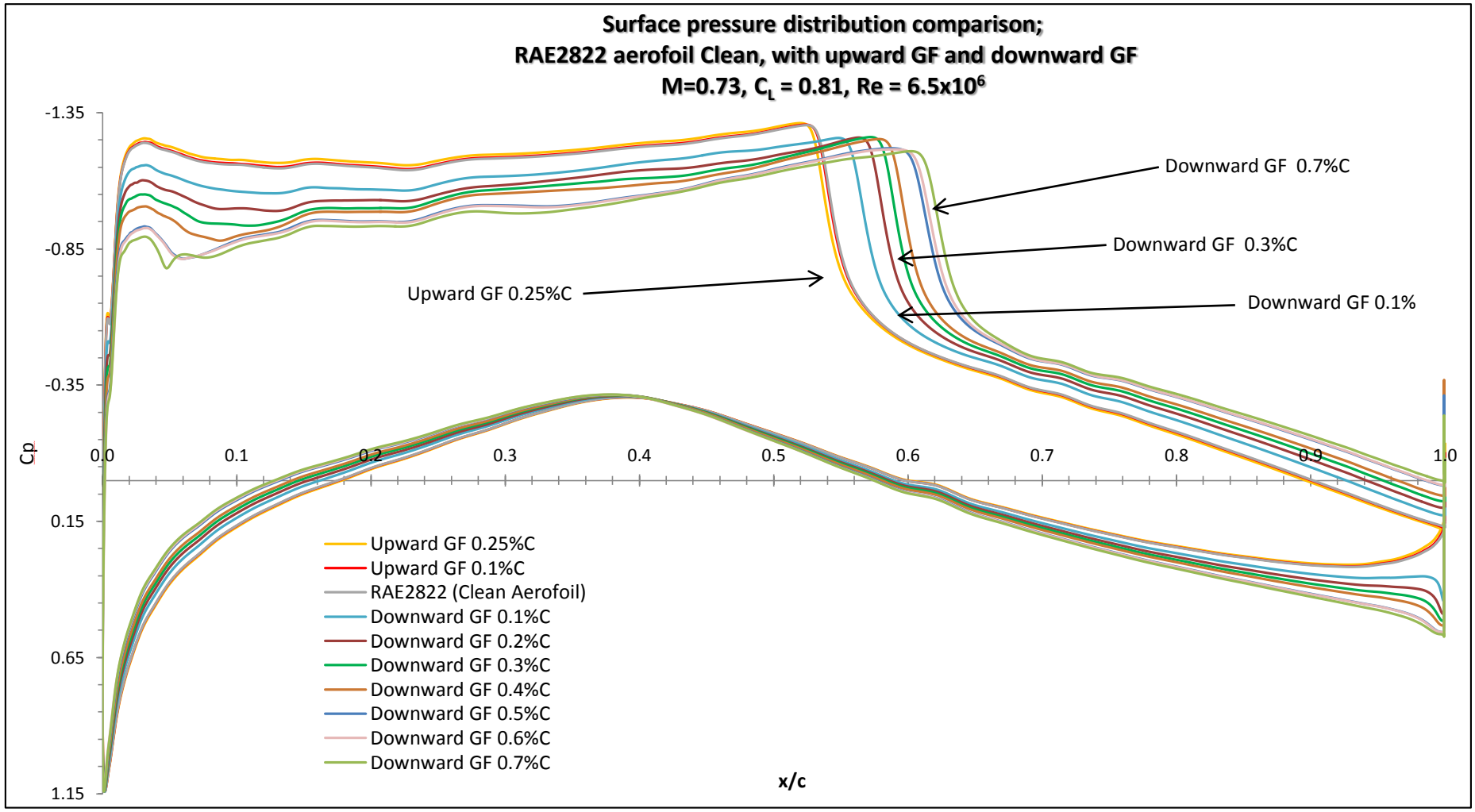

Figure 4.2.1.1 Surface pressure distribution comparison for RAE2822 + Gurney Flaps

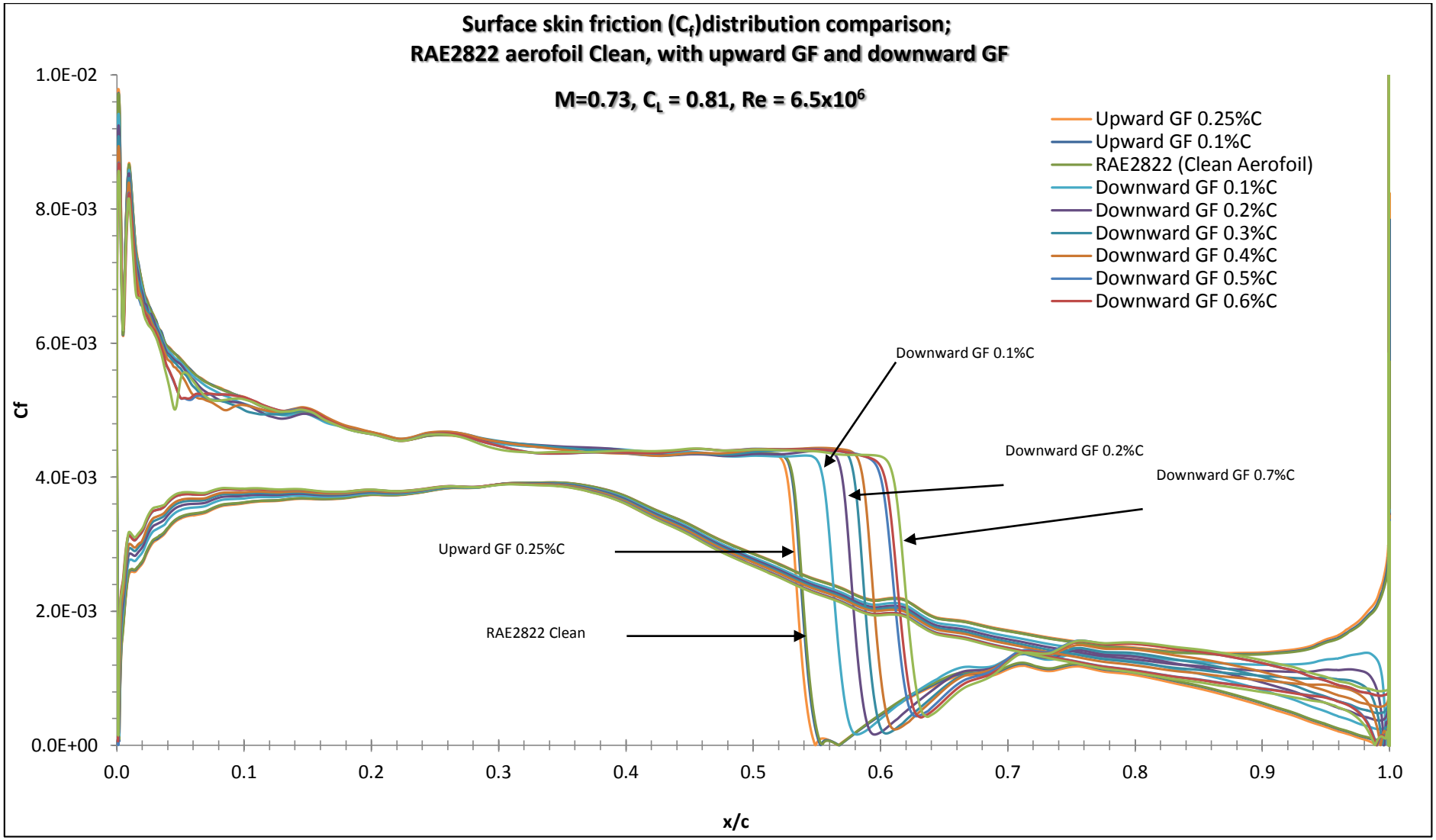

Figure 4.2.1.2 Surface skin friction distribution comparison for RAE2822 + Gurney Fla

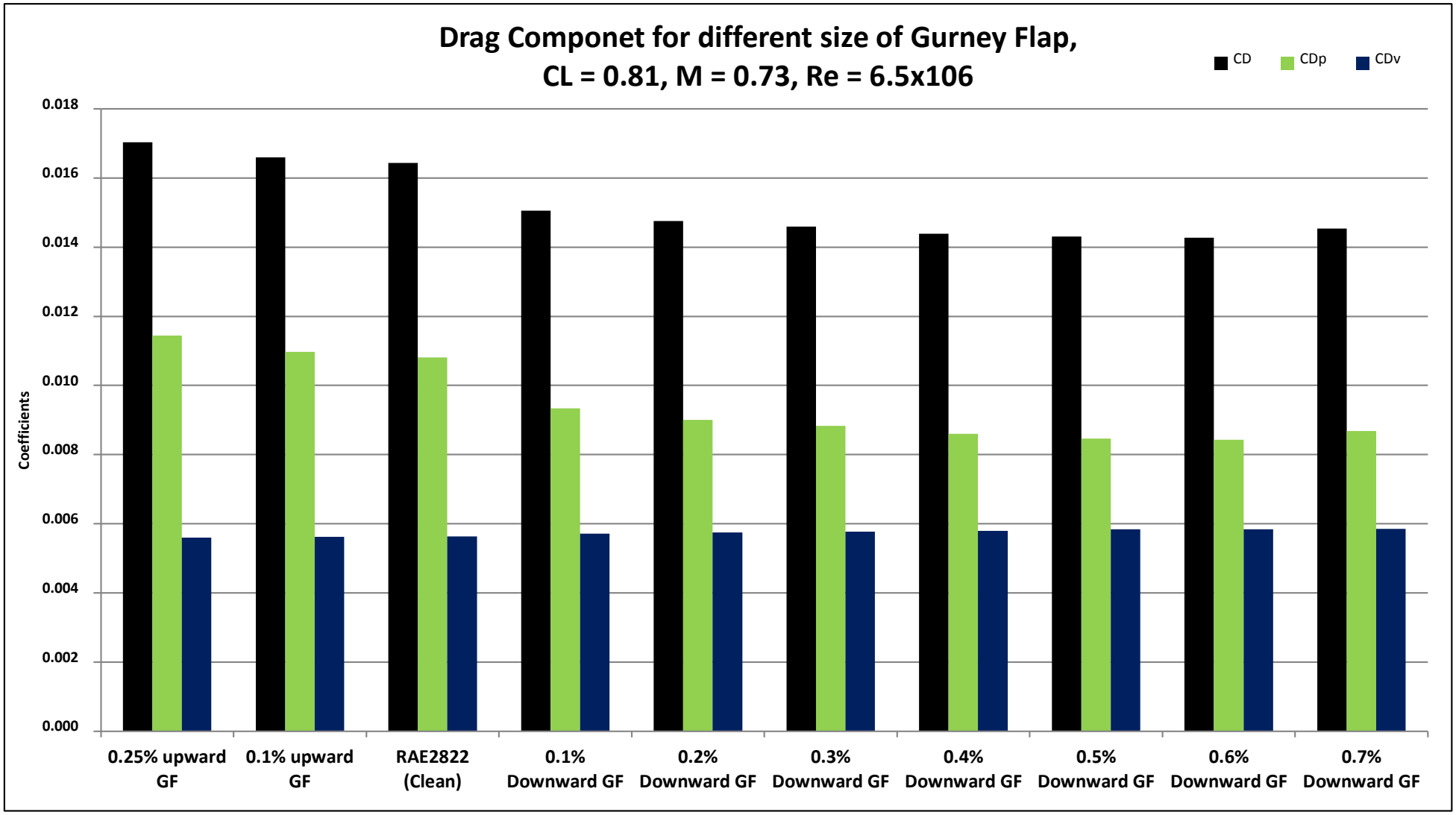

Figure 4.2.1.3 Drag Component comparison for RAE2822 + Gurney Flaps

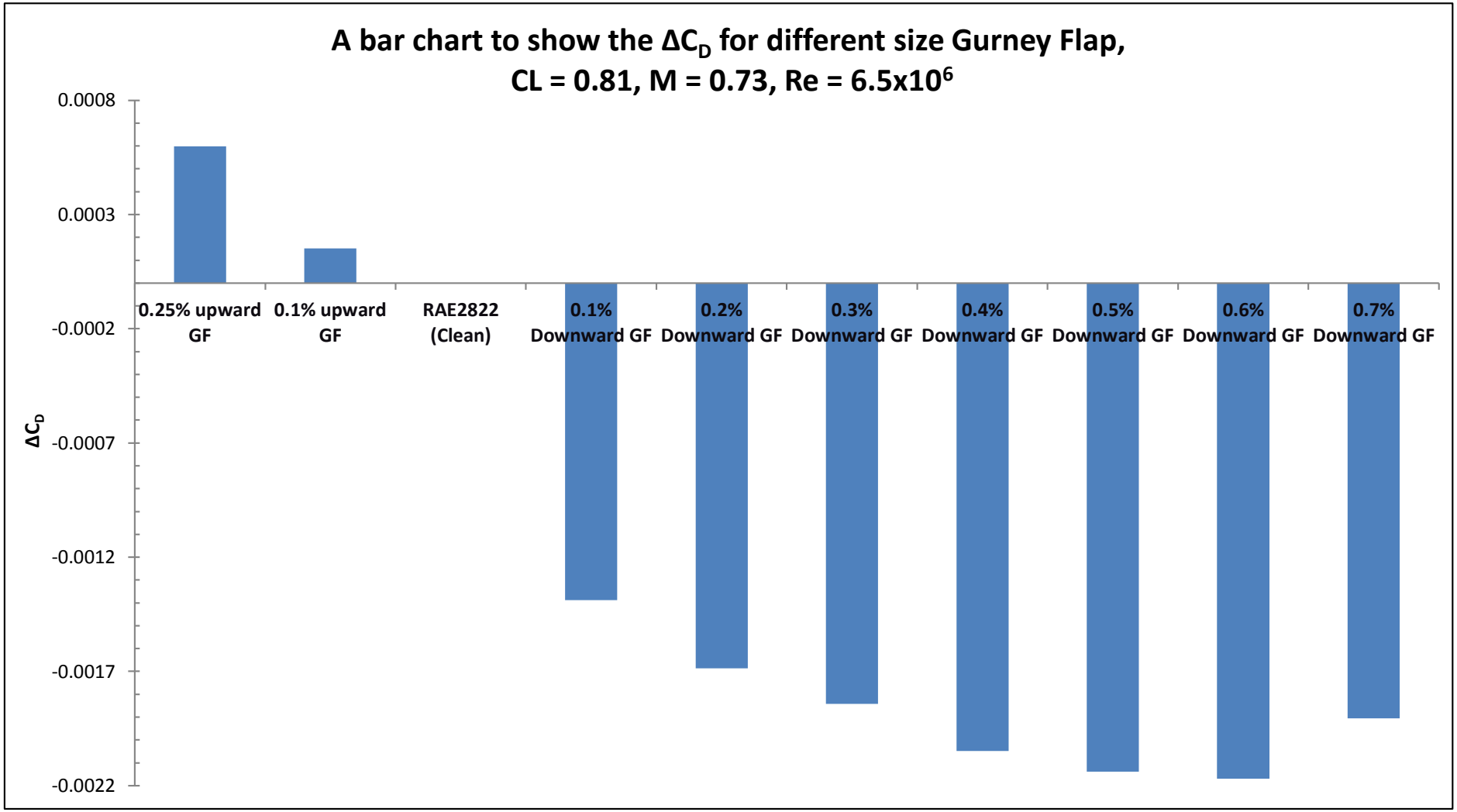

Figure 4.2.1.4 Bar chart to show the changes in drag for different size Gurney flap

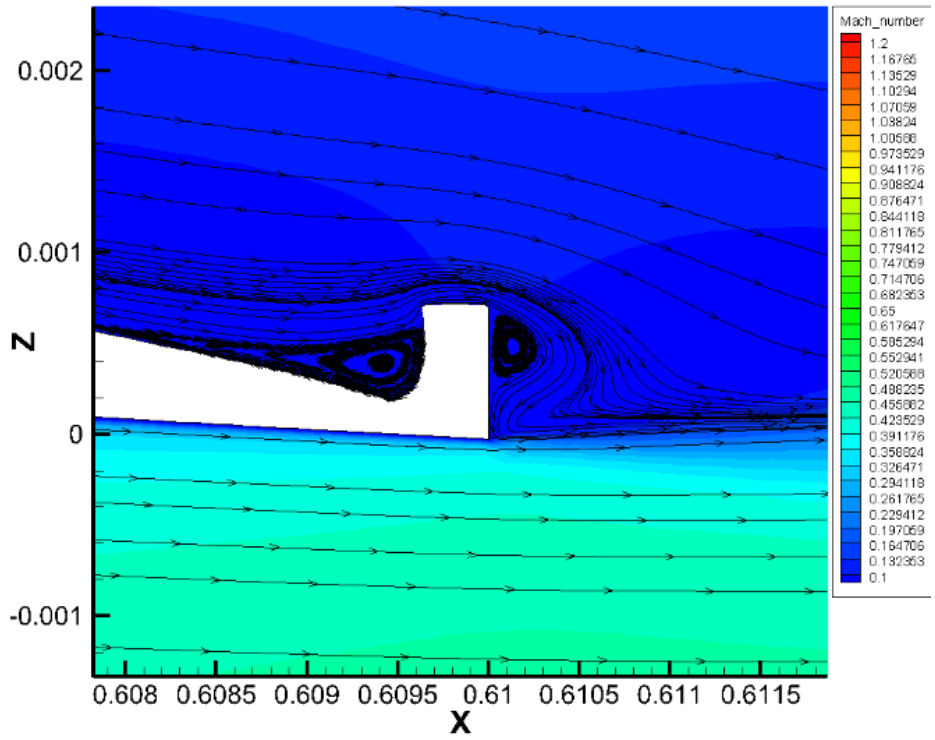

Figure 4.2.1.5 Mach Contour plot and stream plot for RAE2822 with 0.25%c upward Gurney flap

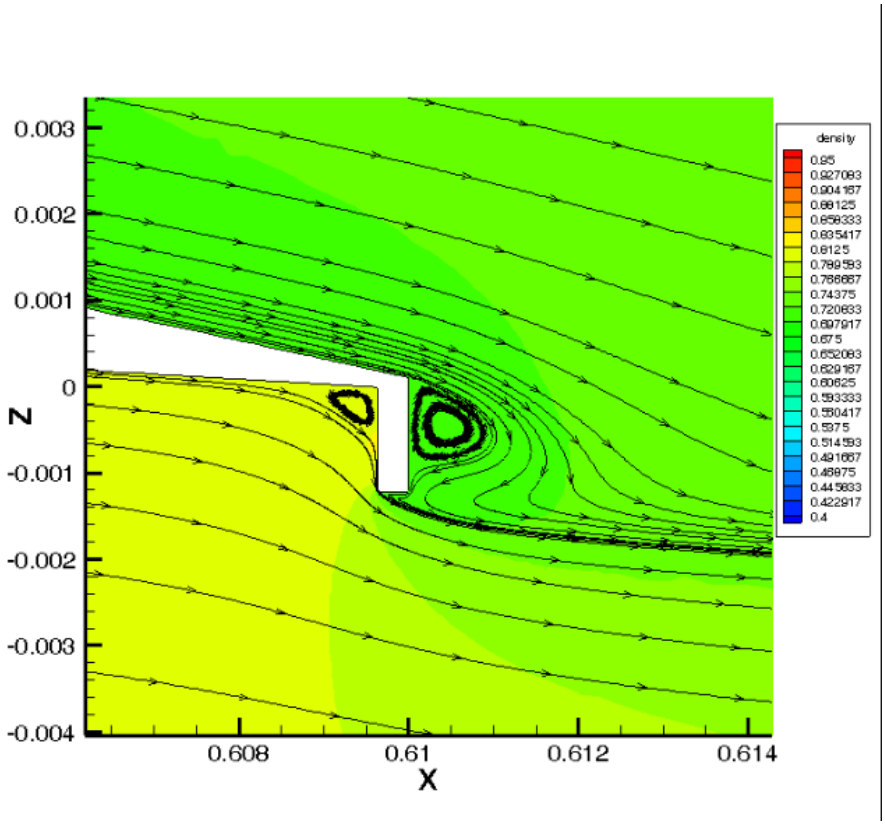

Figure 4.2.1.6 Mach Contour plot and stream plot for RAE2822 with 0.20%c Gurney flap

4.2.2 Camber-line Modification and Gurney Flap investigation

In the previous section, it showed positive drag reduction with the addition of a Gurney flap. It is very interesting that a small plate attached to the trailing edge of a wing can increase a vast amount of performance. The addition of Gurney flap can be seen as a camber alteration. From results in previous section, for a given lift condition, the Gurney flap alters the Kutta condition, it increases rear loading and reduces top surface suction in comparison with the clean aerofoil. The lift enhancement behaviour also suggests the addition of Gurney flap affects the aerofoil's effective camber line. This is a form of trailing edge modification, which alters the effective camber. Therefore, by looking at the drag produced by the Gurney flap addition and camber-line alteration with the same lift performance can suggest validation Gurney flap over aerofoil redesign.

The camber-line calculation is obtained from the vortex situated in front of the flap. The curvature flow travelled outside the vortex was considered as elliptical, this curvature flow is assumed to be the 'pressured surface' as if the Gurney flap not installed. By approximation, the centre point of the ellipse was obtained, the original camber line are then modified using the elliptical equation. The distance between upper curve and lower curve to the camber line retained as the same as the baseline aerofoil. The upper and lower curve co-ordinates are obtained through the derivative of the camber line, then generate an equation normal to the camber line, and by inserting the 'thickness' (distance). The surface co-ordinates are then calculated.

The selected Gurney flap geometries are 0.3% and 0.4% chord. Then the two camber-line modified aerofoils were generated; in respect to 0.3%c and 0.4%c Gurney flap. The

geometries were simulated at M = 0.73, Re = 6.5 x 10^6, Chord length = 0.61m (based on AGARD RAE2822 case 9) through TAU, using SA turbulence modelling.

As predicted, the camber modified aerofoil showed approximately the same lift enhanced behaviour as the Gurney flap. This is shown in figure 4.2.2.1, C_L-alpha plot, the cambered aerofoil and Gurney flap aerofoil laid exactly on top of each. And more interestingly, figure 4.2.2.3, the C_m behaviour is almost identical for both cambered and flap added aerofoil. This suggests the Gurney flap and cambered alteration contains similarly aerodynamic behaviour, this mean C_L and C_m can act as a constraint. In terms of drag coefficient in respect to angle of attack, it is clearly show that the standard clean aerofoil produces the less drag, the camber modified version is always less drag then retrofit Gurney flap. This is only valid in reference to angle of attack. The aerodynamics performance can be seen in figure 4.2.2.4, the addition of Gurney flap or camber modification clearly shown an increase in L/D ratio. Again, the simulation results it indicates the camber modified aerofoil contains less drag than the addition of GF.

In Table 4.2.2.1, this is the simulation results of lift constrained scenario, it indicate that both cambered and Gurney addition generates a positive benefit to the L/D ratio. The cambered aerofoil (replica of Gurney flap addition) performed very similar in term of pitching. However, in terms of drag, figure 4.2.2.1a the cambered version conquers over the standard Gurney flap. In the drag breakdown, the C_{dv} remains very similar for all 5 cases, but the C_{dp} is shows where the difference occurs. And in both figure 4.2.2.7 and 4.2.2.8 indicates camber modified aerofoil delays shock downstream to the very similar position as Gurney flap can achieve. The main reason for cambered aerofoil in performing less drag than Gurney flap addition, it is because the reduction or elimination of the two rotational vortex caused by the Gurney flap. The cambered trailing edge reduces the rapid

dive sharp corner on the upper surface trailing and the removed of the vertical plate. As the sharp trailing edge abolished, the flow follows the geometry more easily without causing such high distribution and resulting in a large rotational vortex. Although, in figure 4.2.2.10a a vortex exist on the upper surface near the trailing but in comparison to figure 4.2.2.10d the effective are by far much lessen. The vortex immediate in front of the flap is caused by the flap as a blockage of flow causing it to redirect and resulting a vortex. The vortex itself is trapped once it is generated and reached stability, the steam wise flow will then follow around the vortex, treating it as a wedged trailing edge. The cambered version already provided the "wedged" curvature for the lower surface, which implies the rotation vortex is neglected, therefore less energy are wasted.

In this study, the obtained result suggests the modification of camber is more effective than addition of GF. However, GF can be retro fit to service aircraft, and camber alteration can be very difficult achieve to an existing wing.

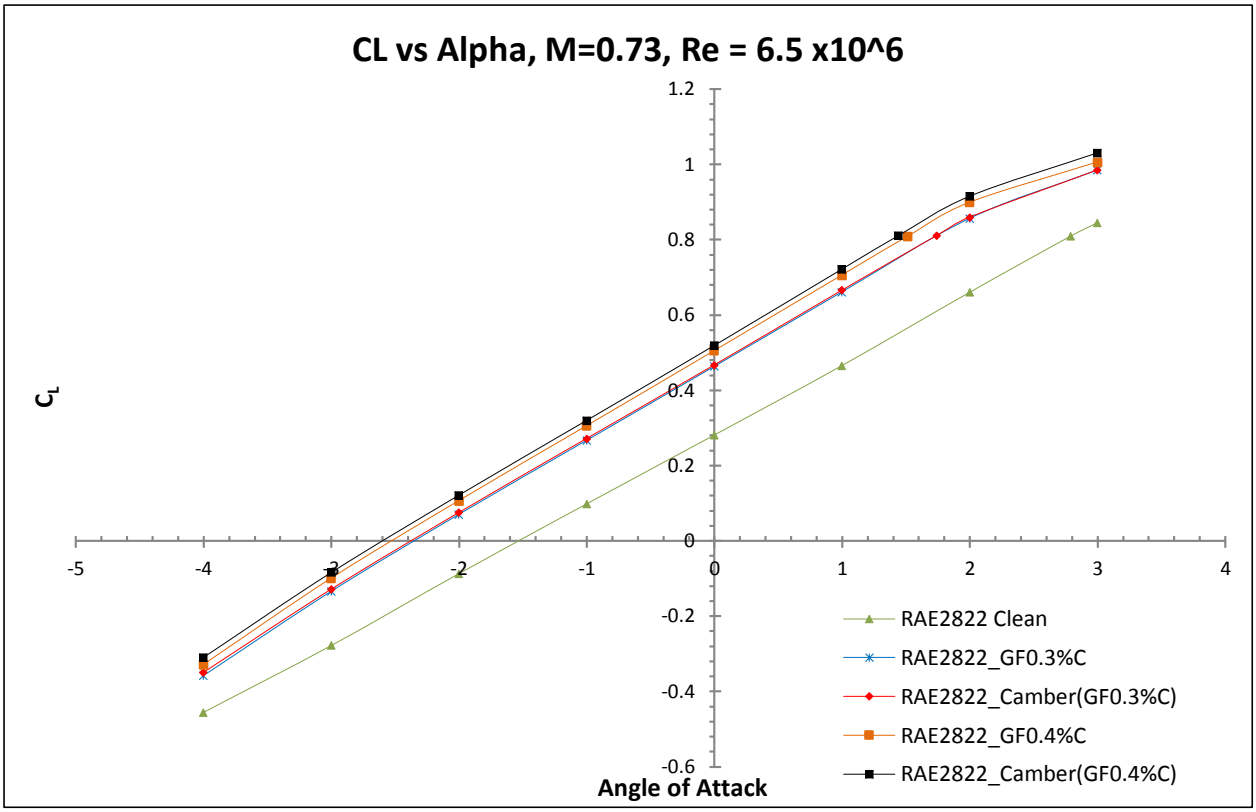

Figure 4.2.2.1, C_L vs Alpha

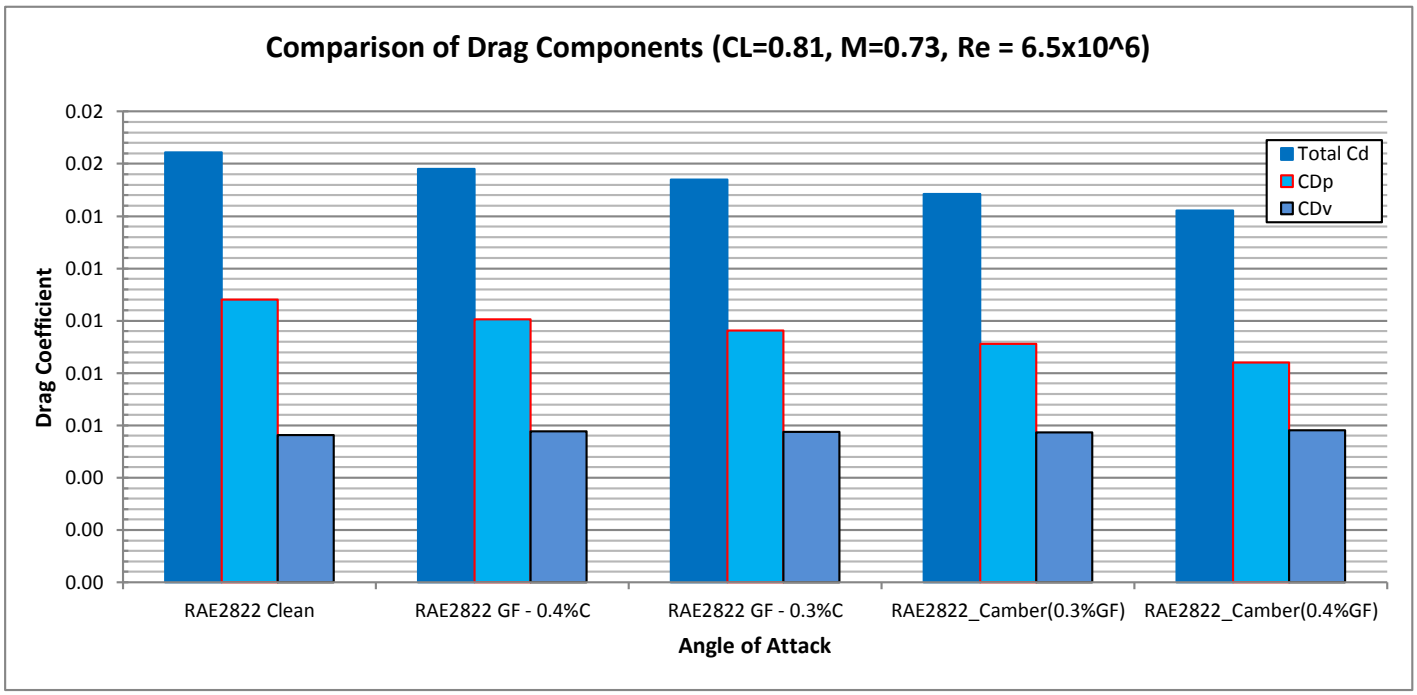

Figure 4.2.2.1a, Comparison of Drag Components (CL=0.81, M=0.73, Re = 6.5x10^6

Table 4.2.2.1

Lift Constrained; $C_L = 0.81$

Aerofoil	Alpha	C_{Ltotal}	C_{Lp}	C_{Lv}	C_{Dtotal}	C_{Dp}	C_{Dv}	C_M	L/D
RAE2822 Clean	2.79	0.809670	0.809647	0.000023	0.016442	0.010815	0.005627	-0.178260	49.243920
RAE2822 GF - 0.3%C	1.727749	0.807683	0.807625	0.000058	0.015393	0.009632	0.005761	-0.206275	52.470714
RAE2822 GF - 0.4%C	1.514209	0.809183	0.809118	0.000065	0.015815	0.010047	0.005768	-0.212099	51.164867
RAE2822_Camber(0.3%GF)	1.740485	0.810958	0.810895	0.000064	0.014853	0.009116	0.005737	-0.205284	54.600084
RAE2822_Camber(0.4%GF)	1.441573	0.810910	0.810836	0.000074	0.014210	0.008403	0.005807	-0.212420	57.065072

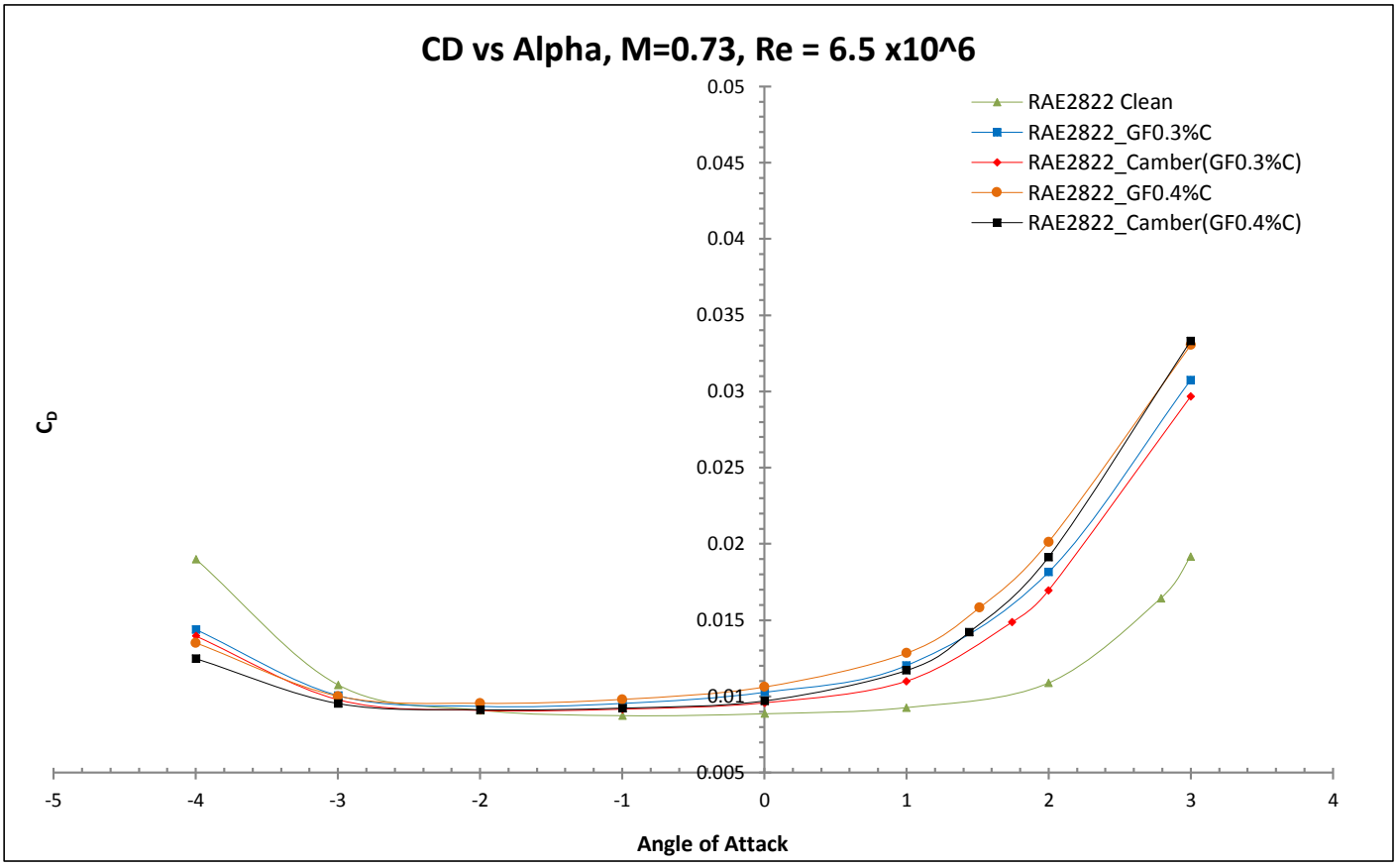

Figure 4.2.2.2, C_D vs Alpha

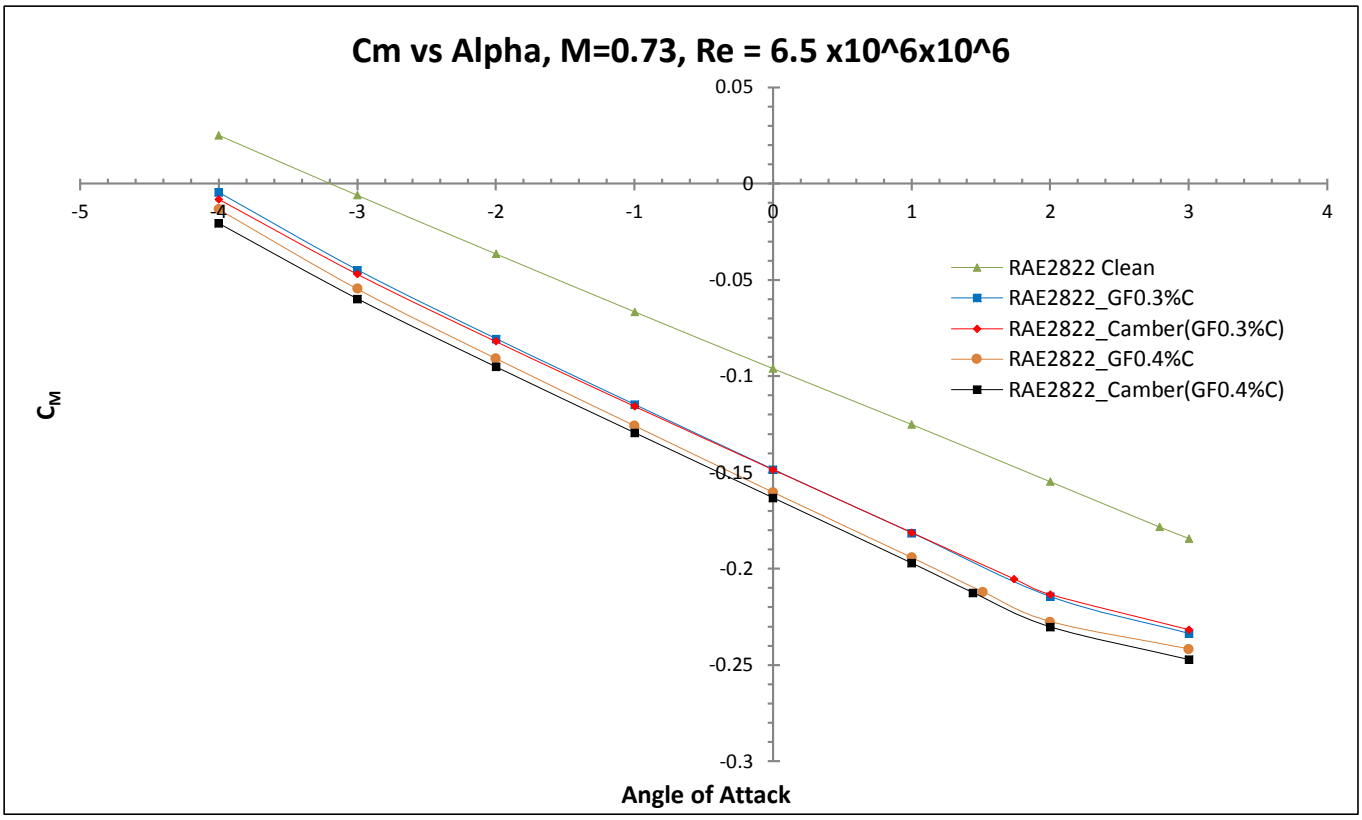

Figure 4.2.2.3, C_m vs Alpha

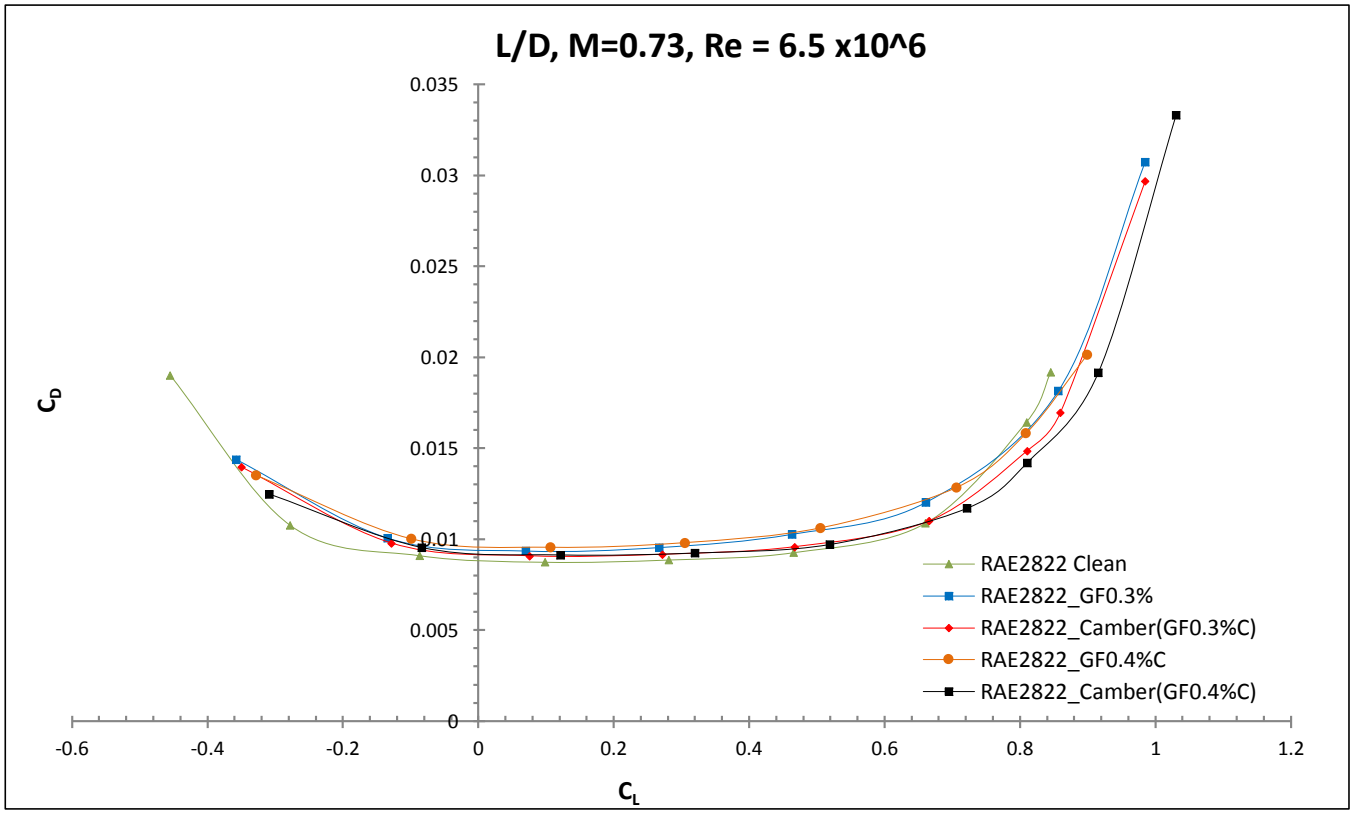

Figure 4.2.2.4, Aerodynamic efficiency (CL/CD)

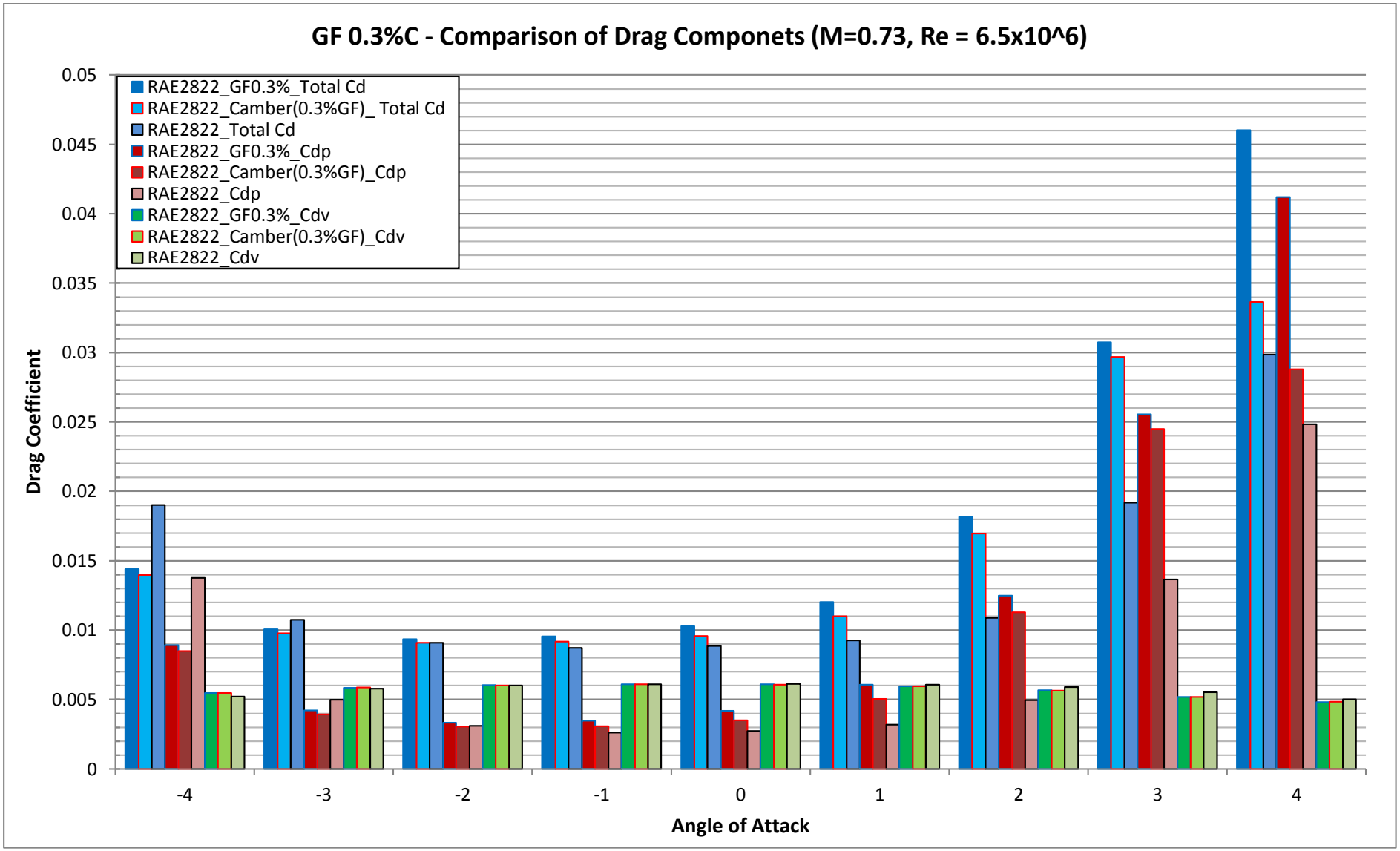

Figure 4.2.2.5, GF 0.3%C - Comparison of Drag Components (M=0.73, Re = 6.5x10^6)

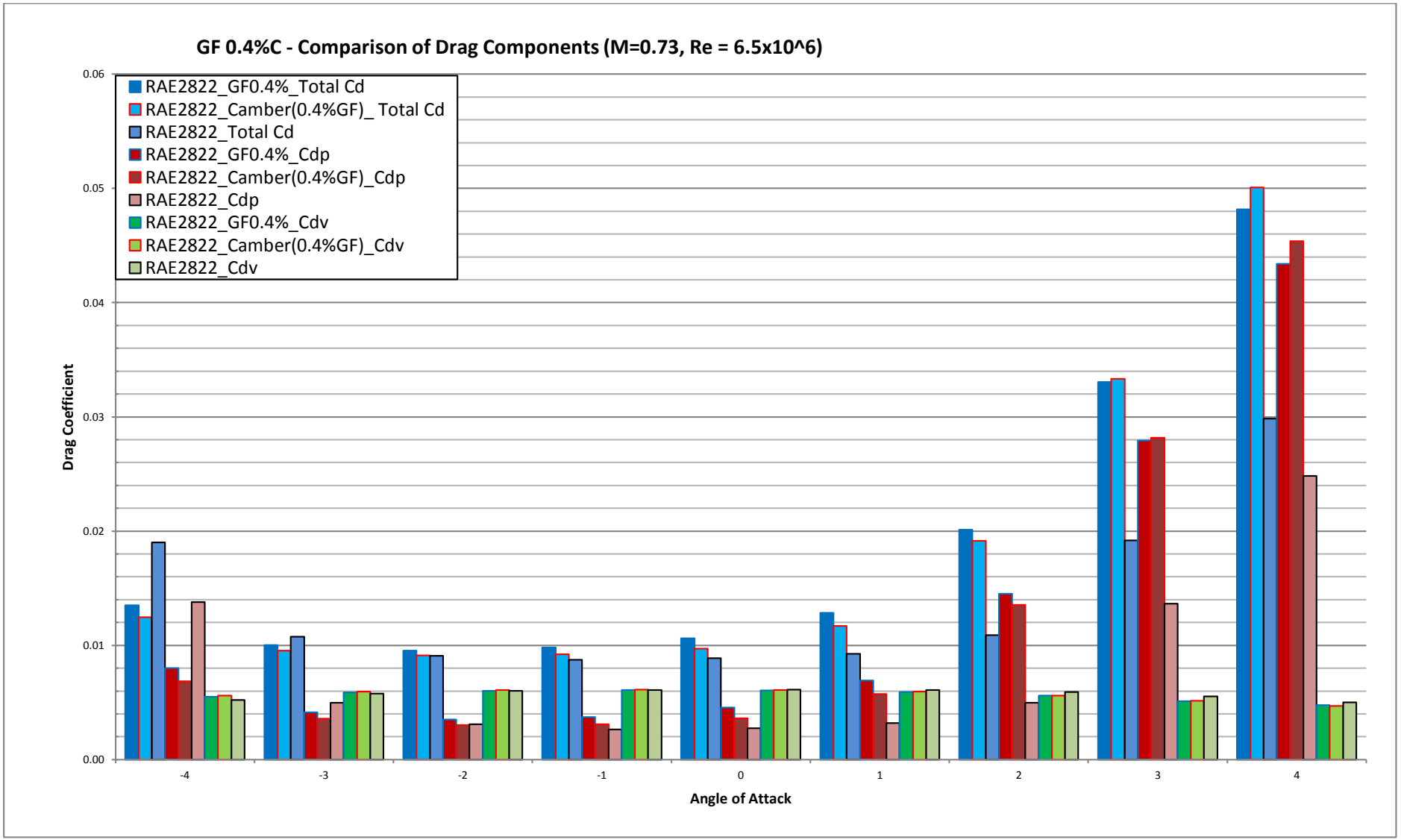

Figure 4.2.2.6, GF 0.4%C - Comparison of Drag Components (M=0.73, Re = 6.5x10^6)

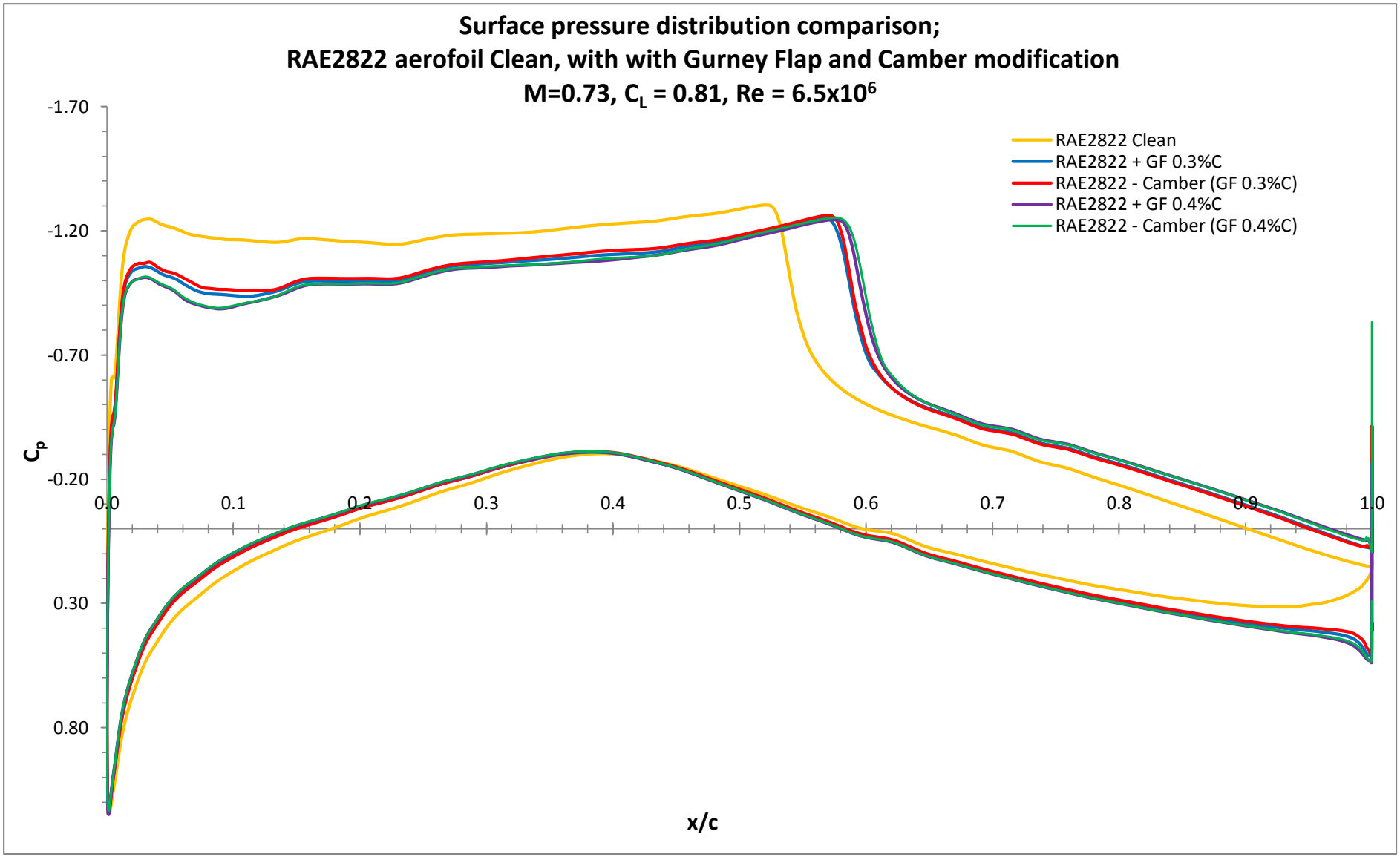

Figure 4.2.2.7, Surface pressure distribution, RAE2822 and modification, M=0.73, Re = 6.5x10^6)

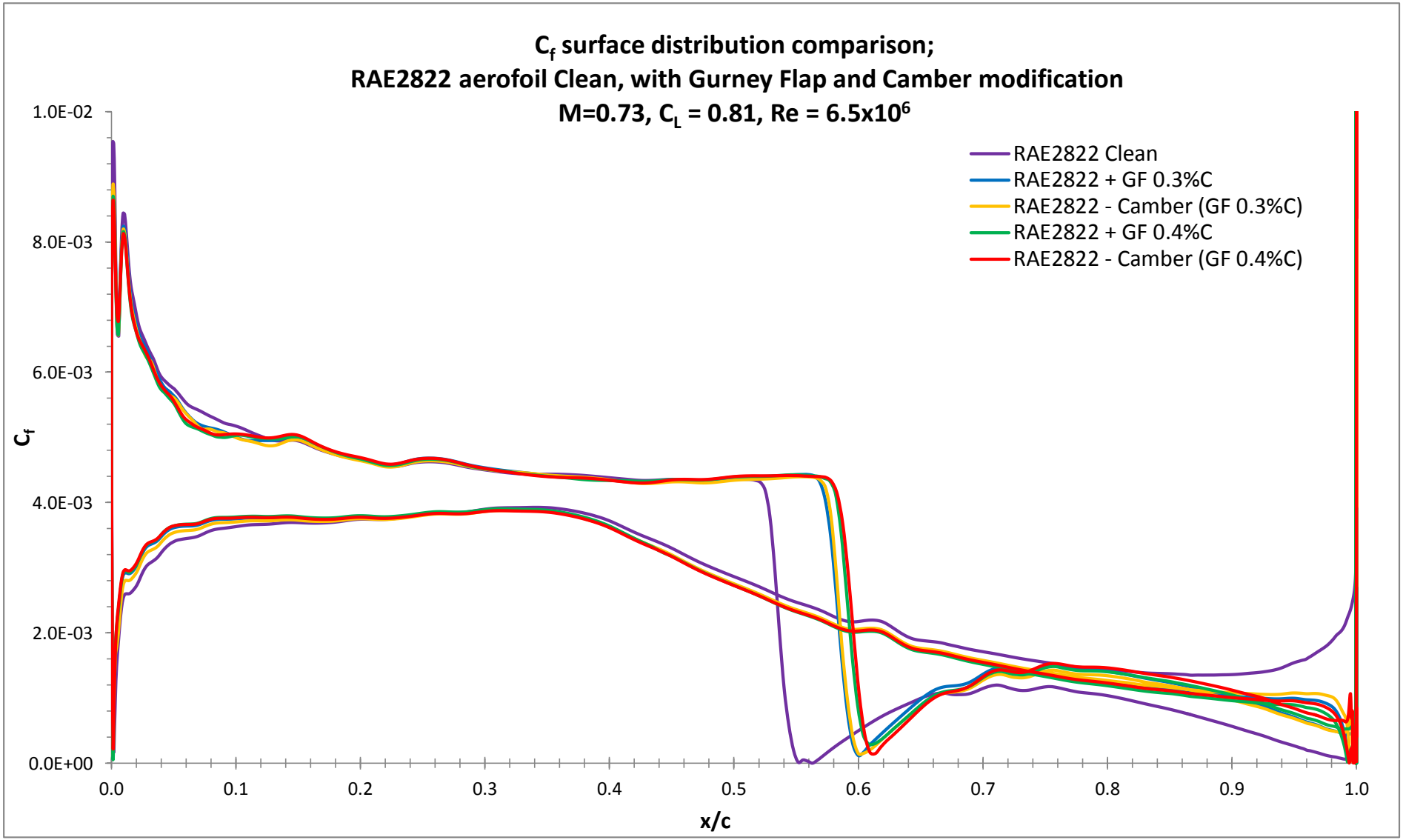

Figure 4.2.2.8, C_f Surface distribution, RAE2822 and modification, M=0.73, Re = 6.5x10^6)

a)

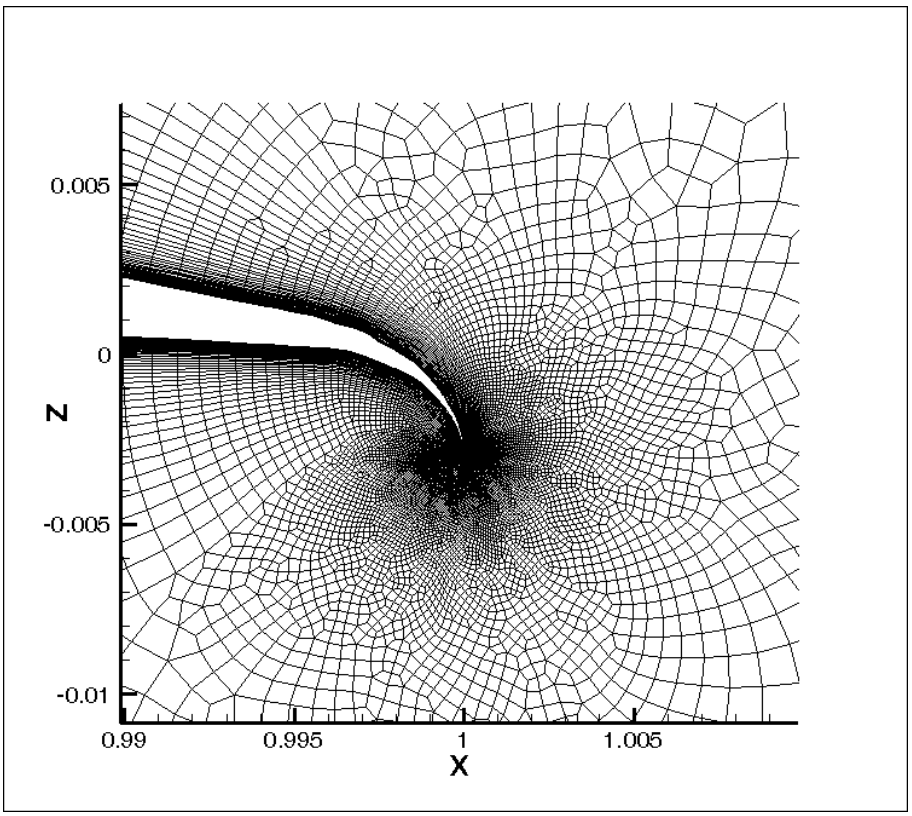

b)

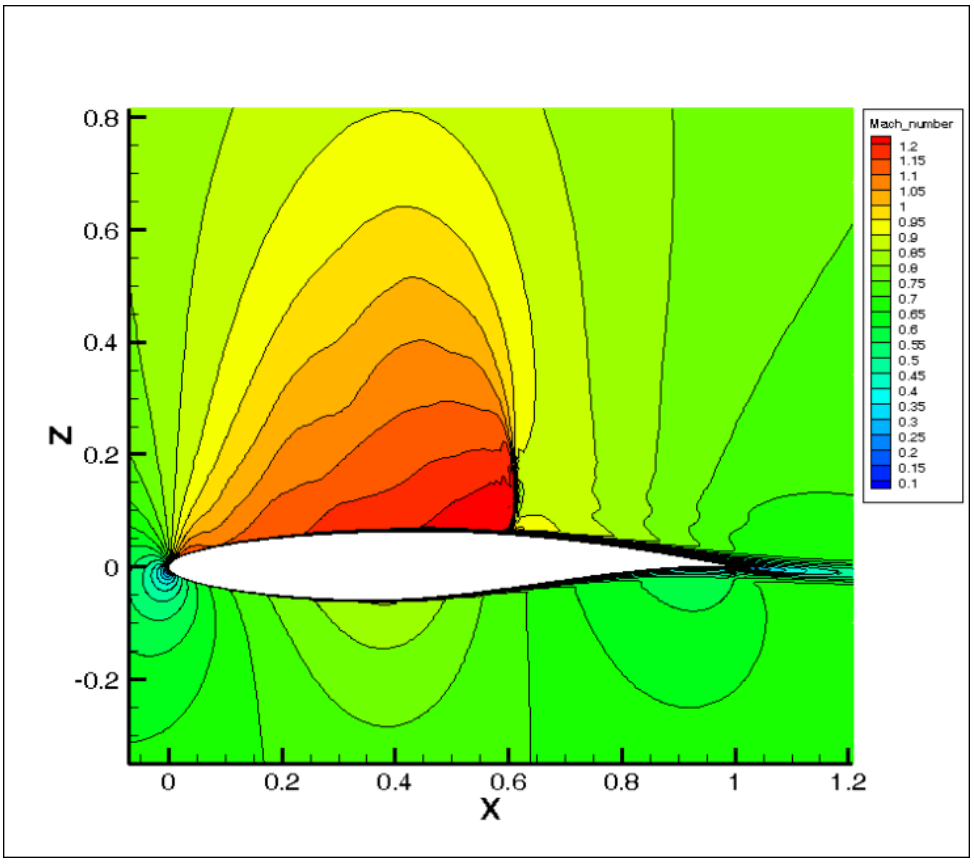

Figure 4.2.2.9a, b, RAE2822_Camber(GF_0.4%C) @CL=0.81

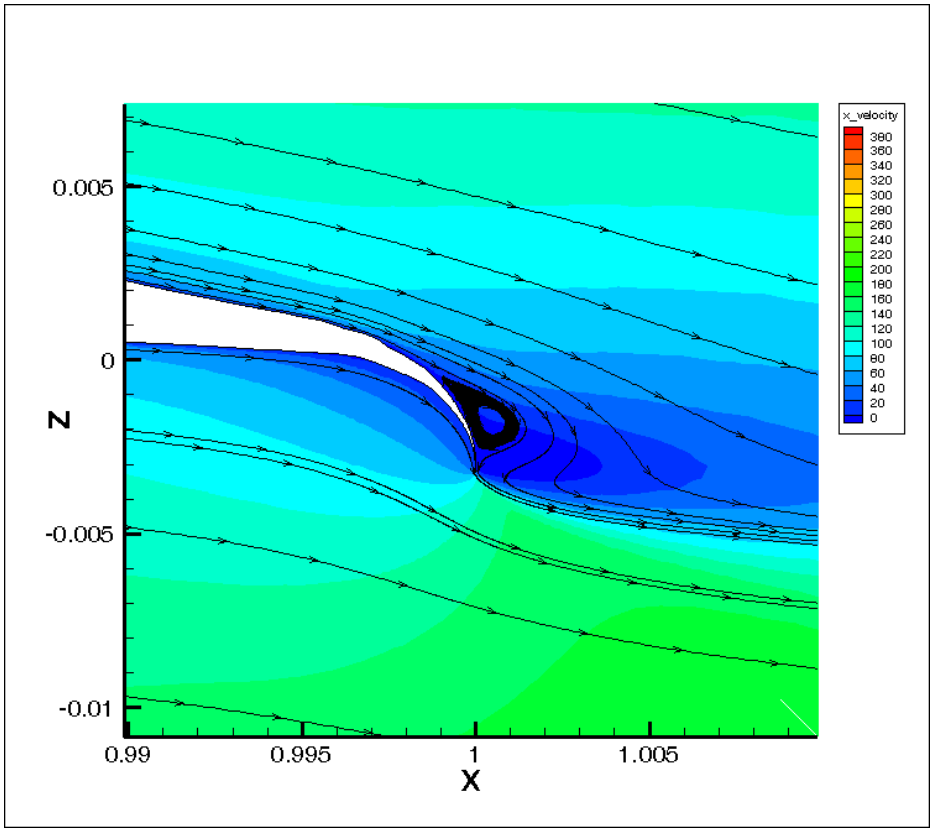

Figure 4.2.2.10a, RAE2822_Camber(GF_0.4%C) @CL=0.81 Figure 4.2.2.10b, RAE2822_Camber(GF0.3%)

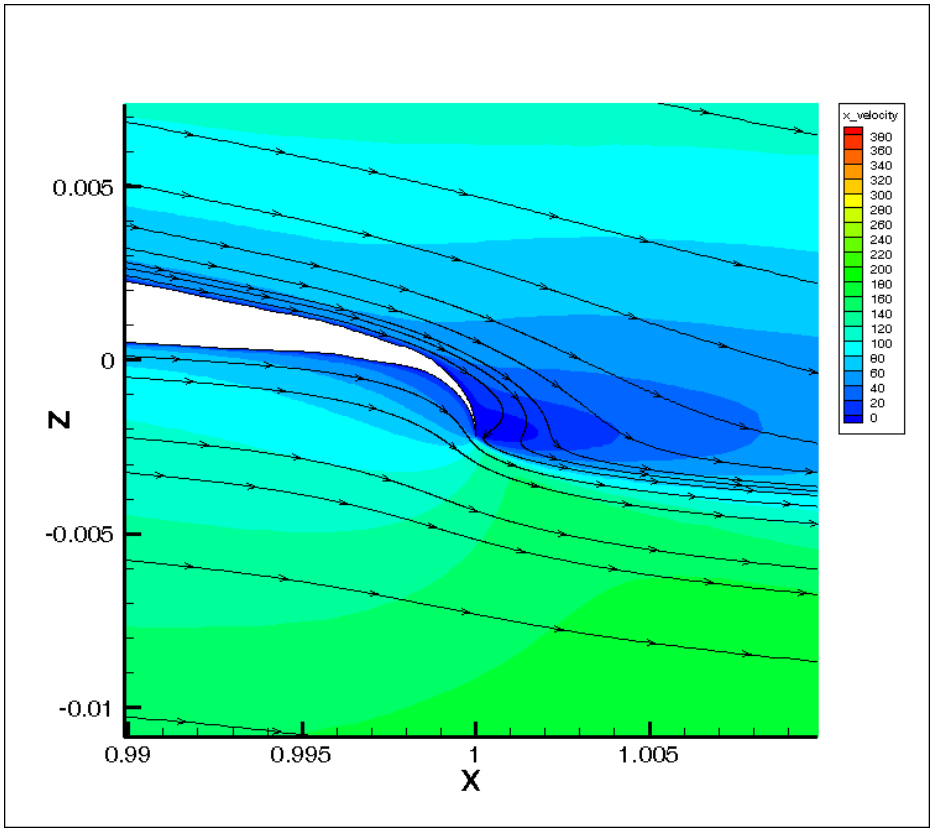

Figure 4.2.2.10a, RAE2822_Camber(GF_0.4%C) @CL=0.81 Figure 4.2.2.10b, RAE2822_Camber(GF0.3%)

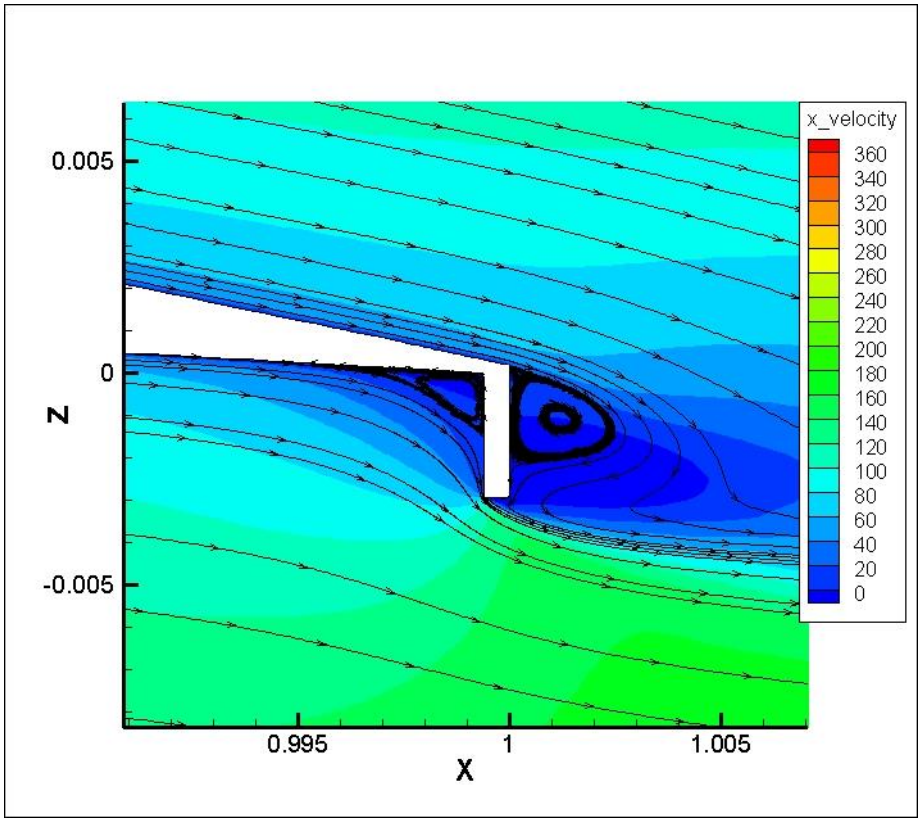

Figure 4.2.2.10c, RAE2822_GF_0.3%C @CL=0.81

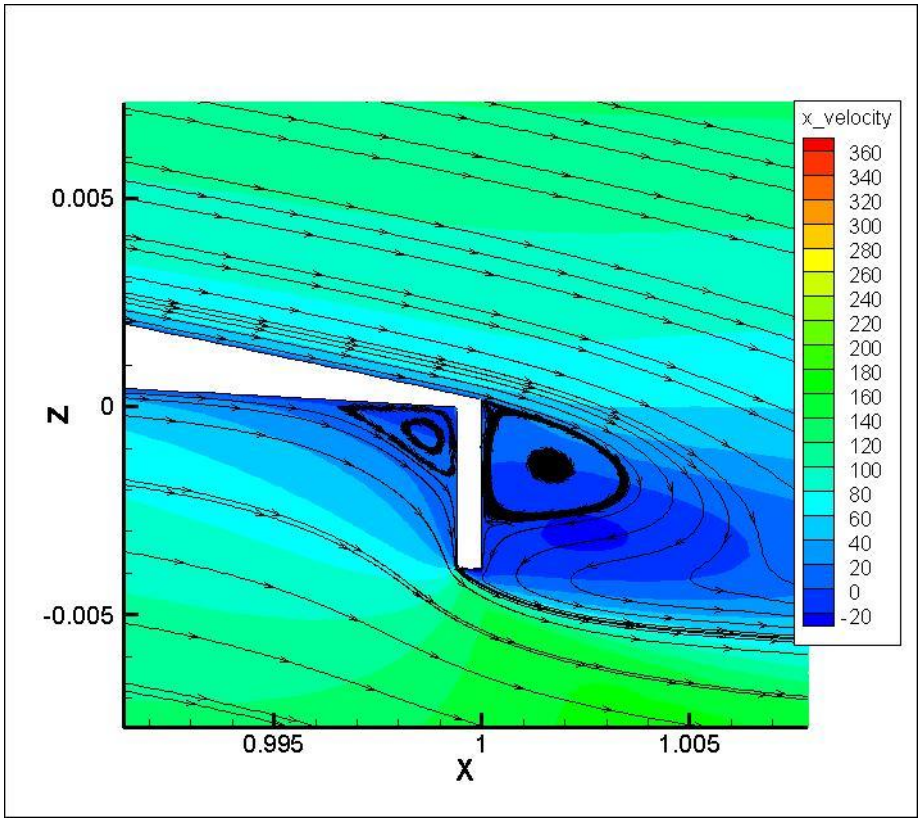

Figure 4.2.2.10d, RAE2822_GF_0.4%C @CL=0.81

4.2.3 Angled/tilted Gurney Flap investigation

The performance of Gurney Flap is greatly depending on the length of the flap. The larger flap can generate more disruptions, which results in larger vortex core both in front and after the flap. However, if the flap is too larger, the disruption can be too great and causes negative effectives and as well as Karman's vortex street. In previous section, the result suggests that s cambered trailing edge is more effective than conventional vertical drop flap. This brings the interests in investigating the effect on angled/ tilted Gurney flap. This experiment uses the 'optimum' Gurney flap length as a based, then by applying trigonometry and Pythagoras theorem with the desired tilt angle to determine the flap dimension. This can be seen in figure 4.2.3.1.

This study uses result obtained in previous sections, which concluded the effective flap length is between 0.5%c and 0.6%c. The simulation are performed at M=0.73, Re = 6.5 x 10^6 and lift constrained to C_L = 0.81. The 0.5%c Gurney flap geometry were modified through RBF mesh deformation in small steps (distance of x = 0.0001m) and applied into the simulations. The best geometry dimension is then obtained by selection. The geometry began with 0.5%c and end with 0.5902%c. Table 4.2.3.1 shows the performance comparison of the specimen test range. The results indicate that 0.5615%c Gurney flap produced the least drag and this length is selected for the tilted/ angled study.

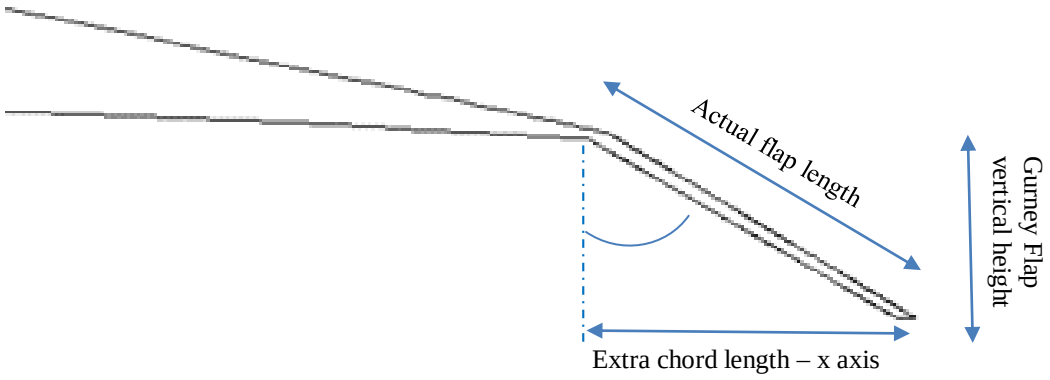

Figure 4.2.3.1, Tilt Gurney flap - Sketch

Four different geometries are used in this study with the constant vertical height and tilted angle of 35^o, 45^o, 60^o and 70^o. In order to provide a good comparison, the simulations are conducted in the same condition, M = 0.73, Re = 6.5 x 10^6, C_L = 0.81 and with S-A Turbulence Model. The simulated result, Table 4.2.3.1, indicates tilted 60^o has the most effective performance out of the 4 geometries.

Table 4.2.3.1

		C_L			C_D			C_M	L/D
Name	Alpha	C_{Ltotal}	C_{Lp}	C_{Lv}	C_{Dtotal}	C_{Dp}	C_{Dv}		
RAE2822 Clean	2.7900	0.8097	0.8096	0.0000	0.01644203	0.01081465	0.00562738	-0.1783	49.24
RAE2822 GF - 0.5%C	1.2999	0.8091	0.8090	0.0001	0.01559095	0.00980276	0.00578819	-0.2173	51.89
RAE2822 GF - 0.5164%	1.3000	0.8092	0.8092	0.0001	0.01558985	0.00980093	0.00578892	-0.2173	51.91
RAE2822 GF - 0.5328%	1.3000	0.8092	0.8092	0.0001	0.01558993	0.00980101	0.00578892	-0.2173	51.91
RAE2822 GF - 0.5492%	1.2999	0.8092	0.8092	0.0001	0.01558987	0.00980097	0.00578891	-0.2173	51.91
RAE2822 GF - 0.5533%	1.3000	0.8092	0.8092	0.0001	0.01559078	0.00980185	0.00578893	-0.2173	51.91
RAE2822 GF - 0.5574%	1.2999	0.8092	0.8092	0.0001	0.01558998	0.00980107	0.00578891	-0.2173	51.91
RAE2822 GF - 0.5615%	**1.2999**	**0.8092**	**0.8092**	**0.0001**	**0.01558957**	**0.00980066**	**0.00578891**	**-0.2173**	**51.91**
RAE2822 GF - 0.5656%	1.3000	0.8092	0.8092	0.0001	0.01559017	0.00980124	0.00578893	-0.2173	51.91
RAE2822 GF - 0.5820%	1.2999	0.8092	0.8092	0.0001	0.01559008	0.00980117	0.00578891	-0.2173	51.91
RAE2822 GF - 0.5902%	1.2999	0.8092	0.8092	0.0001	0.01559001	0.00980111	0.00578890	-0.2173	51.91

Table 4.2.3.2

		C_L			C_D			C_M	L/D
Name	Alpha	C_{Ltotal}	C_{Lp}	C_{Lv}	C_{Dtotal}	C_{Dp}	C_{Dv}		
35^o Degree	1.2242	0.8110	0.8109	0.0001	0.01563266	0.00984560	0.00578706	-0.2199	51.88
45^o Degree	1.2853	0.8110	0.8109	0.0001	0.01562780	0.00985411	0.00577369	-0.2187	51.89
60^o Degree	**1.4049**	**0.8110**	**0.8109**	**0.0001**	**0.01544582**	**0.00969067**	**0.00575515**	**-0.2159**	**52.51**
70^o Degree	1.2823	0.8109	0.8109	0.0001	0.01556354	0.00978534	0.00577820	-0.2186	52.10
RAE2822 GF - 0.5615%	1.2999	0.8092	0.8092	0.0001	0.01558957	0.00980066	0.00578891	-0.2173	51.91
RAE2822 Clean	2.7900	0.8097	0.8096	0.0000	0.01644203	0.01081465	0.00562738	-0.1783	49.24

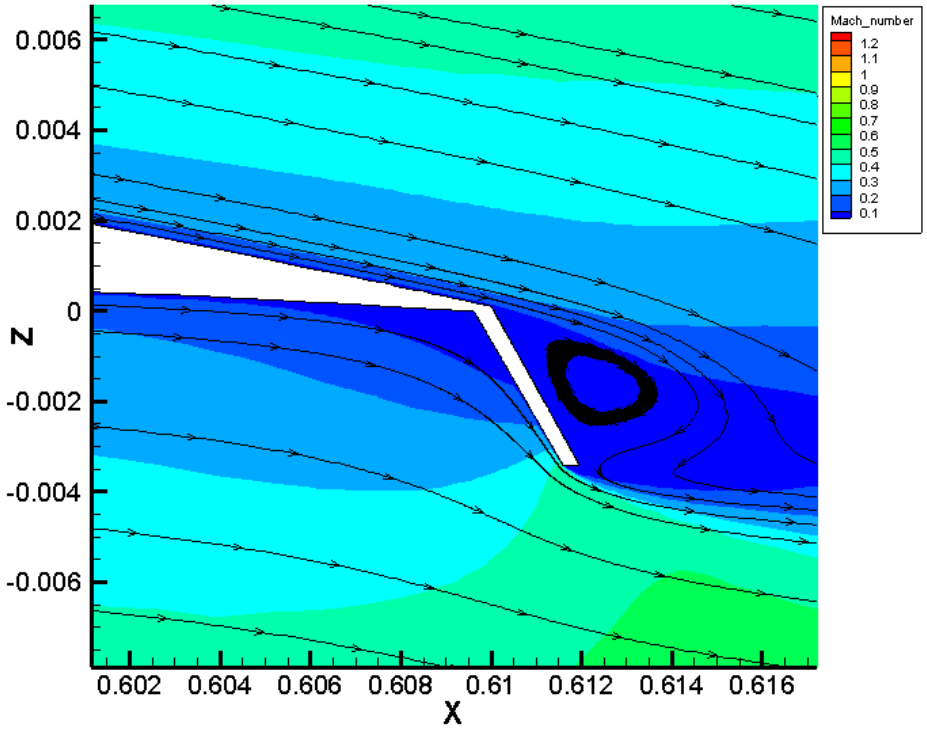

Figure 4.2.3.2a Tilted 35º Gurney flap

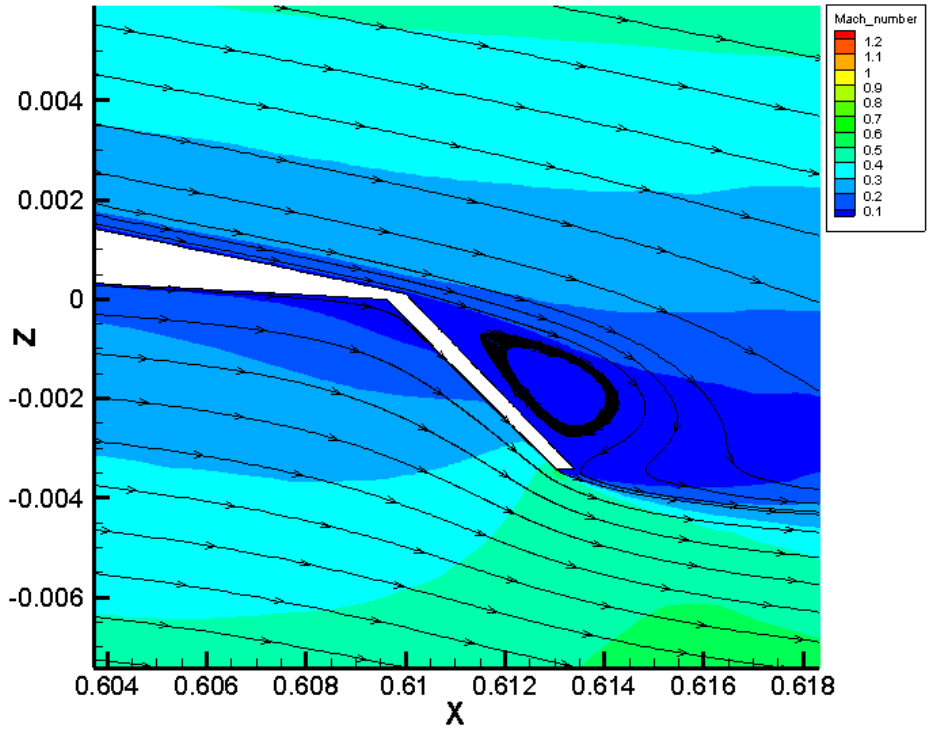

Figure 4.2.3.2b Tilted 45º Gurney flap

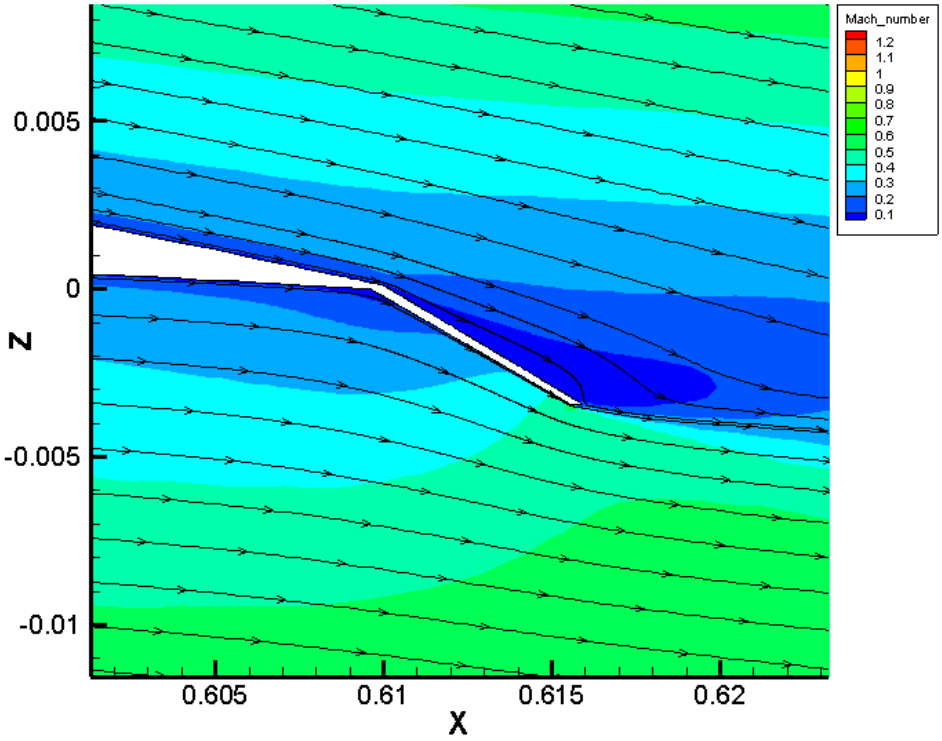

Figure 4.2.3.2c Tilted 60º Gurney flap

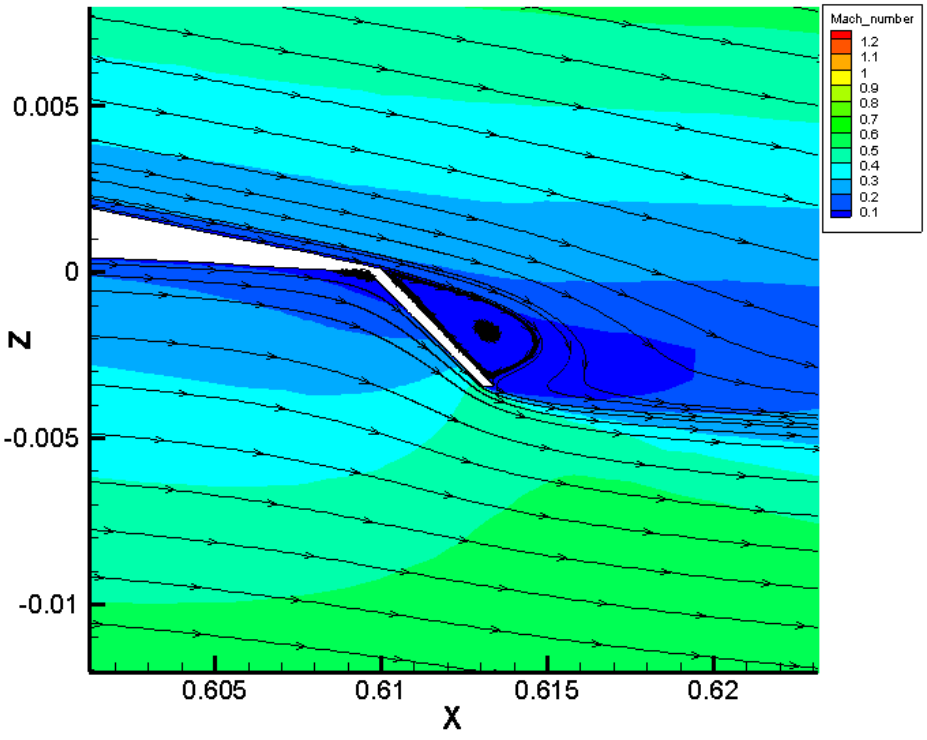

Figure 4.2.3.2d Tilted 75º Gurney flap

The main reason that 'Tilted 60° Gurney flap' produces the least drag can be represented on figure 4.2.3.2, the Tilted 60° geometry consists of no vortex, which means very little disruption, and 'Tilted 75° Gurney flap' has the smallest vortex core which in turn matches to the results shown in Table 4.2.3.2 . The Tilted 45° and 35° flap generates more disruption to the flow field and causes larger vortex, and therefore results higher drag then the smooth flow 'Tilted 60°'. However, in figure 4.2.3.3, it indicates the shock location lays almost the same for 'Tilted' Gurney flaps and original 0.5615%c flap, this mean the tilted angle flap performs as the 'theoretical flap vertical flap height' but with less drag if the vortex can be reduce or eliminated. This tilted flap behaviour is very similar to the study (trailing edge camber) conducted earlier.

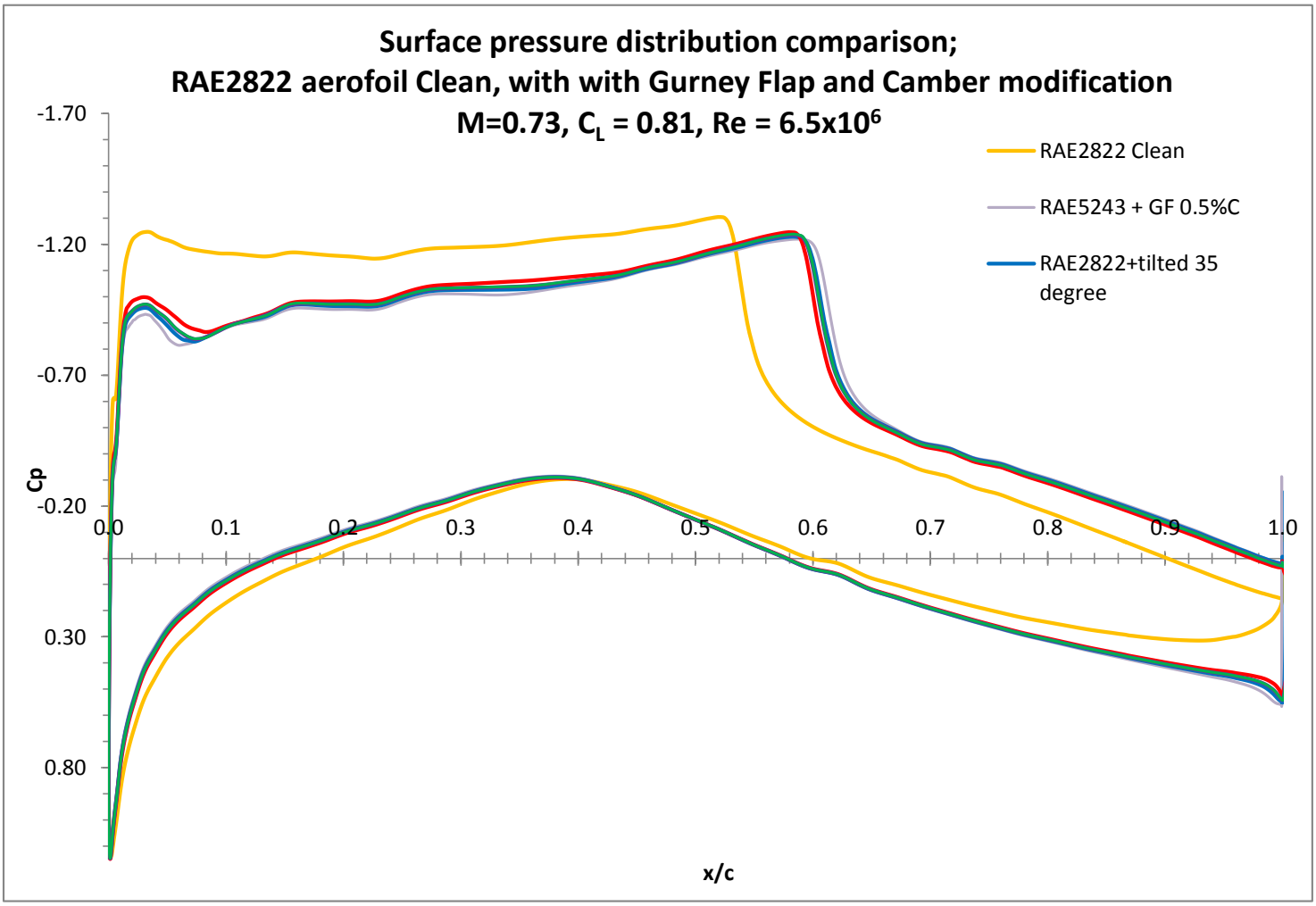

Figure 4.2.3.3 Pressure distribution

4.2.4 Shockbump and Gurney Flap[30]

The drag benefits of Gurney flap at transonic condition is suggested in earlier chapter, this drag reduction is achieved by shock delay downstream. However, the shockwave has not been weaken or diminish, it is just delayed or transfer moved downstream. A well-known transonic flow control device, Shockbump, this device is thought provide extra benefits to the drag reduction in additional to Gurney flap. The function of shock bump is to weaken the shock strength during transonic flight, thus reduces drag. The drag reduction is achieved by obtaining a compression of the flow immediately before the shock wave via local geometrical modification. In this study, Gurney flap (GF) and shockbump (SB) is used to investigate its effect on drag reduction at transonic condition.

The purpose of this research is to investigate the enhanced performance feature and feasibility of Gurney flap, less than 1%Chord (0.1%C to 0.7%C), on supercritical aerofoil (RAE2822). A combination of shock control bump and Gurney flap has been investigated. This includes investigations on lift constrain situation, at different angle of attack (-4^o to $+4^o$) and different Mach numbers.

The RAE2822 aerofoil along with GF and shockbump was simulated in three different Mach number; M = 0.72, 0.73 and 0.74 and with Re = 6.5×10^6 (based on the chord length of 0.61m). In the mesh independent study with AGARD case 9 condition, the RAE2822 creates a lift of $C_L = 0.81$. Lift constrained condition was also introduce to all the tested Mach numbers, with M = 0.73 as the designed condition. Figure 4.2.4.2 represent the surface pressure distribution of RAE2822 with shockbump, GF and combined of the two device together with $C_L = 0.81$ condition. The area under the curve in the pressure distribution graph represents the lift. In the all three different Mach number, it clearly shows that the addition of Gurney flap, from 0.1%C to 0.7%C length, all displayed a delay in shockwave downstream on the aerofoil. The amount of suction required to maintain the desired lift

condition is reduced with the aid of GF, this can also be seen on the shockbump scenario. This is because of the trailing edge of the aerofoil, there is an opening of Cp introduce, hence, the area under the curve retain the same but leading edge suction can be reduced as more suction is generated across the aerofoil. Therefore, with a smaller maximum suction point, the pressure difference are lessen, this results in a smaller shock. In the C_f plots at figure 4.2.4.2, it clearly shows in the clean aerofoil condition, at M = 0.72, a shockwave was present but not enough to cause shock induced separation, whereas for M = 0.73 and 0.74 a shock induced separation occurred then follows by a reattachment. The M = 0.72 cases suggests that GF reduces the normal shockwave, at M = 0.73 the GF addition removes the shock induce separation, and at M = 0.74 the GF only moves the normal shock downstream but no other effects can be seen.

In the Shockbump case, the results indicates that the shockbump induced a rapid pressure difference at the leading edge, this is due to designed geometry of the shockbump. At designed condition M = 0.73, Re = 6.5 x 10^6 and C_L = 0.81, it indicates a reduction of 20.52% in drag. And in off-design M = 0.74, it shows a 13.10% drag reduction. However, in M = 0.72, the off-designed shockbump causes substantial increase in drag, 11.60% drag increase. This adverse effect is generated because of the shock been shifted forward by the bump and also a secondary large shock been formed by the accelerated flow due to the curvature of the shockbump. The addition of GF to the SB, shows no positive performance gain in this form of combination. The GF again demonstrates its ability to shift the normal shockwave downstream, which in fact pushing the pressure difference region in to the bump geometry and causes flow accelerating. Thus, a larger shockwave has formed and reduces the shockbump performance. This can be seen on the C_f plot at figure 4.2.5.2.

Figure 4.2.5.3 displays the reduction in pressure drag only with GF addition, the skin friction drag is unaffected. This effect can be seen as a virtual camber alteration, the GF alters the effective camber of the aerofoil, thus lowers the required angle of attack for the specific required lift. This camber

alteration effect is caused by the rotational vortex induced by the GF. In figure 4.2.5.5, GF is robust can be applied to off-designed condition and still achieve a good drag reduction. The simulated data suggests that GF alone can produce positive benefit in drag reduction for all three tested Mach number; with the highest Mach number (M = 0.74) benefits the most, a reduction of 17.5 % drag and M = 0.72 benefits the least, a maximum reduction of only 10.3 % drag.

The aerofoil with Gurney flap attached shows a substantial increment in lift-to-drag compared with clean aerofoil. This benefit can be seen on all lift constrained cases irrespective of the flap height. On the other hand, shockbump outperform GF at the designed condition, but causes large penalty in off-designed region or combined with GF. This can be seen on figure 4.2.5.4 and 4.2.5.5.

In the overall performance, $-4^{o} \leq \alpha \leq +4^{o}$, RAE2822 has a peak L/D at around 60+ during M = 0.73. The aerofoil in this Mach number can achieve the highest L/D, which outperform the Shockbump and GF. However, during high lift condition, i.e. $C_L = 0.82$, the clean aerofoil is its tough and reducing its aerodynamic efficiency. The shockbump and GF addition extends the aerofoil's lift generation, thus, provides a better performance in high lift condition. The combination of shockbump and GF shows negative effects and large reduction in L/D. For condition at M = 0.72, the GF shows a large improvement in the maximum L/D ratio, but the peak is shifted towards lower C_L, however, for the designed lift condition of $C_L = 0.82$, there is still a large improvement can be seen. Shockbump shows no positive characteristic in comparison to the normal lift range of clean RAE2822, an extended lift range can be seen from the shockbump. There are no actual benefits with the combination of Shockbump with GF. For the M = 0.74 case, the GF extends the L/D curve of the clean RAE2822 aerofoil. This addition of GF increases the range of lift generated from the aerofoil as well as increase the maximum aerodynamics efficiency. Again, shockbump and shockbump with GF displays a reduction in aerodynamic efficiency but an extension in the lift range generated.

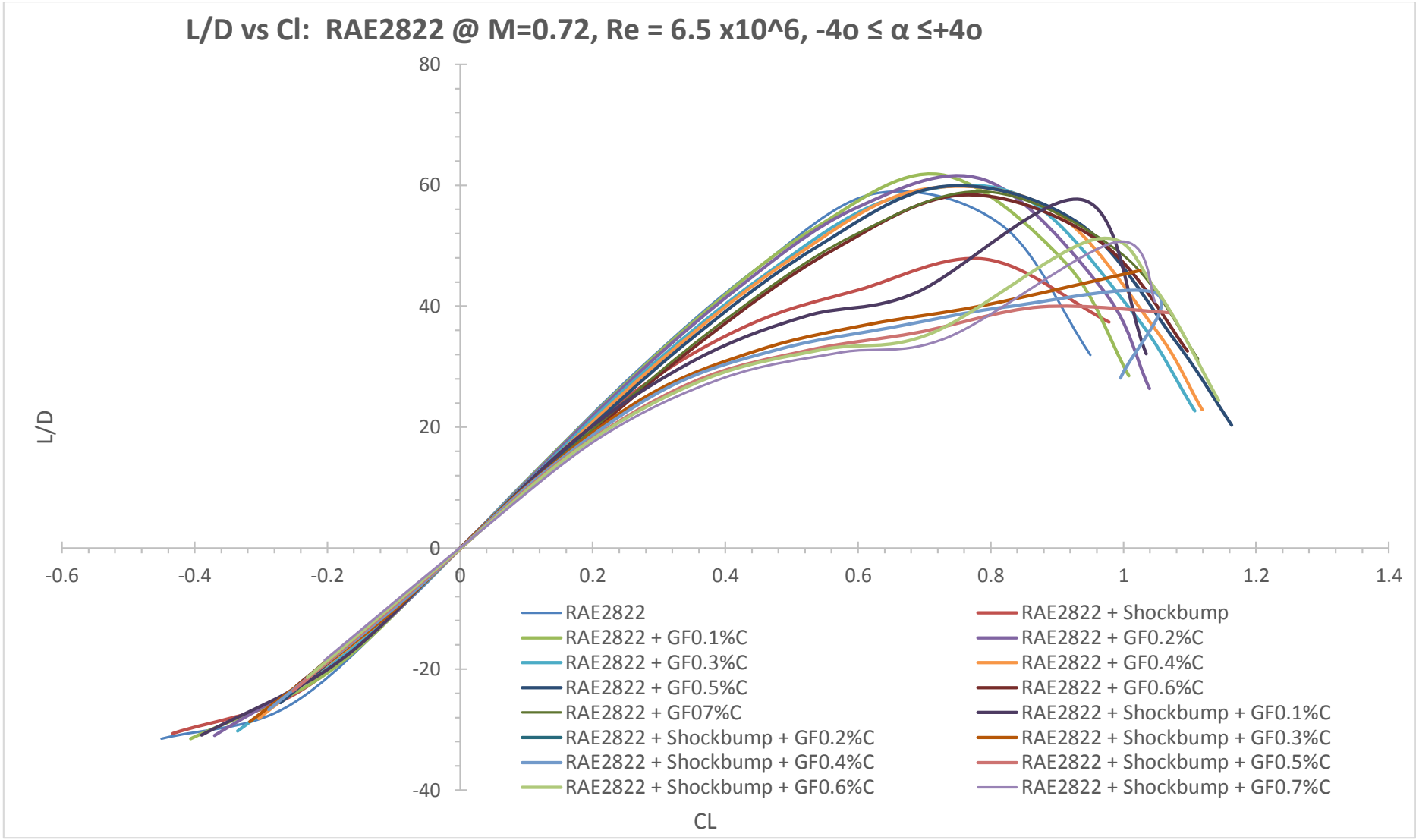

Figure 4.2.4.1a Lift-to-drag ratio vs C_L for RAE2822, Re = $6.5x10^6$, $-4^o \leq \alpha \leq +4^o$ (a) M=0.72

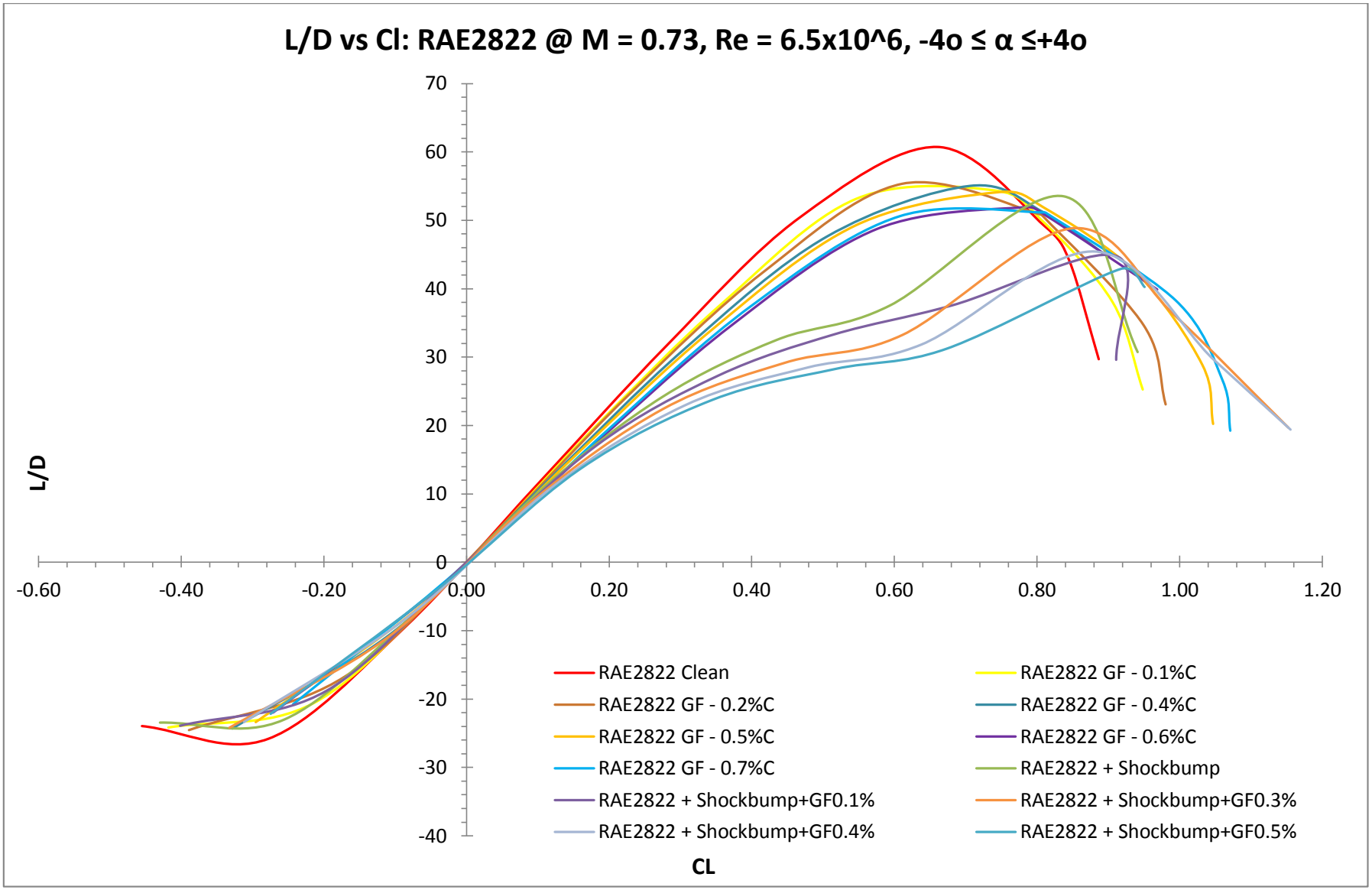

Figure 4.2.4.1b Lift-to-drag ratio vs C_L for RAE2822, Re = $6.5x10^6$, $-4^o \leq \alpha \leq +4^o$ (b) =0.73

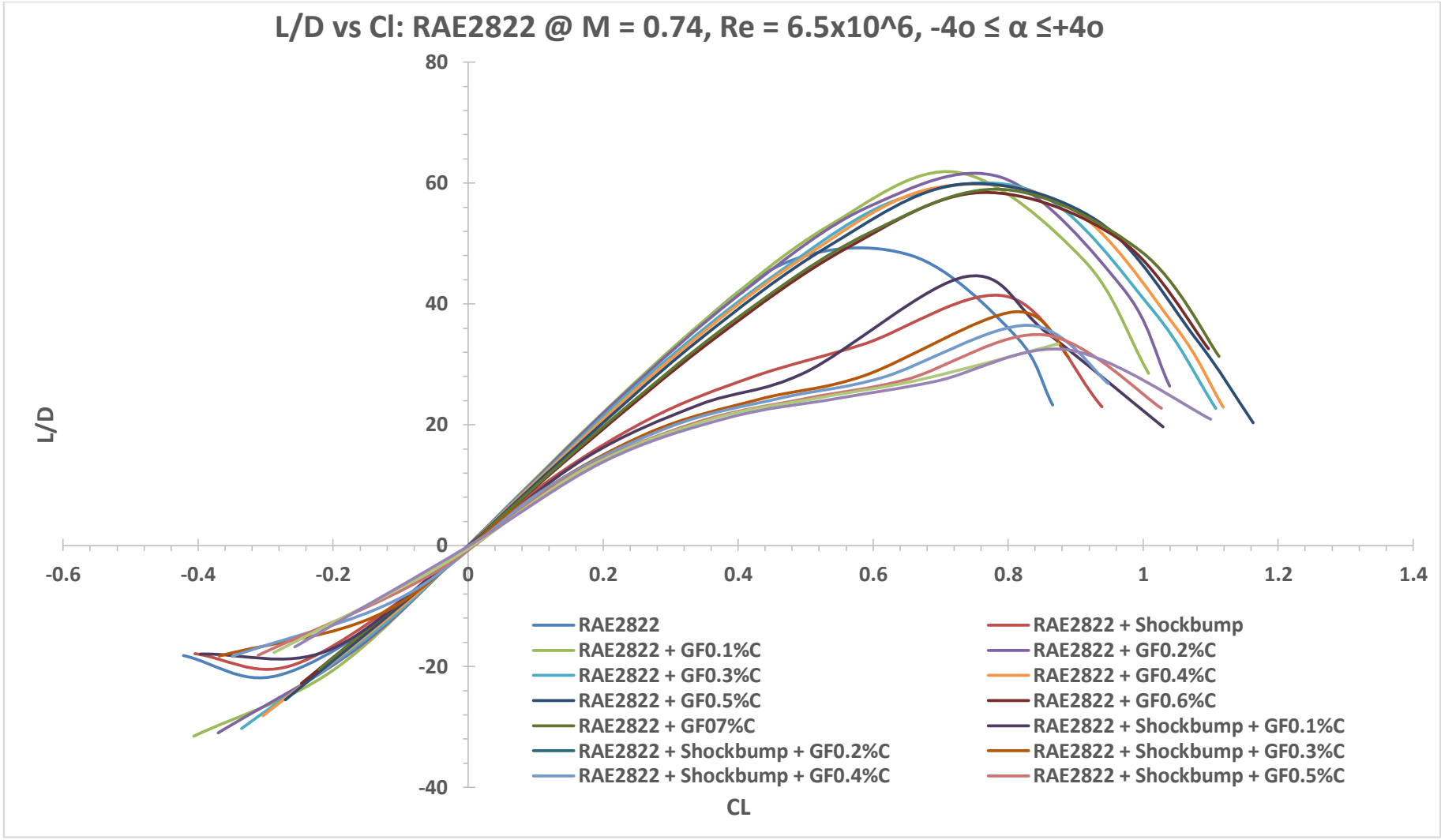

Figure 4.2.4.1c Lift-to-drag ratio vs C_L for RAE2822, Re = $6.5x10^6$, $-4^o \leq \alpha \leq +4^o$ (c) M=0.73

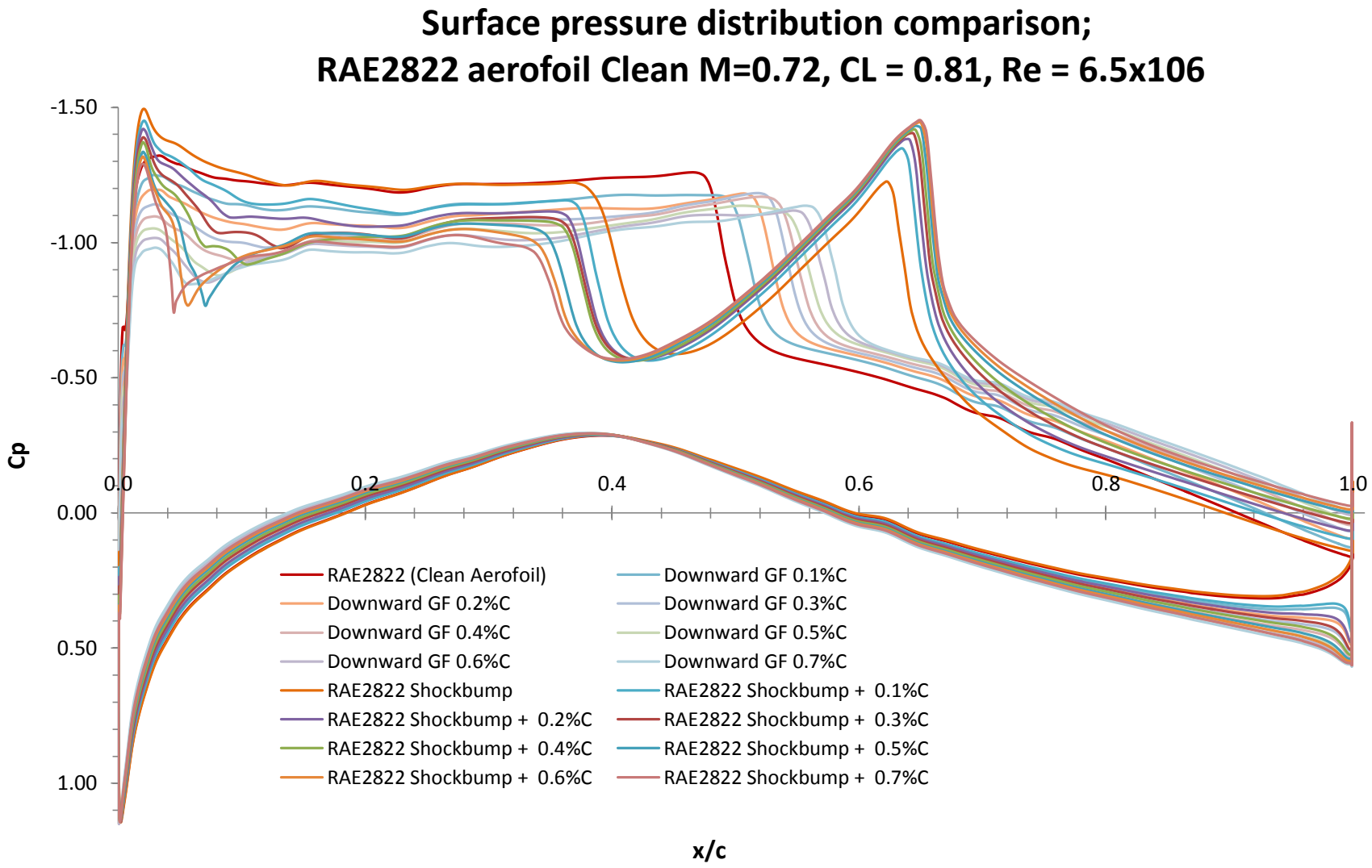

Figure 4.2.4.2a C_p, Surface pressure distribution for RAE2822 and flow control devices, a) @M = 0.72

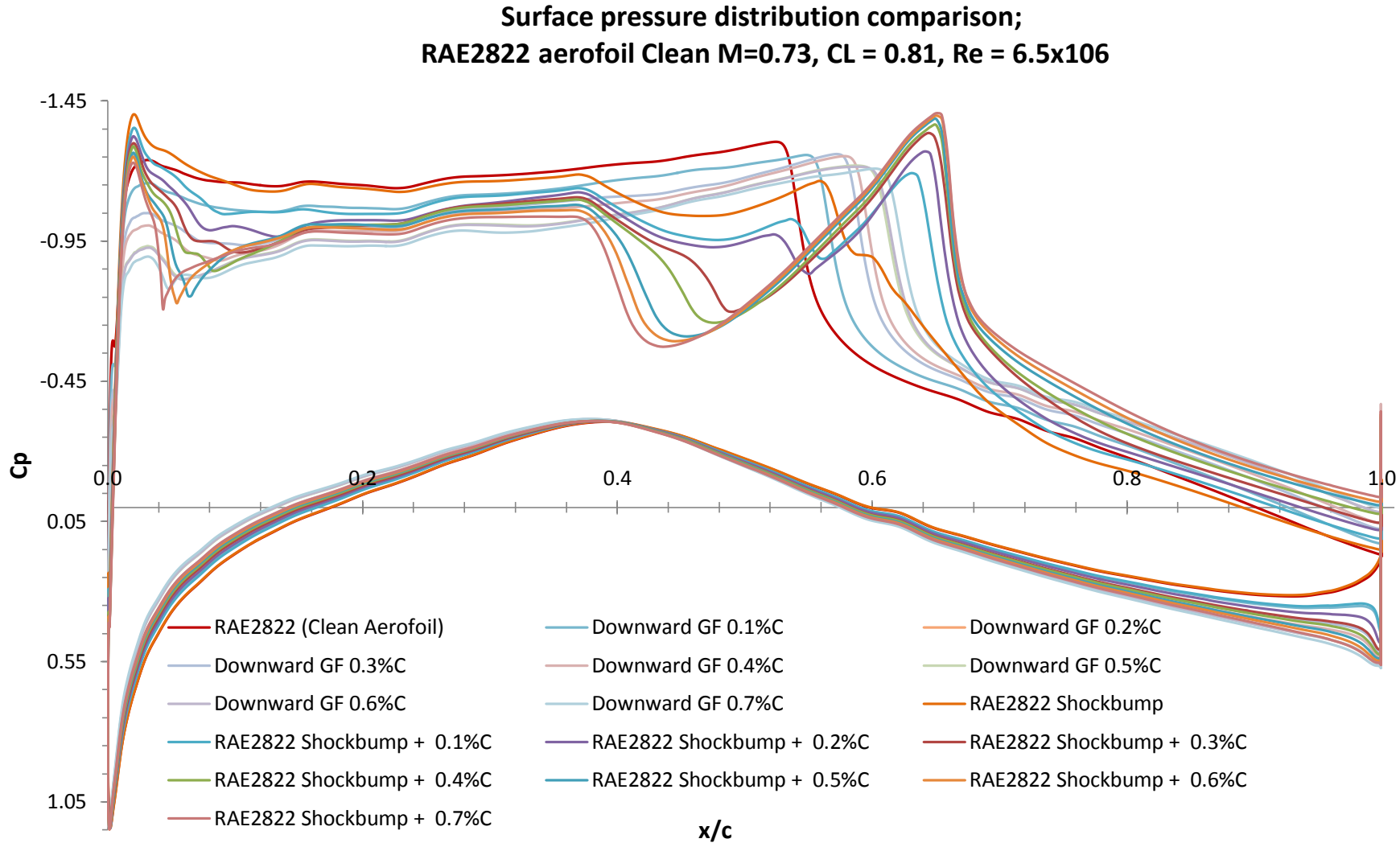

Figure 4.2.4.2b C_p, Surface pressure distribution for RAE2822 and flow control devices, b) @M = 0.73

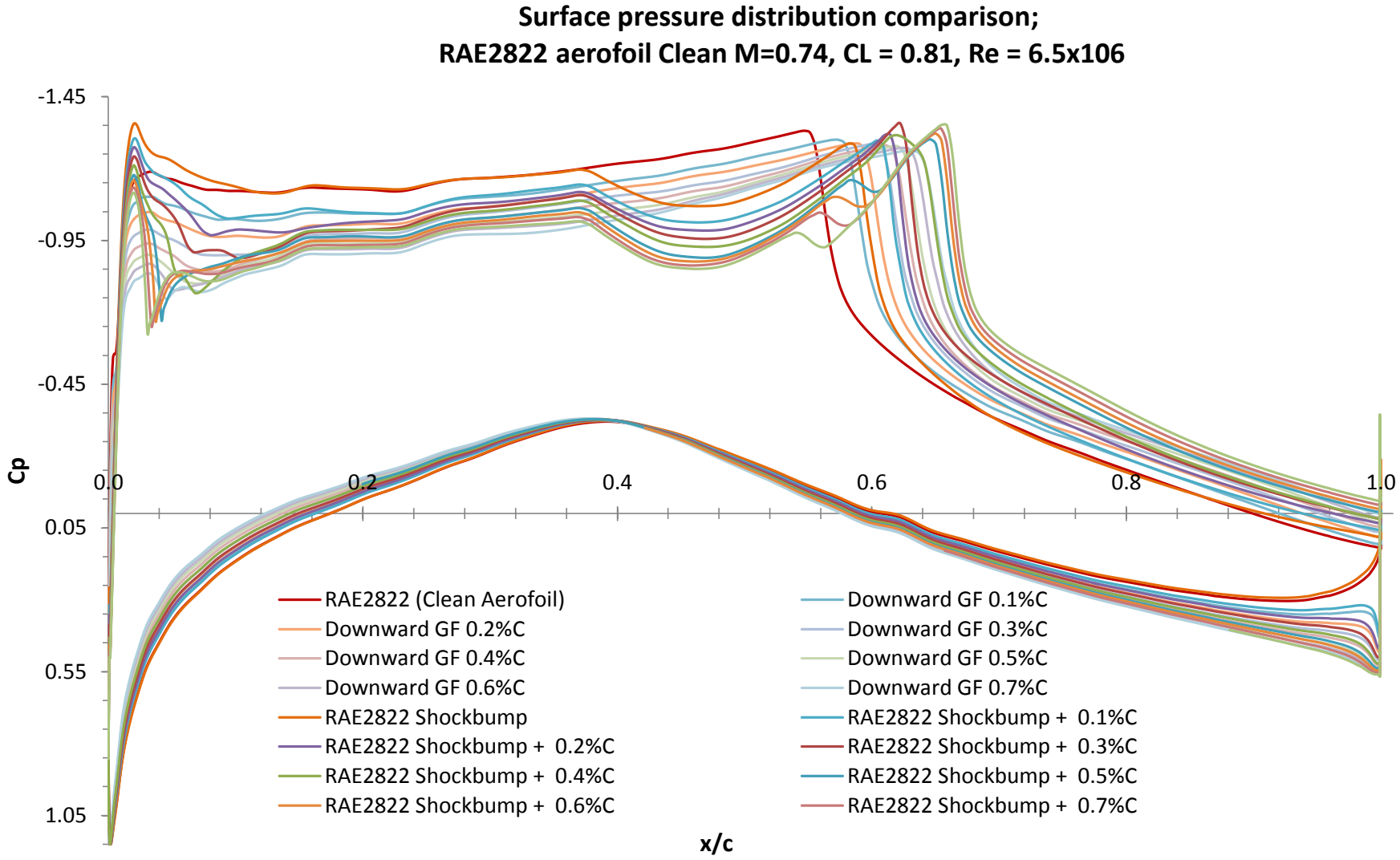

Figure 4.2.4.2c C_p, Surface pressure distribution for RAE2822 and flow control devices, c) @M = 0.74

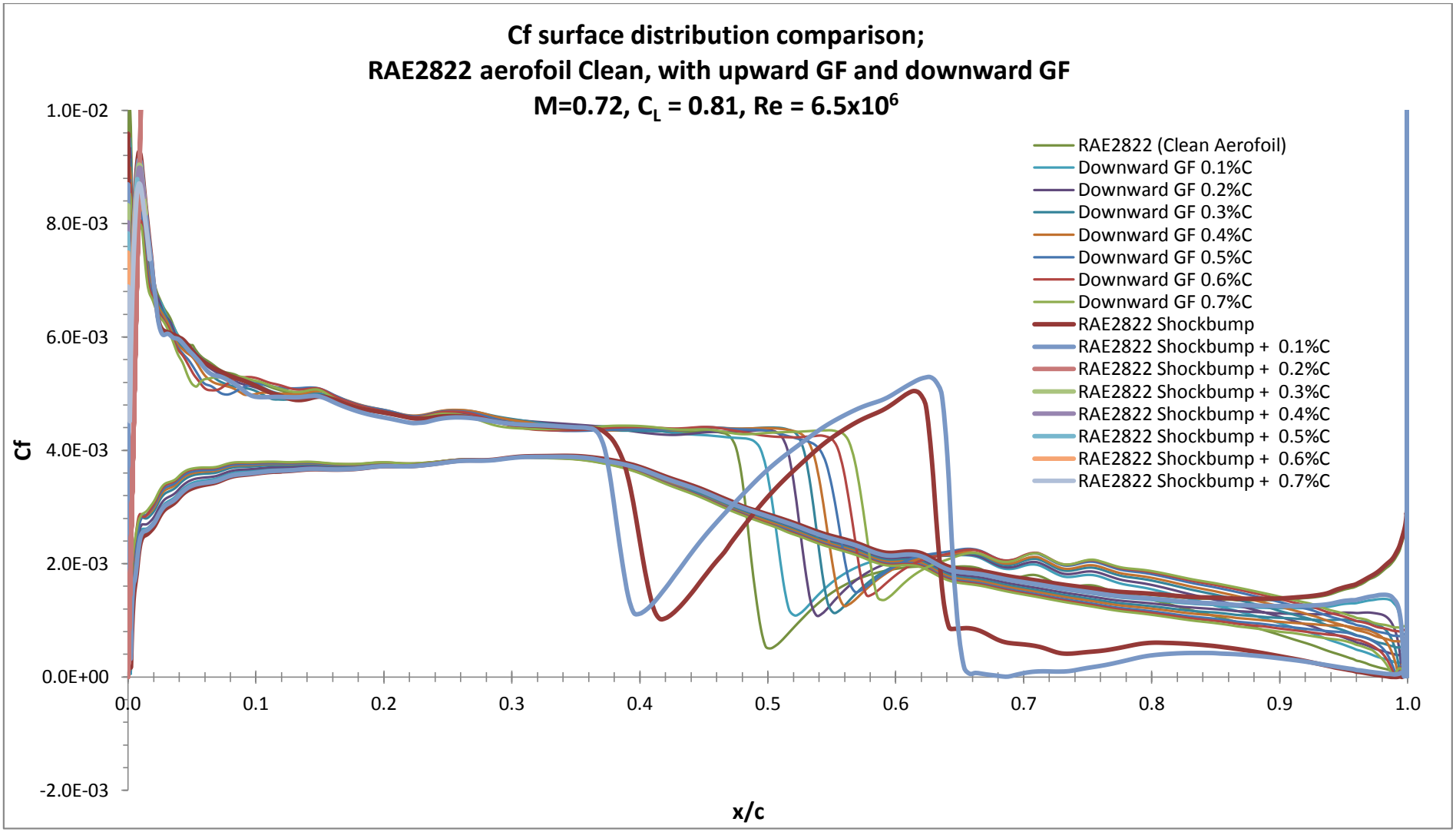

Figure 4.2.4.2d Cf surface distribution for RAE2822 d) @M = 0.72

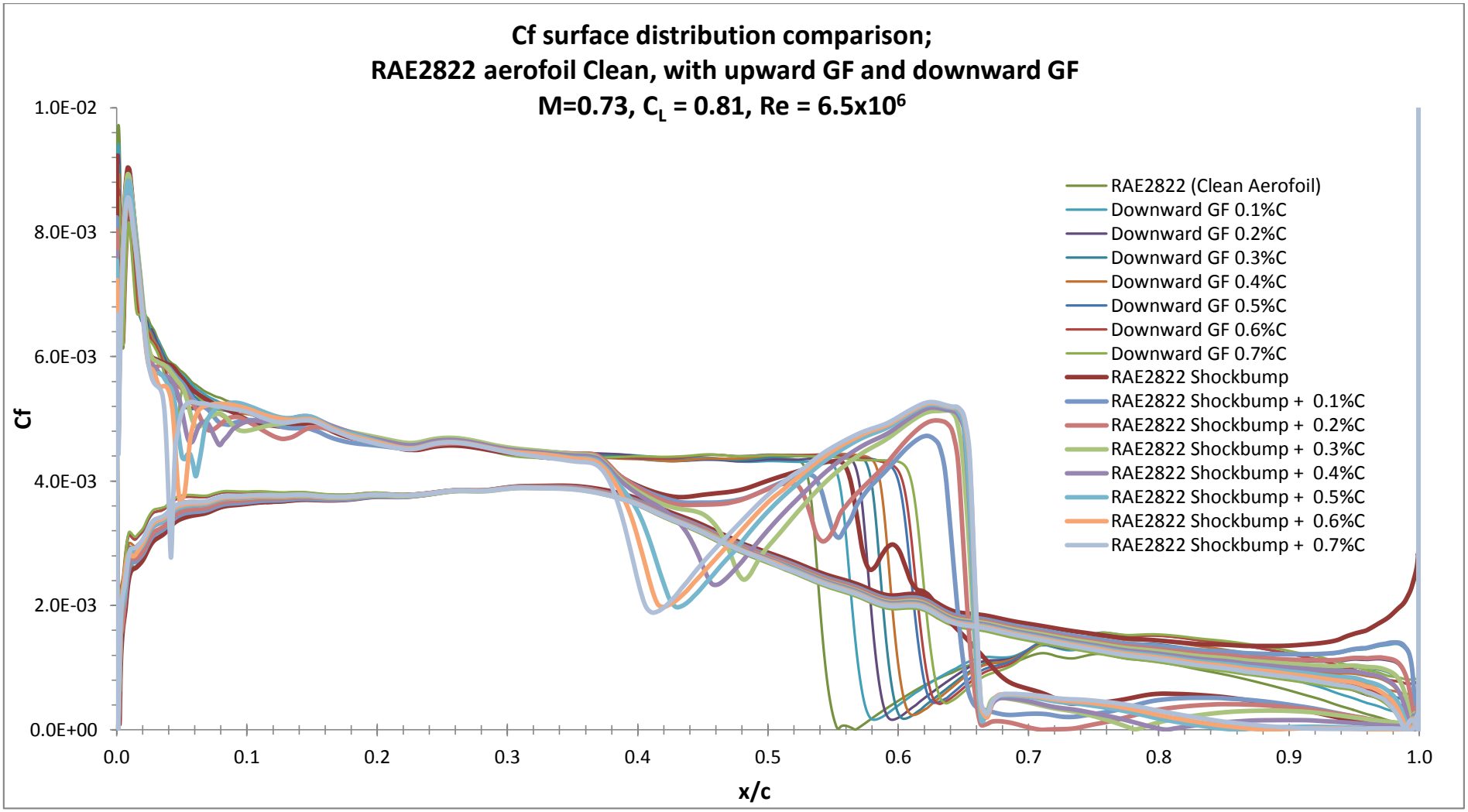

Figure 4.2.4.2e Cf surface distribution for RAE2822 e) @M = 0.73

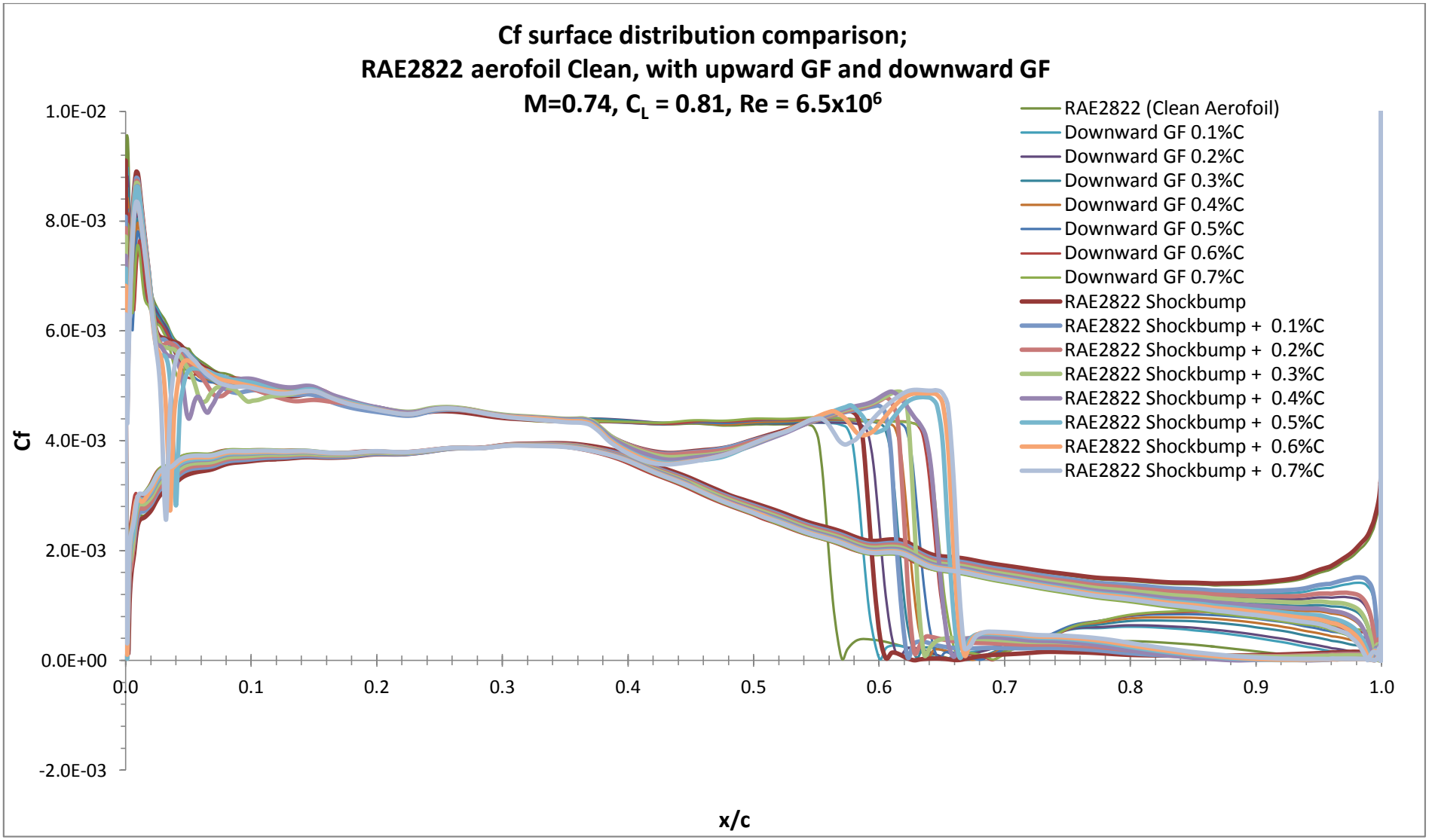

Figure 4.2.4.2f Cf surface distribution for RAE2822 f) @M = 0.74

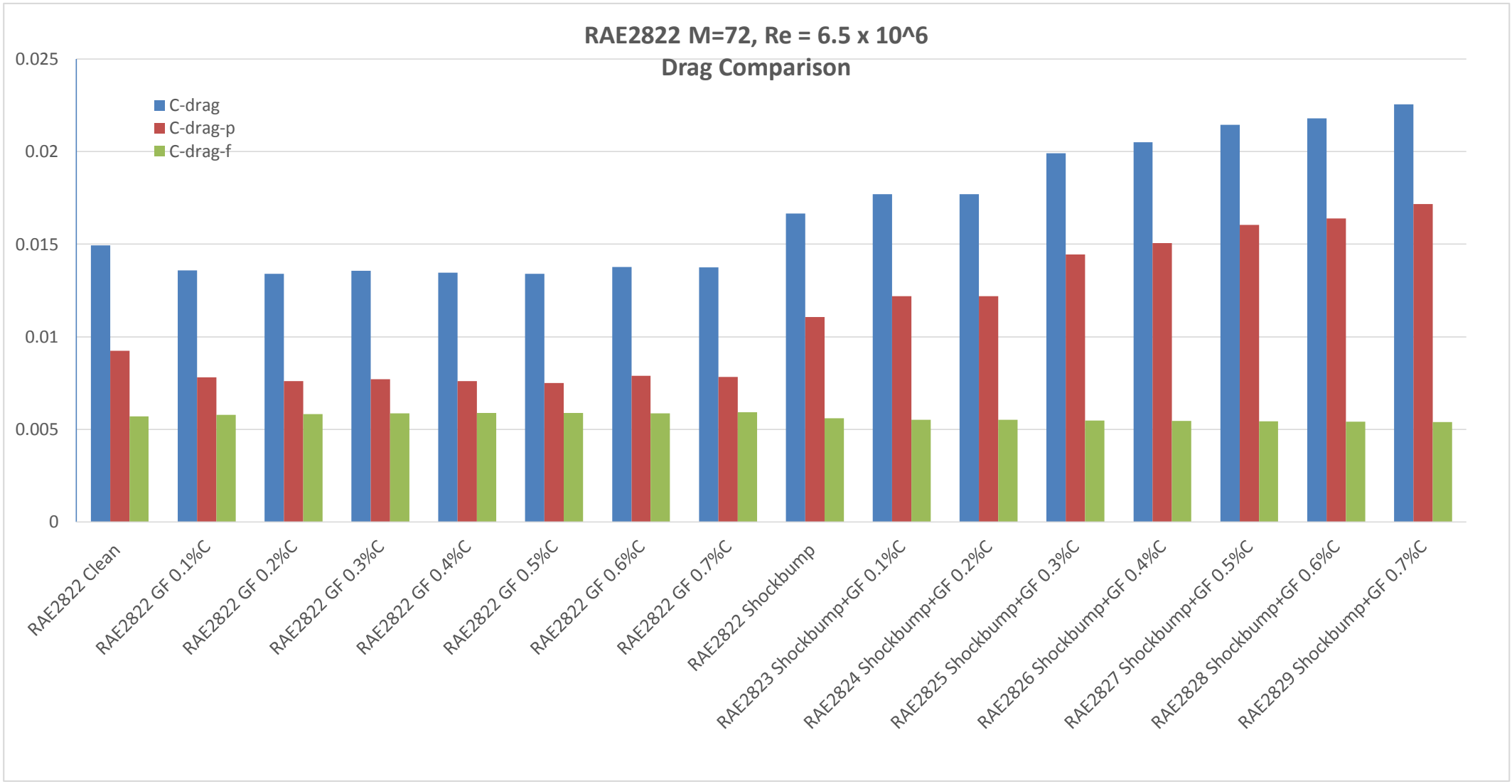

Figure 4.2.4.3a Drag component breakdown a) @M = 0.72

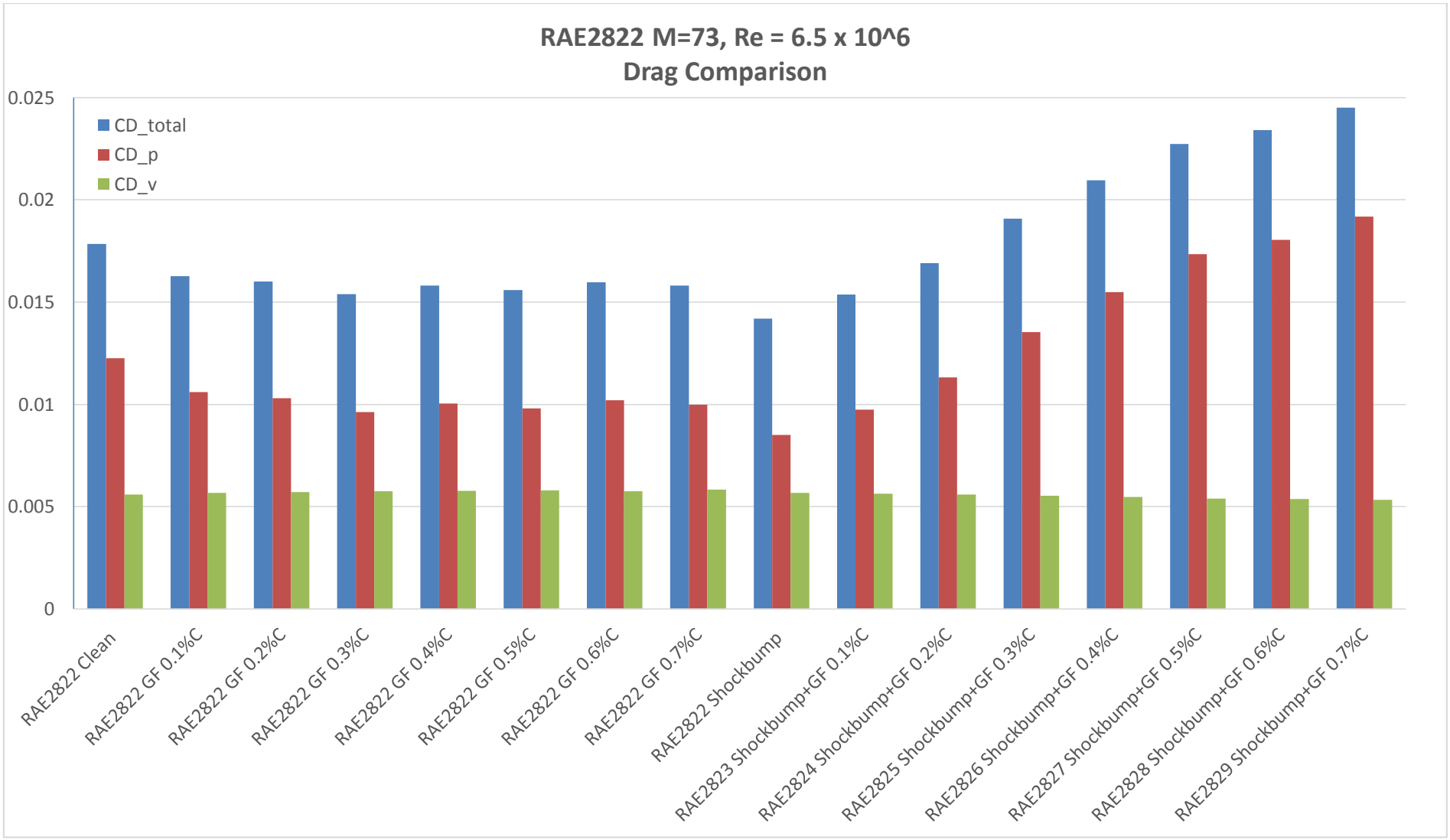

Figure 4.2.4.3b Drag component breakdown b) @M = 0.73

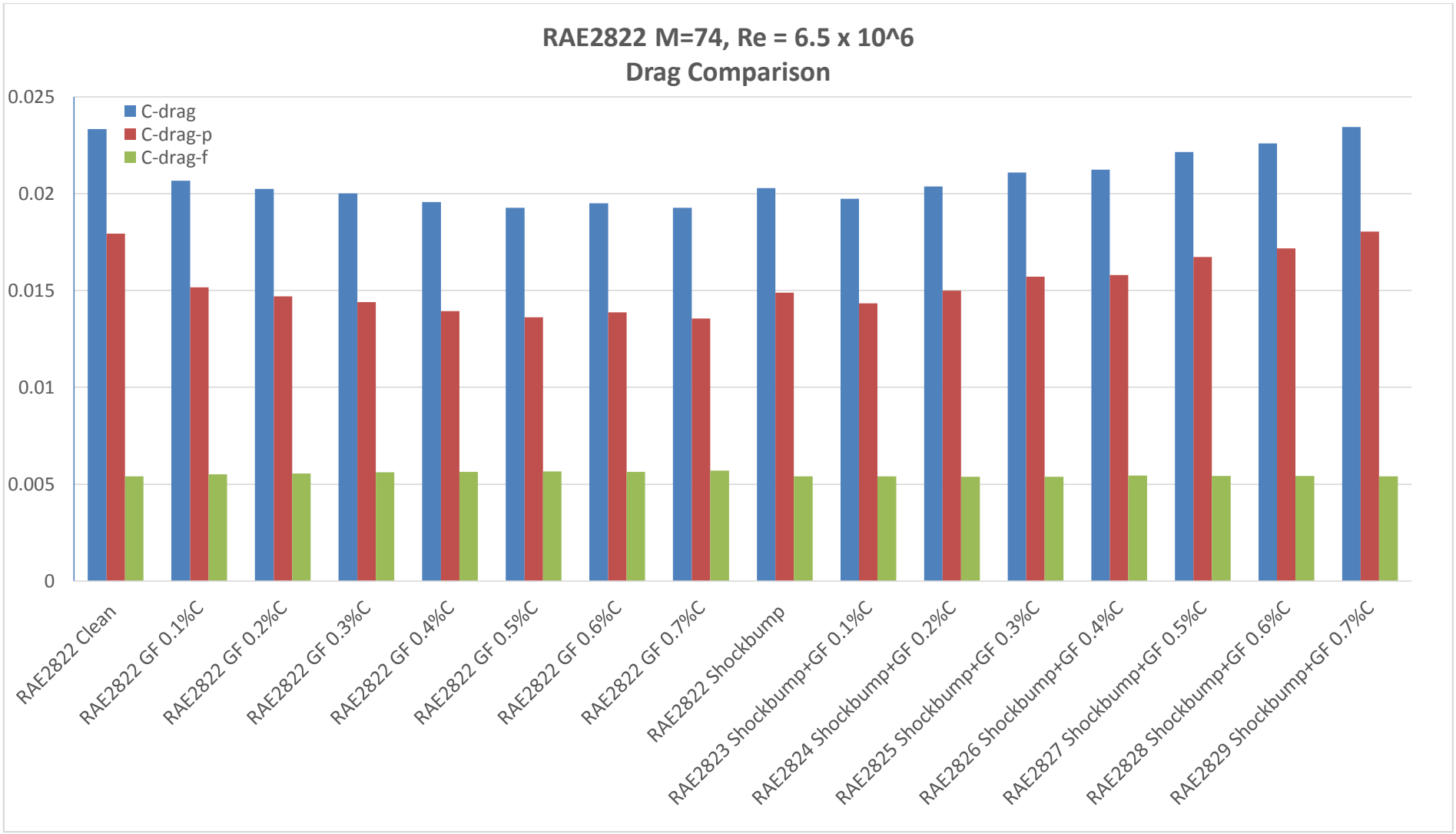

Figure 4.2.4.3c Drag component breakdown c) @M = 0.74

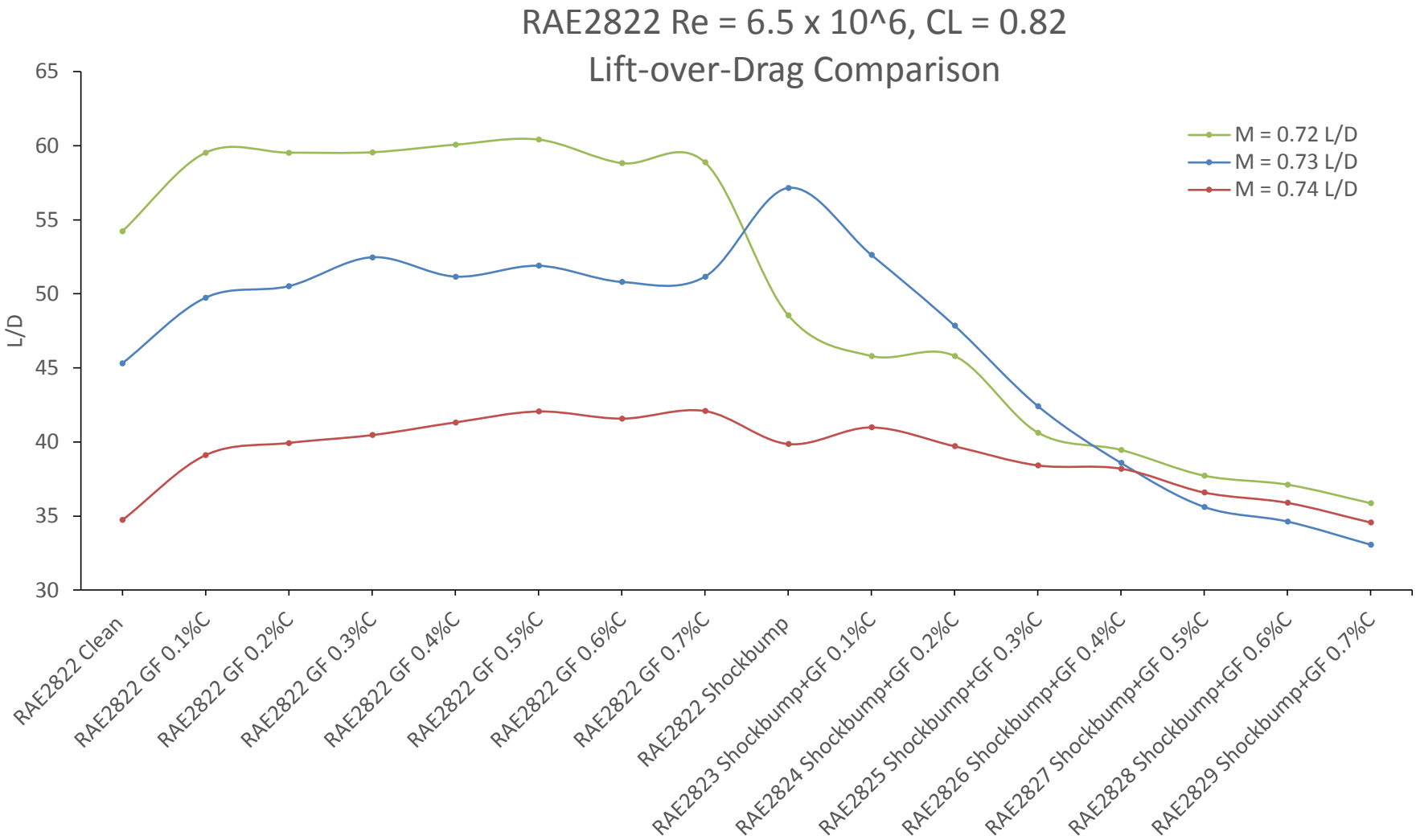

Figure 4.2.4.4 Lift-over-drag Comparison

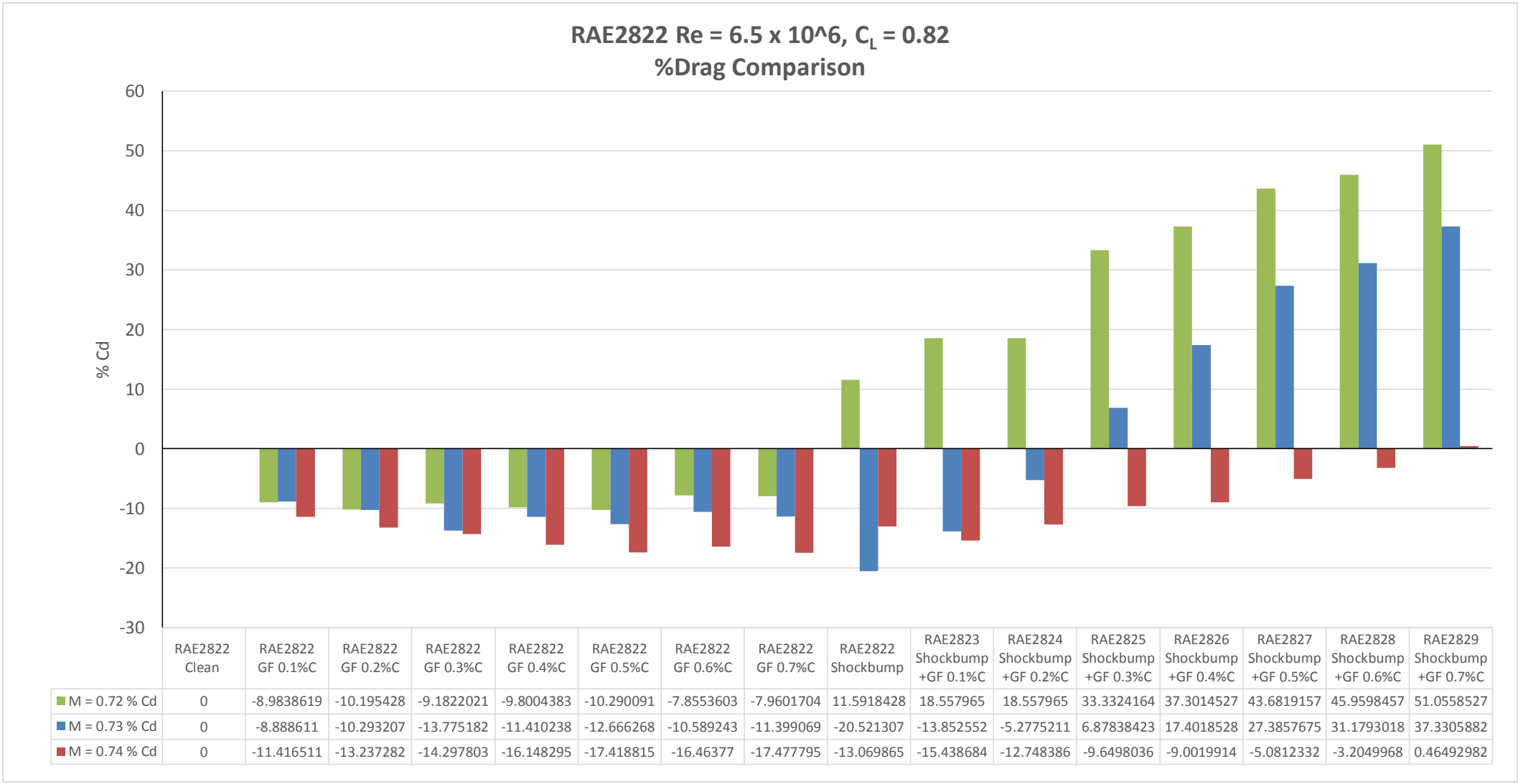

	RAE2822 Clean	RAE2822 GF 0.1%C	RAE2822 GF 0.2%C	RAE2822 GF 0.3%C	RAE2822 GF 0.4%C	RAE2822 GF 0.5%C	RAE2822 GF 0.6%C	RAE2822 GF 0.7%C	RAE2822 Shockbump	RAE2823 Shockbump +GF 0.1%C	RAE2824 Shockbump +GF 0.2%C	RAE2825 Shockbump +GF 0.3%C	RAE2826 Shockbump +GF 0.4%C	RAE2827 Shockbump +GF 0.5%C	RAE2828 Shockbump +GF 0.6%C	RAE2829 Shockbump +GF 0.7%C
M = 0.72 % Cd	0	-8.9838619	-10.195428	-9.1822021	-9.8004383	-10.290091	-7.8553603	-7.9601704	11.5918428	18.557965	18.557965	33.3324164	37.3014527	43.6819157	45.9598457	51.0558527
M = 0.73 % Cd	0	-8.888611	-10.293207	-13.775182	-11.410238	-12.666268	-10.589243	-11.399069	-20.521307	-13.852552	-5.2775211	6.87838423	17.4018528	27.3857675	31.1793018	37.3305882
M = 0.74 % Cd	0	-11.416511	-13.237282	-14.297803	-16.148295	-17.418815	-16.46377	-17.477795	-13.069865	-15.438684	-12.748386	-9.6498036	-9.0019914	-5.0812332	-3.2049968	0.46492982

Figure 4.2.4.5 Percentage Drag Compariso

4.3 Natural Laminar Flow Aerofoil and Shockbump (Validation)

The RAE5243 NLF aerofoil was selected for this study, as shock control is more crucial for such wings due to the requirement of favourable pressure gradients on a substantial part of the wing. This is because NLF aerofoil generate stronger shock waves then supercritical aerofoil, due to the requirement of favourable pressure gradients on a substantial portion of the wing. This means any form of shock control can be display more easily. And also no previous work can be found on the effects of Gurney flap on Natural Laminar Flow (NLF) transonic aerofoils.

The basic principles of shock control method are either to increase the energy of the boundary layer flow just before the interaction region, and alternatively obtain a compression of the flow immediately before the shock wave via local geometrical modification. The latter method, shock bump, was looked at in this scenario. The function of shock bump is to weaken the shock strength during transonic flight, thus reduces drag. The optimised contour bump geometry discussed in this report was designed by Qin, N., Wong W. S. and A Le Moigne[35],a 2 equation k-ω turbulence model was used in their study.

Both baseline aerofoil and optimised contour bump 2D geometry consist of 3 point source (leading edge, trailing edge and overall growing) and 2 line source (aerofoil and wake region). The spacing for all sources are then varied with the same factor, 10 different size meshes were generated for each geometry and used in the verification process. The solver was set to Upwind Backward Euler scheme. There were 2 simulation conducted for each mesh, this is to observe the different results for 1 equation turbulence model and 2 equation turbulence model. The Spalart-Allmars model (1 equation) and k-ω Linearized Explicit Algebraic Stress Model (2 equation). The flow condition is set at 0% transition, fully turbulence. The first cell height is set at 6.78×10^{-7}, this is to achieve $y+ \approx 1$ as required for the

best result by the turbulence model. And the convergence criteria is set at $1x10^7$. The k-ω 2 equation turbulence model was also selected for validation of purposes against reference data[35][37].

The RAE5243 aerofoil was initially tested at $\alpha = 0.77^o$, with M = 0.68 and Re = $1.9x10^7$, in order to compared with [36]Fulk and Simmons' wind tunnel experimental data. A mesh independent analysis was also carried out to verify to consistency of the outputting result. Figure 4.3.0 displays the surface pressure distribution comparison from the experimental data and present simulation via Tau flow solver. The two data displayed a very good match. A favourable pressure distribution on the suction surface is clearly shown, then followed by a relatively strong normal shock wave. Thus, M = 0.68 and Re = $1.9x10^7$ with $C_L = 0.82$ was used as the benchmark or reference condition

The optimised contour bump geometry in this study is obtained from Qin et al(2008) [35]. The shockbump is optimised for M = 0.68, $Re_c = 19 \times 10^6$, and $C_L = 0.82$. Figure 2.2 shows the geometry detail of the shockbump. The simulation result were then compared with reference data, Qin et al[35] and Lee et al[37].

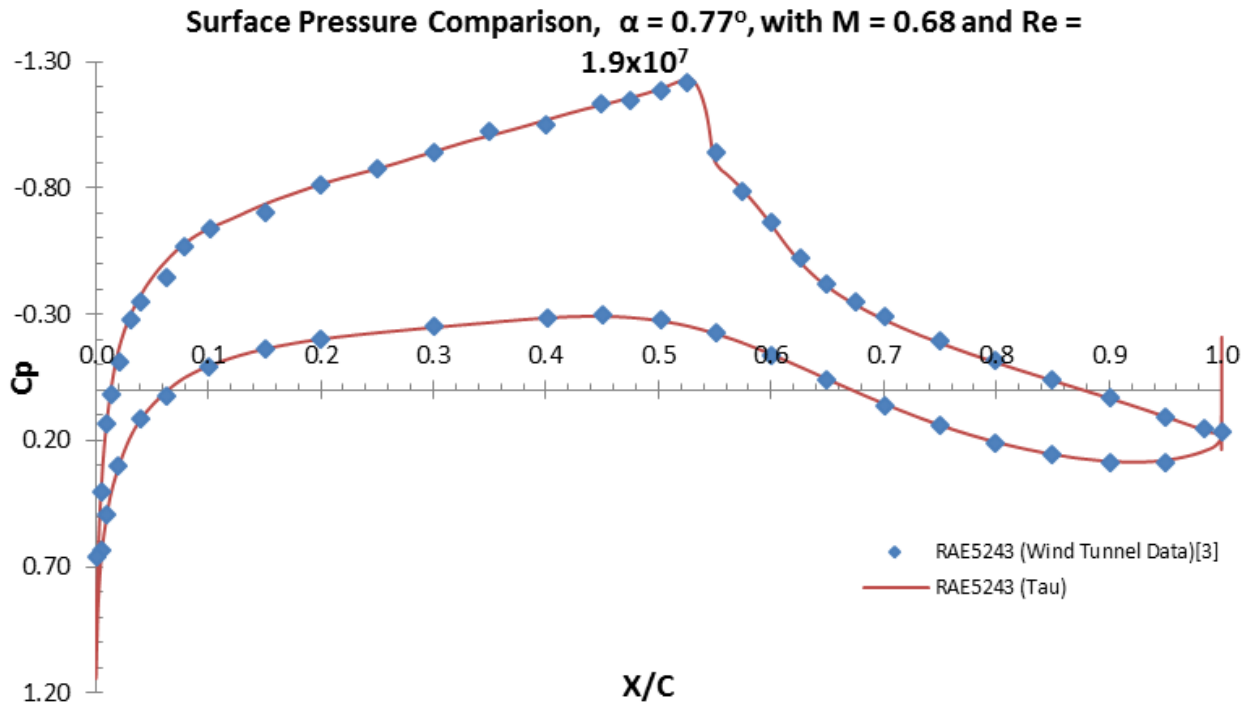

Figure 4.3.0 **Surface pressure distribution on the REA5243 aerofoil**

The contour bump geometry;

Length (%)	31.3
Crest (%)	59.7
Relative (%)	66.1
Height (%)	0.59

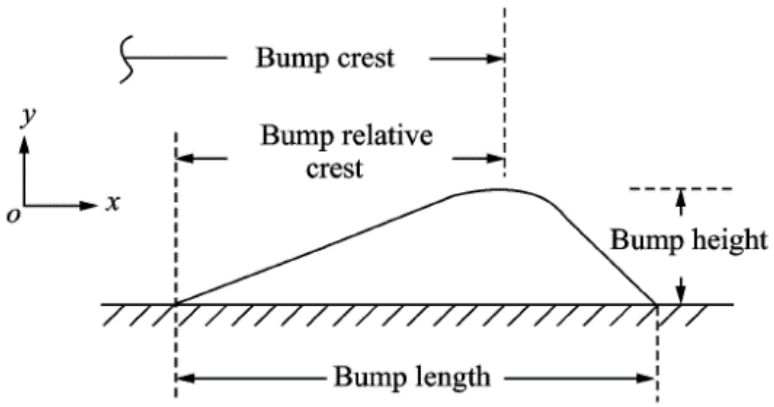

Figure 4.3.1 Parameterization of 2D bumps

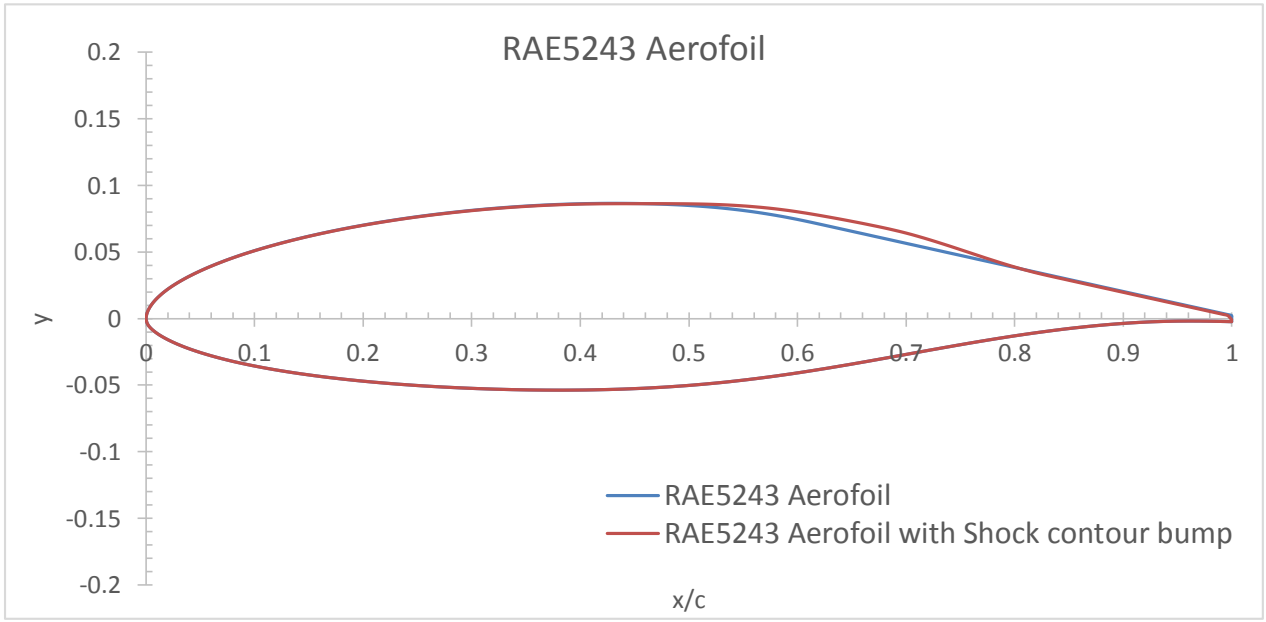

Figure 4.3.2 Geometry: Shock bump and clean aerofoil

Test Condition

Reference temperature: 273.15K

Reference Mach number: 0.68

Reynolds number: 19×10^6

Reynolds length: 1

Angle of attack: allocated from the solver

Constraint: $C_L = 0.82$

From the mesh independent study, the drag coefficient for RAE5243 clean aerofoil configuration with k-ω Linearized Explicit Algebraic Stress Model (Table 4.3.1), C_D = 0.01444, and with Spalart-Allmars Model (Table 3.3.2), C_D = 0.01364. And for the RAE5243 with optimised contour bump with k-ω Linearized Explicit Algebraic Stress Model (Table 4.3.3), C_D = 0.01089, and with Spalart-Allmars Model (Table 4.3.4), C_D = 0.01070.

Table 4.3.1 Mesh Independent data: k-ω Linearized Explicit Algebraic Stress Model

Spacing	Surface Elements	C_L	C_D	Residual	Iteration	Max y+	1st Cell Height	alpha
20%	3,102,694	0.8192	0.0144	4.4622E-03	200,000	1.0225	6.7800E-07	2.4335
25%	1,991,872	0.8201	0.0141	2.8690E-03	200,000	1.0229	6.7800E-07	2.4401
30%	1,370,534	0.8196	0.0143	3.2904E-06	100,000	1.0247	6.7800E-07	2.5214
40%	814,214	0.8201	0.0143	9.9861E-07	31,910	1.0252	6.7800E-07	2.5076
50%	532,831	0.8198	0.0143	9.9903E-07	25,094	1.0253	6.7800E-07	2.5174
75%	255,702	0.8198	0.0144	9.9437E-07	16,407	1.0259	6.7800E-07	2.5270
100%	153,405	0.8196	0.0146	1.0000E-06	16,100	1.0244	6.7800E-07	2.5468
150%	93,077	0.8191	0.0157	6.7633E-02	100,000	1.2354	6.7800E-07	2.5574
200%	54,182	0.8194	0.0168	6.4672E-02	200,000	1.3157	6.7800E-07	2.5938
400%	20,344	0.8191	0.0197	1.0045E-05	200,000	2.1700	6.7800E-07	2.7667

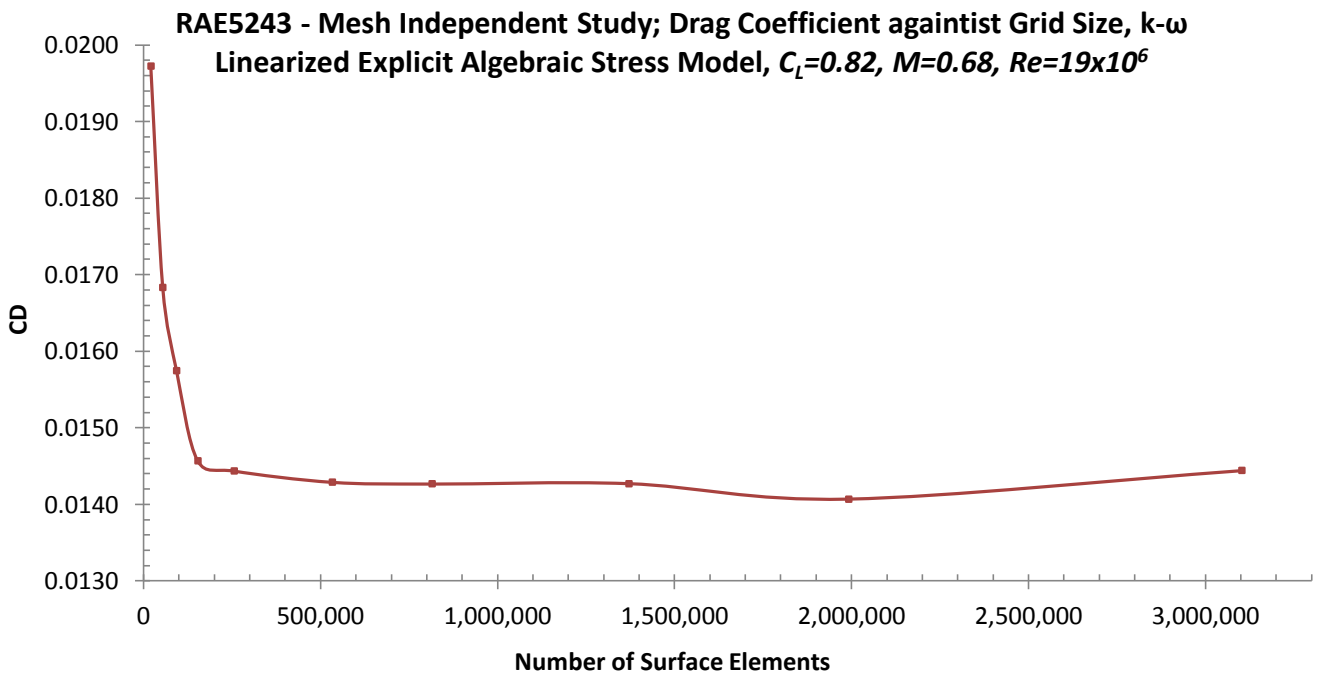

Figure 4.3.3 RAE5243: Drag coefficient against number of surface elements, k-ω Linearized Explicit Algebraic Stress Model

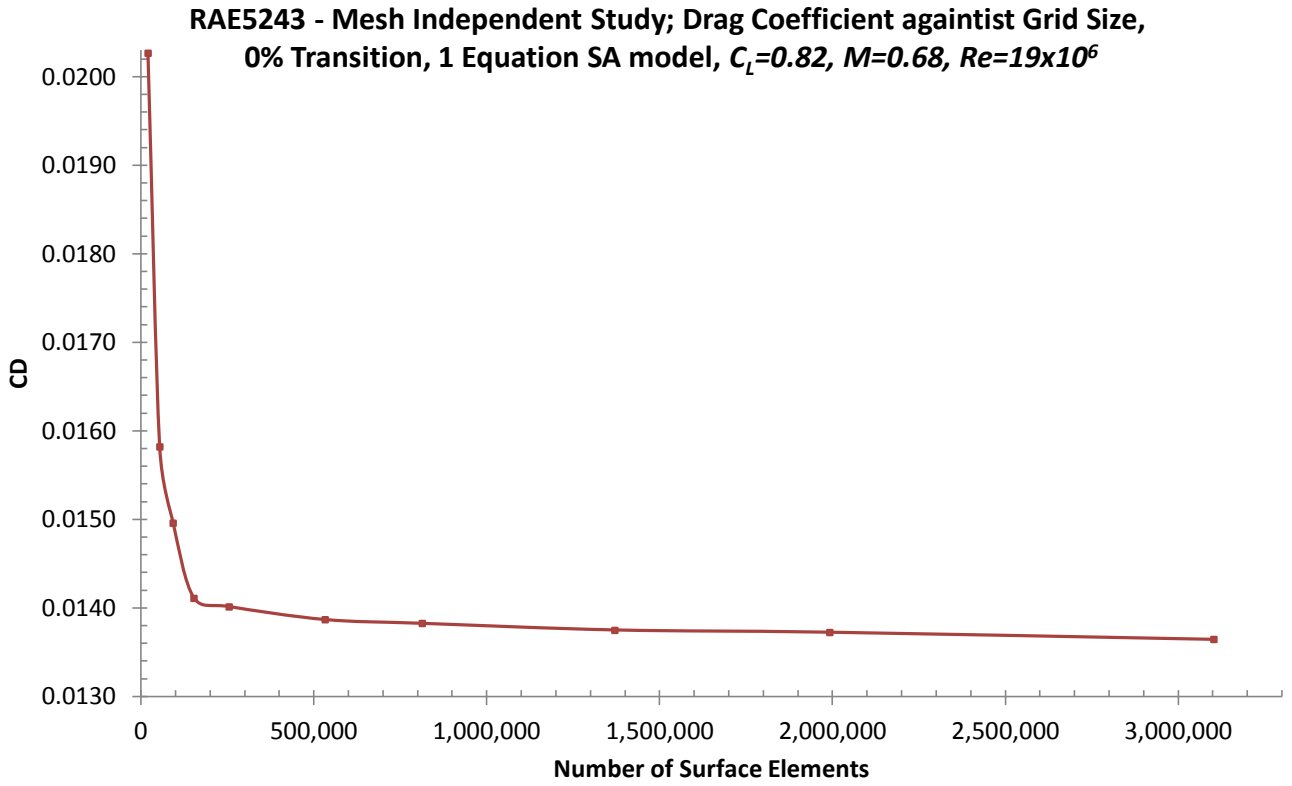

Figure 4.3.4 **RAE5243 aerofoil: Drag coefficient against number of surface elements, S-A Model**

Table 4.3.3 Mesh Independent data (Shockbump): k-ω Linearized Explicit Algebraic Stress Model

Spacing	Surface Elements	C_L	C_D	Residual	Iteration	Max y+	1st Cell Height	alpha
17.8%	3,616,026	0.8201	0.0109	9.9906E-07	77,759	1.0206	6.7800E-07	2.2966
20.5%	2,899,497	0.8200	0.0109	9.9769E-07	58,798	1.0208	6.7800E-07	2.2984
30%	1,374,740	0.8198	0.0111	4.3385E-02	200,000	1.0430	6.7800E-07	2.3435
40%	817,673	0.8201	0.0110	9.9810E-07	31,584	1.0205	6.7800E-07	2.2850
50%	535,952	0.8202	0.0111	9.9751E-07	23,085	1.0207	6.7800E-07	2.2903
75%	254,130	0.8191	0.0112	1.8372E-02	200,000	1.0223	6.7800E-07	2.3286
100%	153,302	0.8191	0.0115	9.9393E-07	18,394	1.0195	6.7800E-07	2.2961
150%	90,977	0.8192	0.0121	9.9868E-07	17,749	1.0076	6.7800E-07	2.3502
200%	52,802	0.8191	0.0133	9.8361E-07	16,748	0.9680	6.7800E-07	2.3816
400%	20,334	0.8190	0.0196	1.1854E-01	200,000	1.3138	6.7800E-07	2.8064

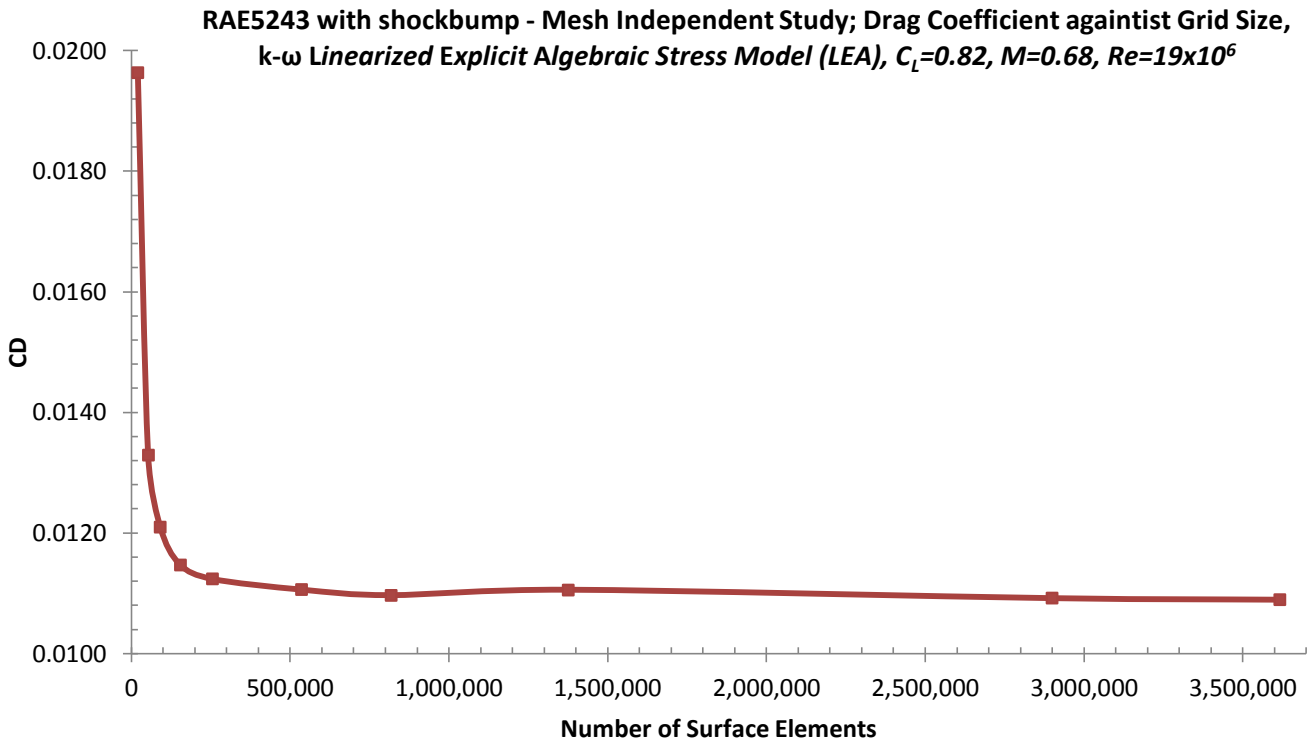

Figure 4.3.5 RAE5243 with Shock contour bump: Drag coefficient against number of surface elements, k-ω Linearized Explicit Algebraic Stress Model

Table 4.3.4 Mesh Independent data (Shockbump): S-A Model

Spacing	Surface Elements	C_L	C_D	Residual	Iteration	Max y+	1st Cell Height	alpha
17.8%	3,616,026	0.8200	0.0107	9.9855E-07	51,813	0.9836	6.7800E-07	2.3598
20.5%	2,899,497	0.8199	0.0107	9.9925E-07	45,609	0.9840	6.7800E-07	2.3700
30%	1,374,740	0.8200	0.0110	1.1311E-02	100,000	1.0013	6.7800E-07	2.4562
40%	817,673	0.8202	0.0109	9.9567E-07	22,059	0.9839	6.7800E-07	2.3786
50%	535,952	0.8202	0.0110	9.9882E-07	17,370	0.9838	6.7800E-07	2.4003
75%	254,130	0.8191	0.0111	4.5800E-03	100,000	0.9841	6.7800E-07	2.4251
100%	153,302	0.8191	0.0115	9.8966E-07	12,786	0.9807	6.7800E-07	2.4695
150%	90,977	0.8190	0.0123	9.8770E-07	13,006	0.9735	6.7800E-07	2.5807
200%	52,802	0.8190	0.0136	9.9437E-07	12,743	0.9273	6.7800E-07	2.6121
400%	20,334	0.8190	0.0206	3.1528E-02	200,000	1.2070	6.7800E-07	3.3615

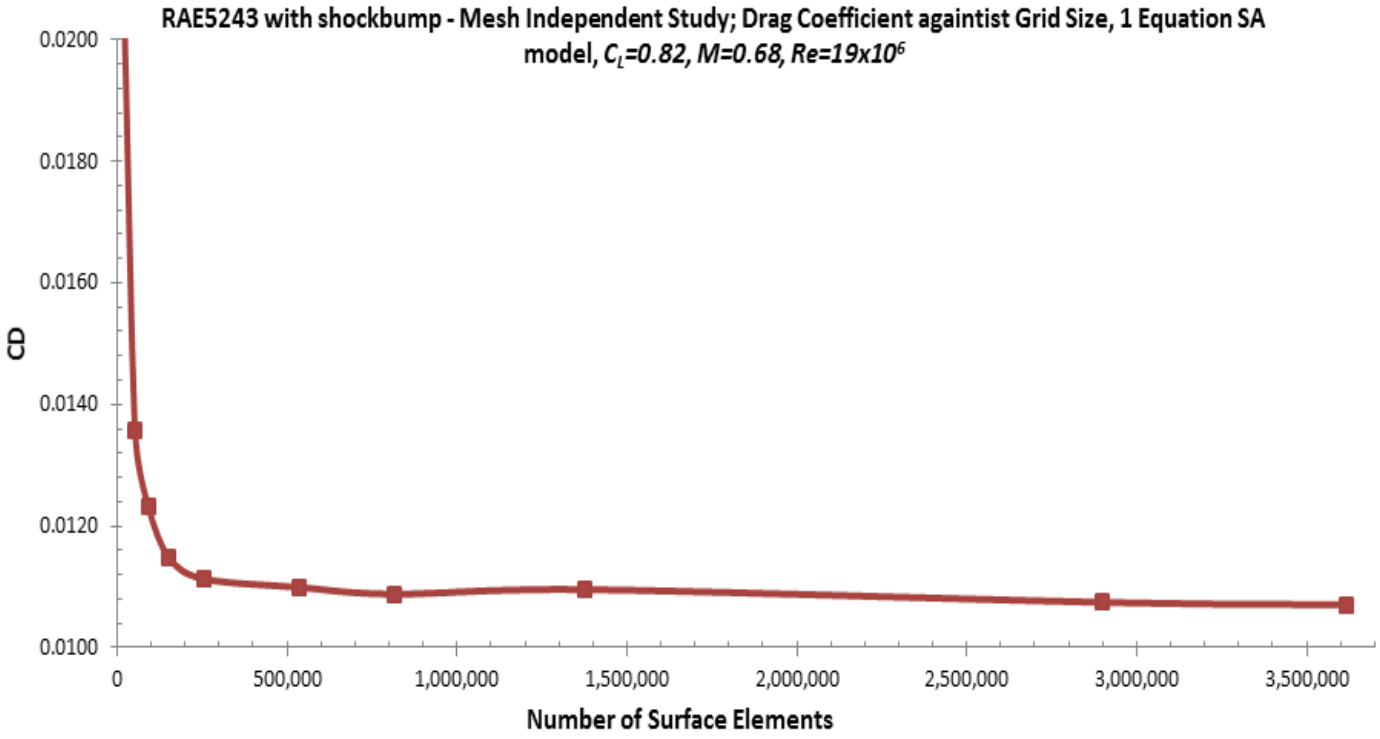

Figure 4.3.6 **RAE5243 with Shock contour bump: Drag coefficient against number of surface elements, S-A**

The simulation result were then compared with reference data[35][37].

For the numerical analysis, it displayed a 21.5% reduction in drag with S-A turbulence model and 24.5% reduction in drag with LEA turbulence model. The discrepancy of the drag changing is solely due to the turbulence model selected, each turbulence model will model the flow behaviour differently. It is a good practice and essential to determine the best model for a specific problem. However, this task is not complete and will require further work in gaining a full understanding of different models. From reference data, [35]Qin showed a 18.2% decrease in drag. Nevertheless, the pressure distribution obtained from Tau solver shows a similarity to the Merlin (flow solver used by [35]Qin). A reduction/ weaken shock can be seen from the distribution plot. Figure 4.3.0.

The maximum Mach number occurred in the clean aerofoil RAE5243 is M = 1.30646 (via LEA model) and M = 1.30946 (via SA model). Whereas, the maximum Mach number displayed with the shock bump has substantially reduce to M = 1.20125 (via LEA model) and M = 1.2029 (via SA model). Although, by comparison of the two turbulence models, the maximum Mach number and the drag component are different, but the pressure plot shows a very good correlation between the two, Figure 4.3.13. The C_p plot also provides a very good match to the reference data for the clean aerofoil configuration. However, a different trend is displayed for the shock contour bump configuration, it highlight a discrepancy between the results from Tau and Merlin. In reference data for optimised bump, a reduced peak pressure are described followed by a slight pressure drop, and then a straight down pressure drop, which representing the shock. Nonetheless, the results obtained for this section demonstrate similar changing peaks in the graph but the pressure drop is more gradual. The reason for the discrepancy had not been yet investigated. It will be a very interesting to understand why the flow has been predicted in such way and from then the author will gain further valuable knowledge in the solver operation and behaviour.

Table 4.3.5 Comparison Results

Geometry	Method	Alpha	C_L	C_D	ΔC_D (%)	Shock location	Cp at shock	L/D
RAE5243 Clean	**Reference data** k-ω, Merlin (Qin)[35]	-	0.82	0.01622	-	0.55	-	50.55
RAE5243 Clean	**Reference data** HAPMOEA (Lee)[37]	2.54	0.82	0.01359	-	-	-	60.34
RAE5243 Clean	k-ω LEA model, Tau solver	2.43	0.8192	0.01444	-	0.54	-1.5960	56.73
RAE5243 Clean	S-A model, Tau solver	2.54	0.8198	0.01364	-	0.54	-1.6076	60.08

Geometry	Method	Alpha	C_L	C_D	ΔC_D (%)	Shock location	Cp at shock	L/D
RAE5243 - Optimised bump	**Reference data** k-ω, Merlin (Qin)[35]	-	0.82	0.01326	18.25%	0.57	-	61.84
RAE5243 - Optimised bump	**Reference data**, HAPMOEA (Lee)[37]	2.46	0.82	0.01120	17.59%	-	-	73.21
RAE5243 - Optimised bump	k-ω LEA model, Tau solver	2.29	0.8201	0.01089	24.56%	0.53	-1.3210	75.28
RAE5243 - Optimised bump	S-A model, Tau solver	2.36	0.8200	0.01070	21.55%	0.53	-1.3150	76.60

The Mach number plot in Figure 4.3.7 and Figure 4.3.10 shows the weakening of the shock with the aid of a contour bump in both turbulence models. The pressure contours in Figure 4.3.8, 4.3.9, 4.3.11 and 4.3.12 illustrate the smearing effects of the bump on the original normal shockwave, reducing the shock strength and spreading it into more gradual compression waves. It also indicates the presents of continuous supersonic compression which can be seen by the 'collapsing down' contour lines above the bump, and accompanied by an immediate continuous subsonic expansion. This behaviour can also be found in the C_p plot, Figure 4.3.13, for both turbulence models.

From table 4.3.15, Tau solution displayed a 24.56% and 21.55% reduction in drag by using LEA turbulence model and SA turbulence model, respectively. But on the other hand, Qin et al. and the Lee et al.'s HAPMOEA validation study only predicted an 18.25% and 17.59% drag reduction, respectively. The drag coefficient obtained from this simulation does not directly match with previous studies. This is due to different solver and turbulence model used. Hence, resulting different values predicted in drag determination. However, the drag reduction correlation is very similar.

The 2 equation model used was an attempt to directly replicate Qin et al. and Lee et al.'s results, but it was unsuccessful. The SA turbulence produced a closer results than then LEA model. This finding encouraged the study to continue applying SA equations as the solver's turbulence model throughout the NLF investigation.

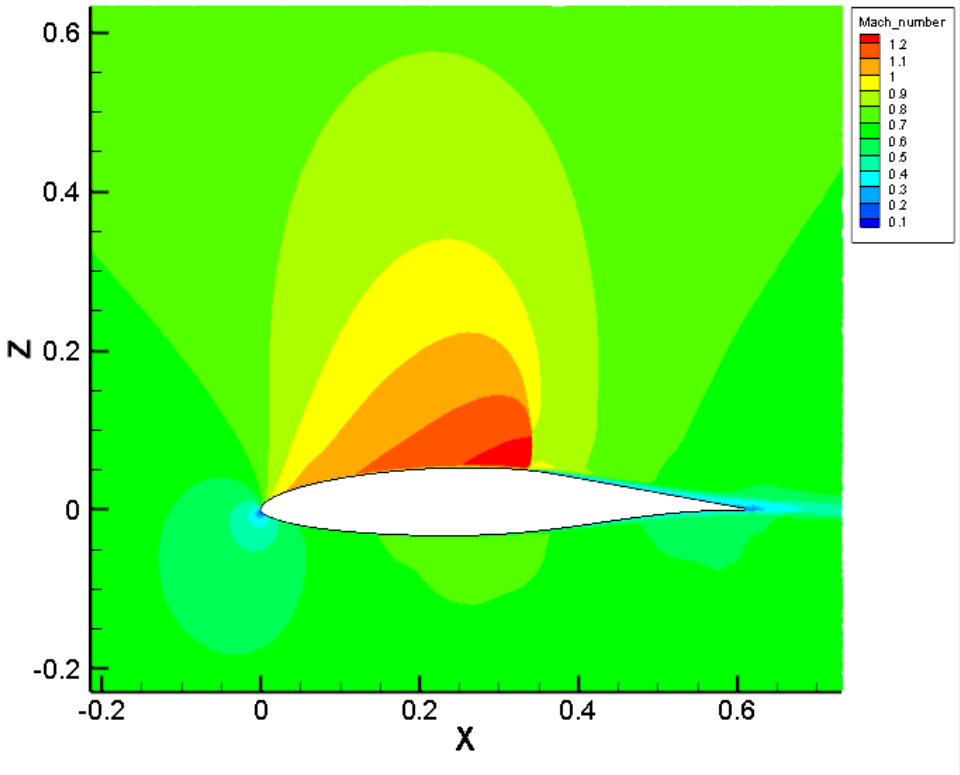

Figure 4.3.7a **Mach number contour plot, LEA Model; (a) clean aerofoil (datum)**

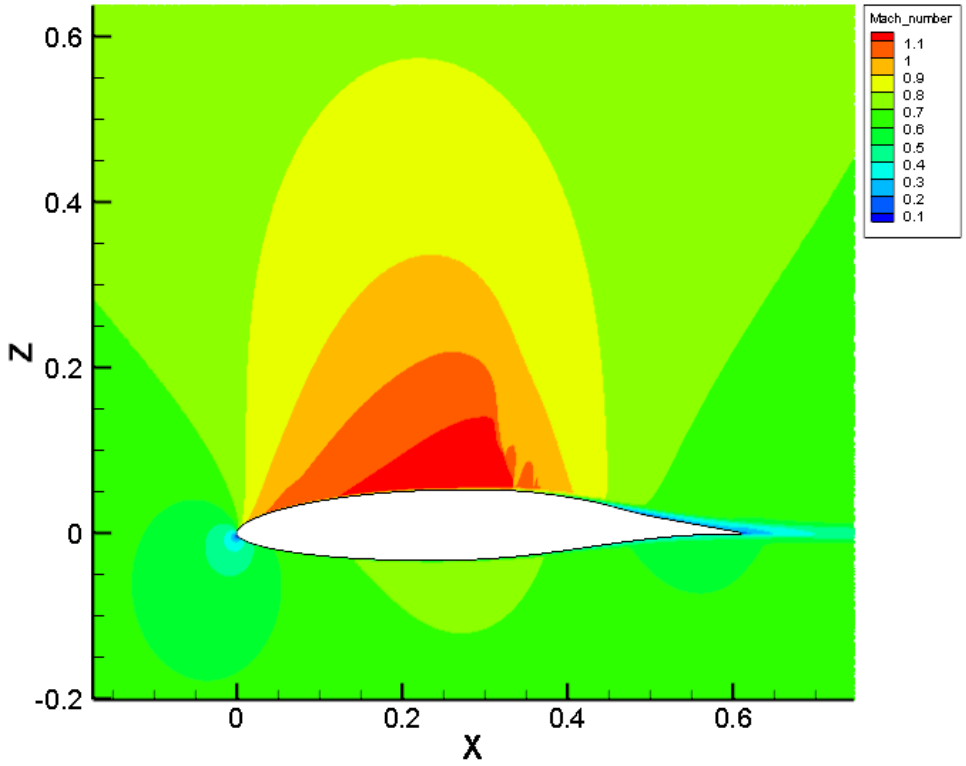

Figure 4.3.7b **Mach number contour plot, LEA Model; (b) with optimised bump**

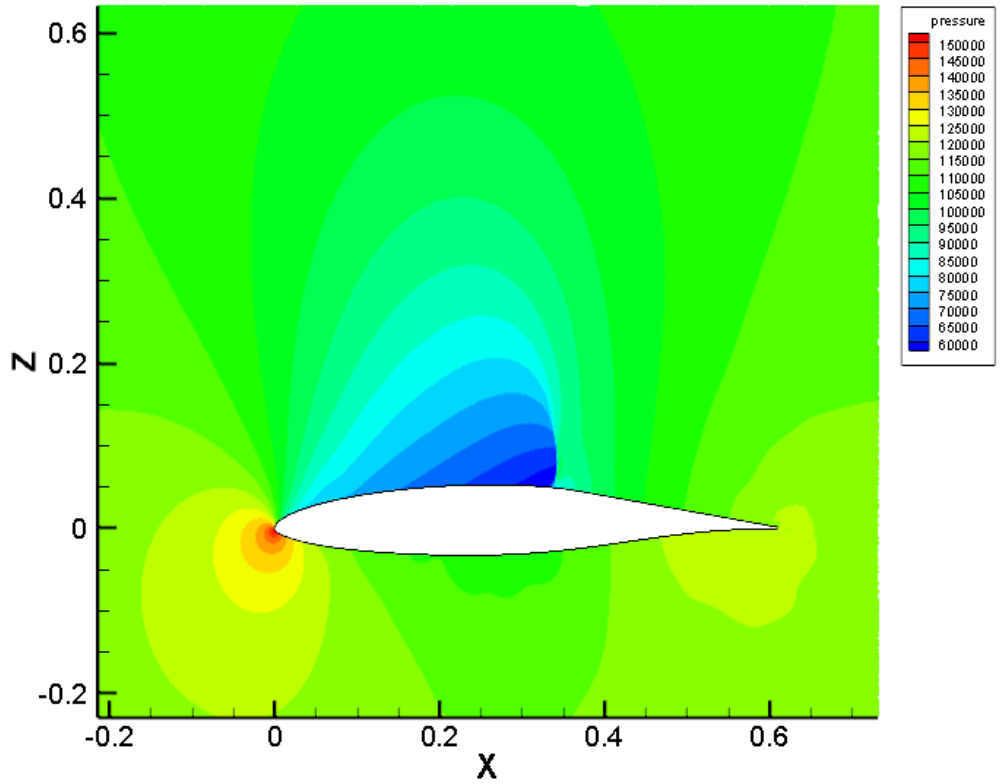

Figure 4.3.8a **Datum aerofoil; Pressure Contour plots (a) overview of the aerofoil , LEA Model**

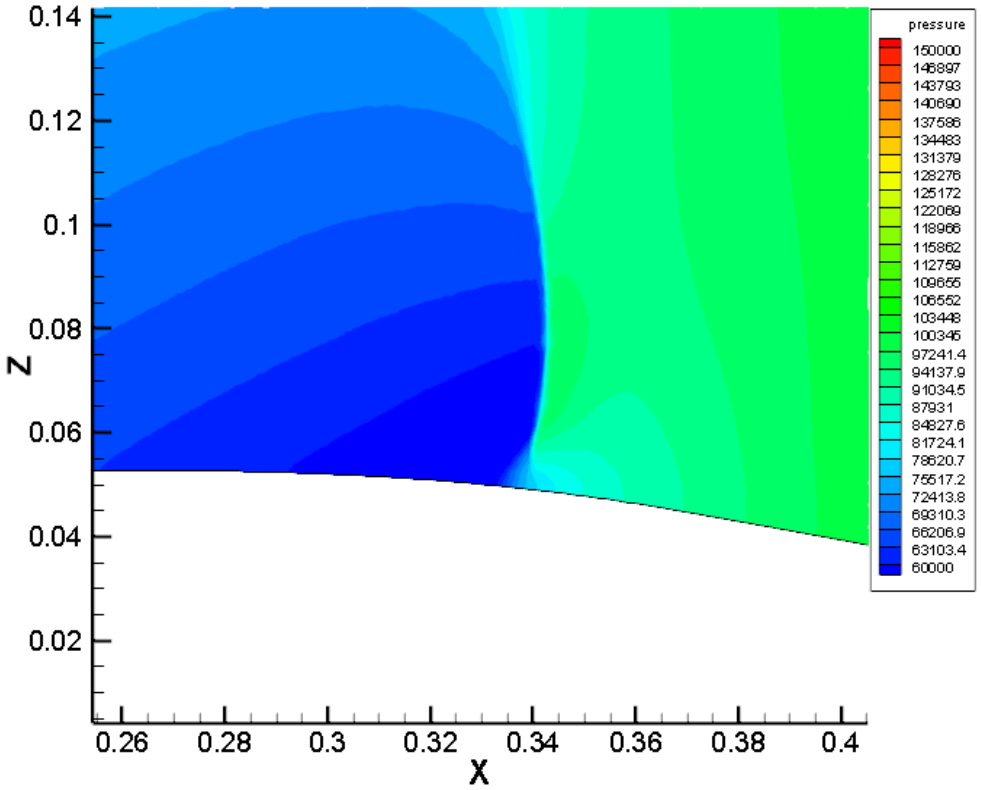

Figure 4.3.8b **Datum aerofoil; Pressure Contour plots (b) at the shock location, LEA Model**

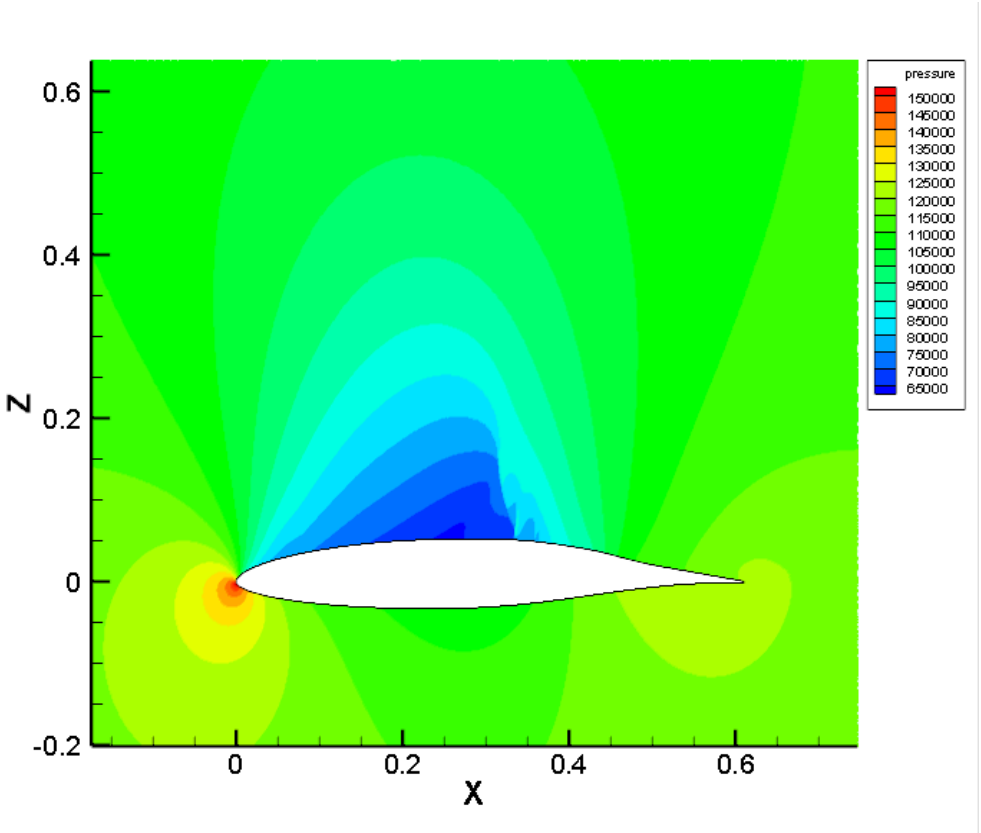

Figure 4.3.9a **With Optimised bump; Pressure Contour plots (a) overview of the aerofoil, LEA Model**

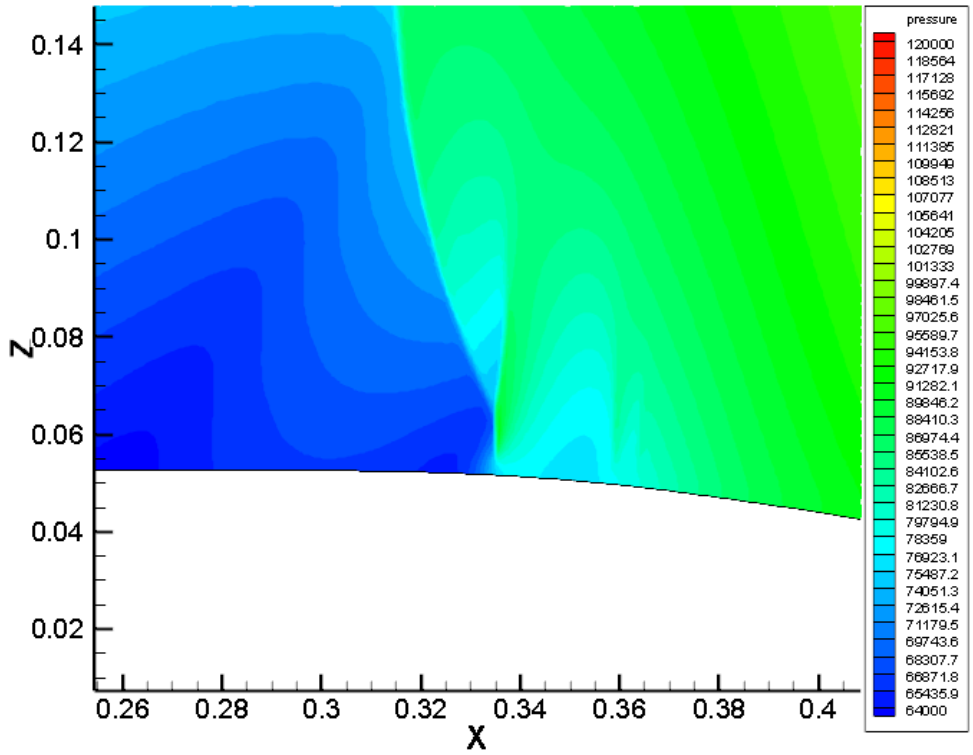

Figure 4.3.9 **With Optimised bump; Pressure Contour plots (b) at the shock location, LEA Model**

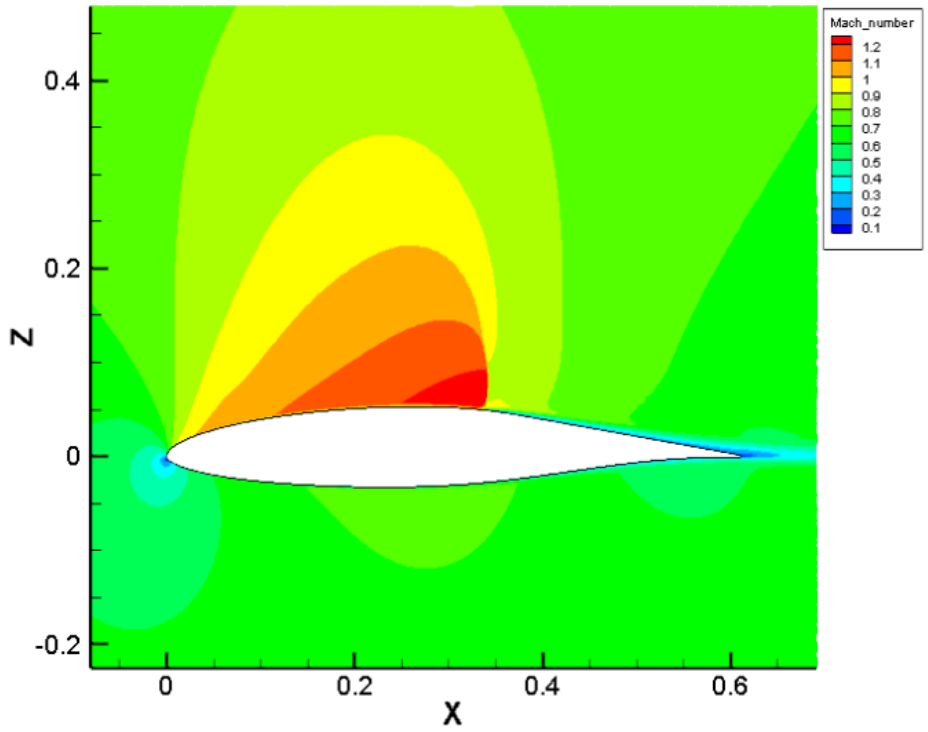

Figure 4.3.10a **Mach number contour plot, SA Model; (a) Datum aerofoil**

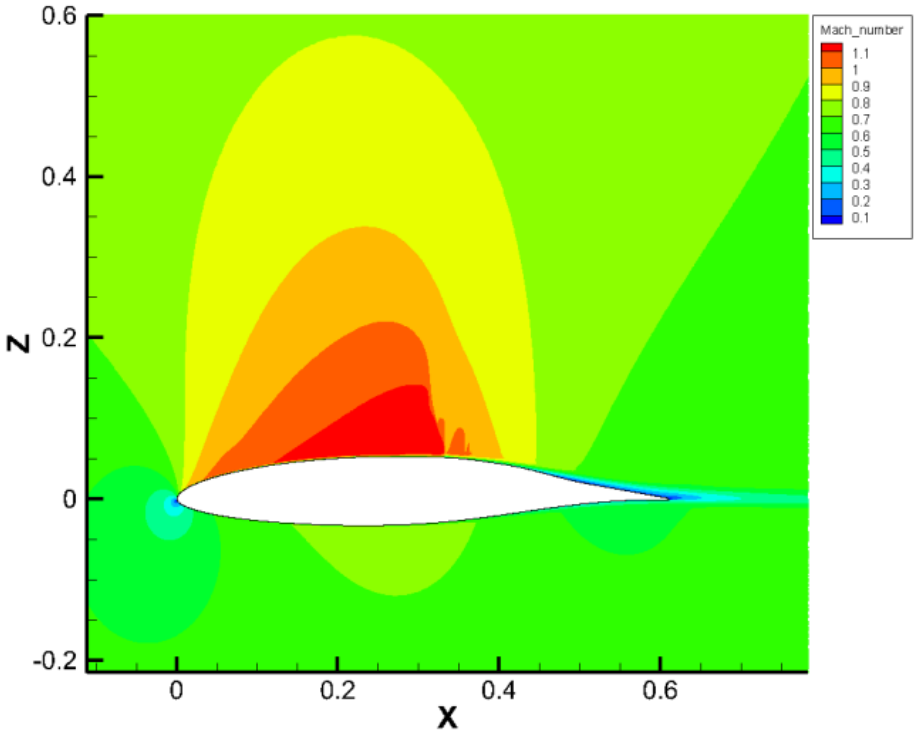

Figure 4.3.10b **Mach number contour plot, SA Model; (b) with optimised bump**

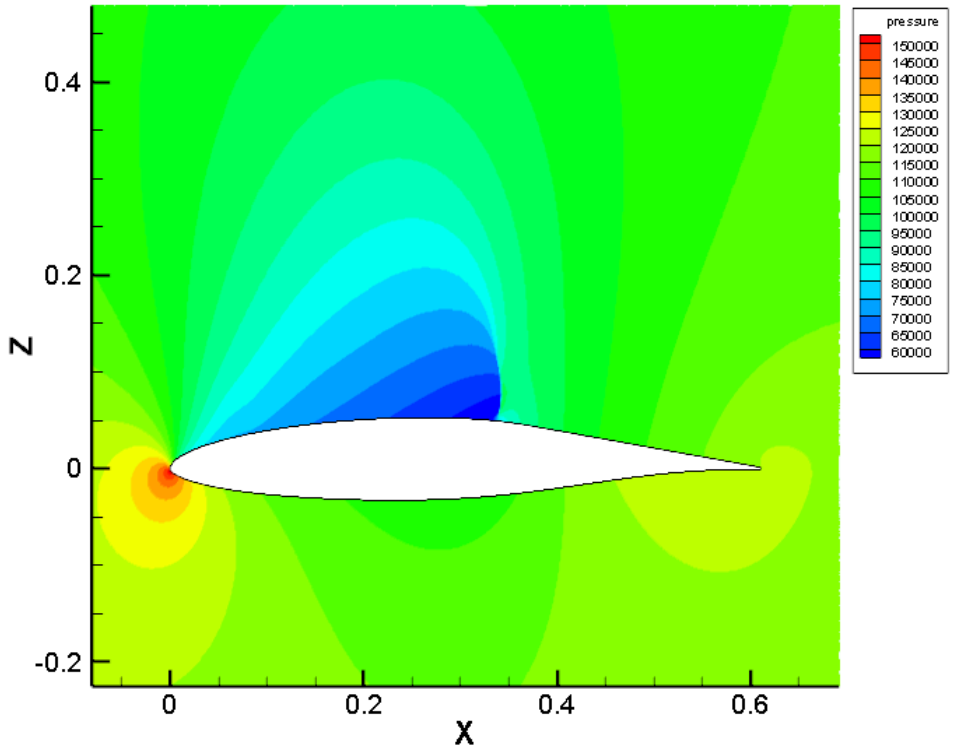

Figure 4.3.11a **Datum aerofoil; Pressure Contour plots (a) overview of the aerofoil, SA Model**

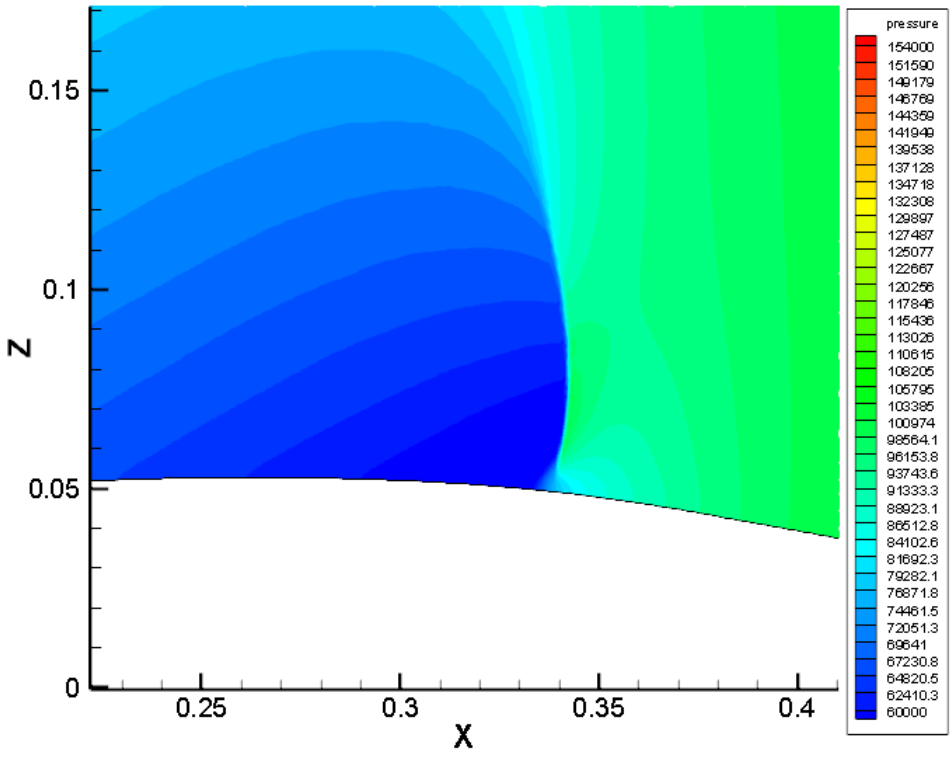

Figure 4.3.11b **Datum aerofoil; Pressure Contour plots (b) at the shock location, SA Model**

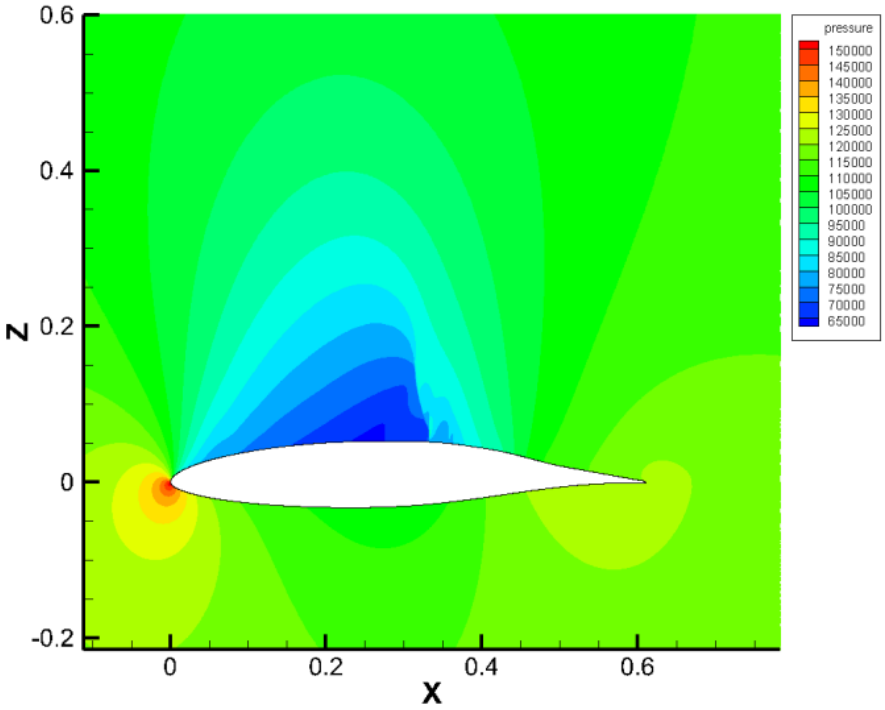

Figure 4.3.12a **With Optimised bump; Pressure Contour plots (a) overview of the aerofoil, SA Model**

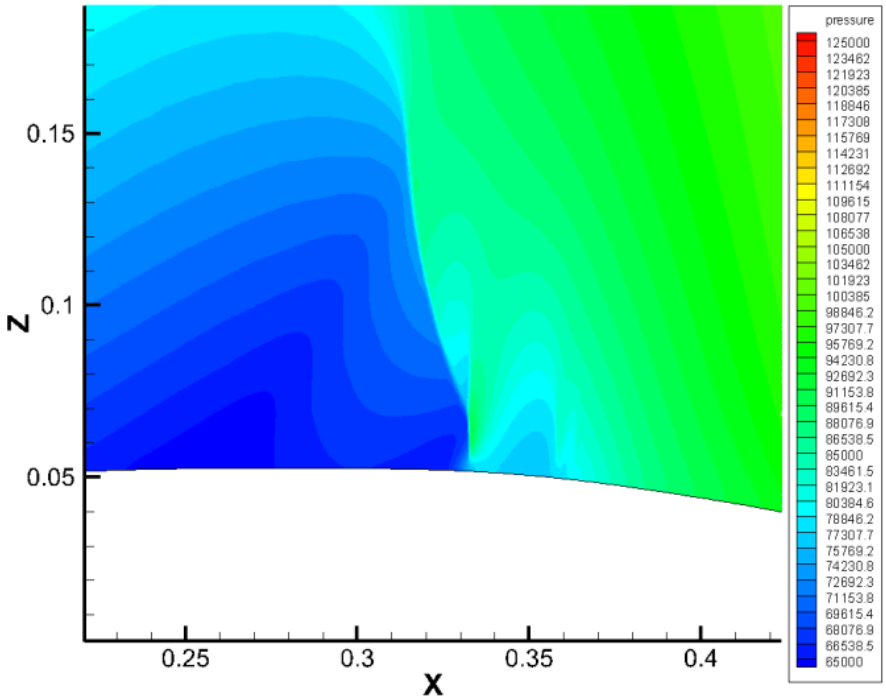

Figure 4.3.12b **With Optimised bump; Pressure Contour plots (b) at the shock location, SA Model**

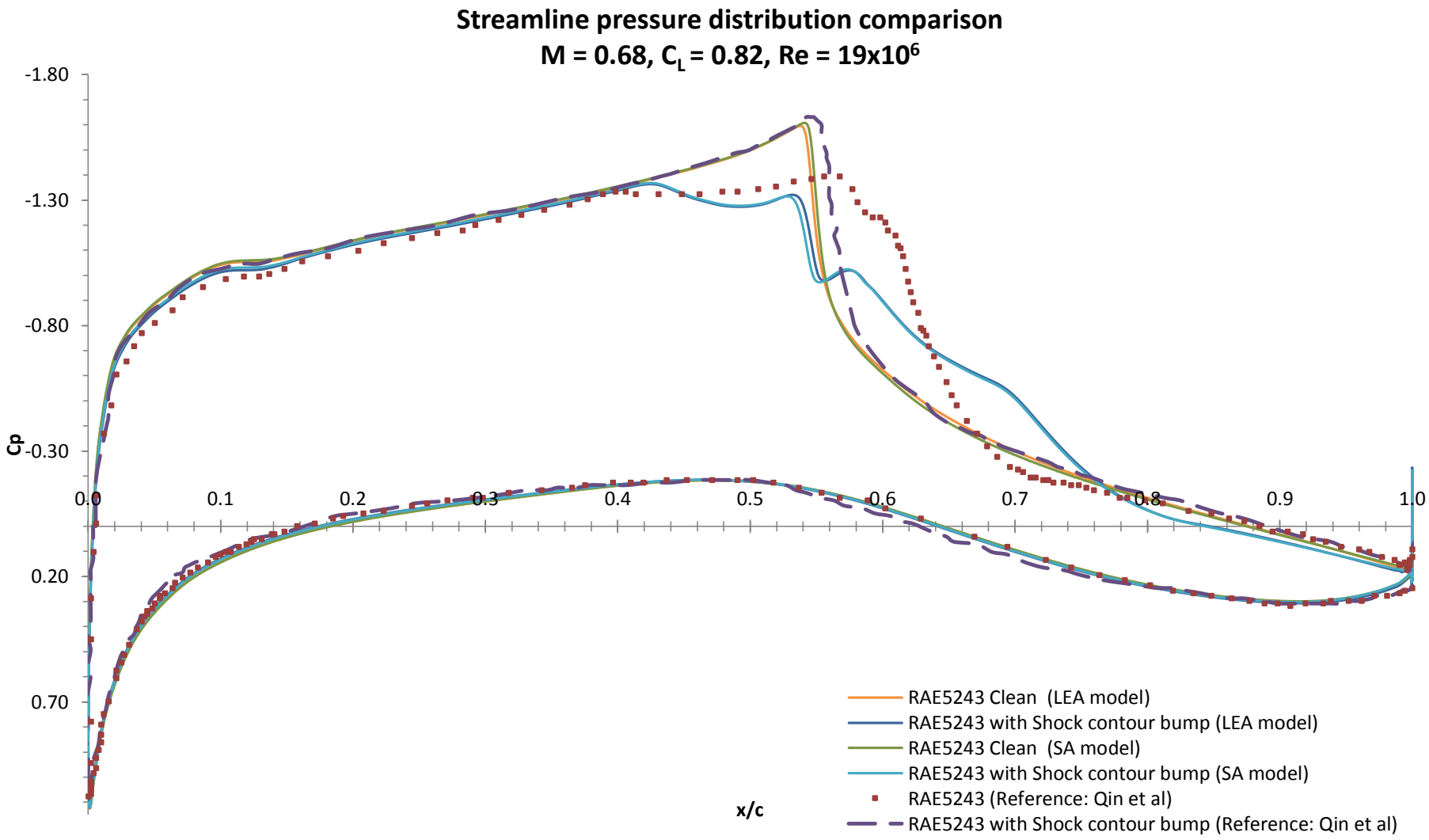

Figure 4.3.13 **Streamwise pressure distribution**

4.4 Natural Laminar Flow Aerofoil with Shockbump and Gurney Flap

NLF aerofoils are gaining popularity with aircraft manufacturer. However, it is very sensitive to shock at transonic conditions. For NLF aerofoil to be useful, shock strength needs to be controlled. In the current study, the shock control feature of Gurney flap was investigated with NLF aerofoils. This is because of the shock sensitive characteristic of NLF aerofoil, which means any effects to the shock can be more visible. Wong et al. (2008)[38] and Qin et al. (2008)[35] looked at the effects of shock control devices such as shock bump and ramp are extensively. Their results concluded, shock bump can achieve a beneficial amount of drag reduction through lowering the wave drag, and weakening the foot of the shock by continuous compression.

Shock bump can be optimised for a specific cruise condition but it is difficult to make it robust for a range of flight conditions. Also, a variable geometric shock bump still faced a large structural and manufacturing constrain with current technology. On the other hand, Gurney flap would be cheaper to install as a retrofit adaptive device then a shock bump. The combination of Gurney flap and shock bump may lead to further reduction in drag; as both devices has its own feature in altering shock behaviour. By integrating the variable Gurney flap and shock bump together, this may result into a more efficient and robust shock bump, which can derive benefit at a range of flight conditions.

This Natural Laminar Flow aerofoil with GF and shockbump was investigated through CFD at three different Mach number; M = 0.67, M = 0.68, M = 0.69. The purpose of this range is to investigate the properties of GF in off-designed condition. M = 0.68 is the designed cruise speed. In the lift constraint (C_L = 0.82) scenario for all tested Mach number, the Cp plot (Figure 4.4.1) displayed similar findings to the previous section of Supercritical aerofoil, as the Gurney flap length increases the trailing edge

pressure and suction point increases. This in turn suggestion an increase in rear loading. This can be seen on the plot where trailing's Cp opened. The leading edge / section of the aerofoil reduces suction and shock is delayed downstream can also be seen from the plot.

From the data obtained, figure 4.4.1 suggests that the Gurney Flap addition on both clean and shockbump aerofoil, features shockwave delay downstream. The alteration of effective camber causes steady reduce in suction for the front of the aerofoil. However, the shockwave delayed distance caused is rather short, this means a larger pressure difference will occurred to maintain a given lift, which implies a bigger shockwave. The area under the curve in a C_p plot represent lift. The trailing edge shows an increase of suction and pressure surface, this is represents the vortex created by the GF. Again, GF causes an obstruction to the flow causing two rotating vortex; a clockwise rotational vortex immediately after the trailing, and one anti-clockwise vortex at the front of the GF. The simulation points out that GF poses very little or negligence effects on to the skin friction drag, Figure 4.4.6 identity that the addition of GF to NLF causes drag penalty regardless of the flap length, and features no benefits to aerodynamic characteristics. The findings also shows a higher maximum Mach number occurred on the surface of the NLF aerofoil when equipped with GF, this can be clear shown on figure 4.4.5 (a) , (c).

The shock contour bump used in this study was optimised at a specific condition only, however, the drag reduction benefits can be seen in off designed condition too in both slightly lower and higher Mach number (figure 4.4.5, 4.4.6). This suggests the higher robustness of shock contour bump in NLF than supercritical aerofoil. In figure 4.4.1, the surface pressure distribution plot shows the shockbump featured aerofoil maintains very similar front part of C_p properties (from leading edge to ~0.41 x/c) to clean aerofoil. At designed condition, the shockbump reduces the peak suction point and transfer the rapid pressure difference it into a more gradual change, thus weaken the shockwave and reduces the pressure drag. In M = 0.67, the normal shockwave was shifted forward from ~0.58

x/c to ~0.41 x/c and due to the curvature of the shockbump a secondary shockwave was induced, figure 4.4.5 (b). In the same case, with an additional secondary flow control device, GF, figure 4.4.5 (c) shows both shockwaves are strengthened. However, in the higher Mach number, M = 0.69, the peak suction point is reduced by the smearing constant pressure from ~0.4 x/c to ~0.6 x/c, then followed by the normal shock. Figure 4.4.5, 4.4.6; the combination of GF and pre-optimised shockbump, when compared with the clean aerofoil shows drag increment at M = 0.69, whereas in M = 0.67 and 0.68 drag reduction can be found. The GF addition to existing shockbump provides no extra improvement in aerodynamic performance, but actually reduces the L/D enhancement created by the shockbump.

Figure 4.4.2 shows normal shockwave occurred on the NLF during the reference condition. The pressure contour plot in figure 4.4.3, 4.4.4b illustrate the smearing effects of the bump on the original normal shockwave, reducing or wakening the shock strength and spreading it into more gradual compression waves. It also indicates the presents of continuous supersonic compression which can be seen by the ‘collapsing down’ contour lines above the bump, and accompanied by an immediate continuous subsonic expansion. The findings suggest that, GF poses no positive benefit on NFL.

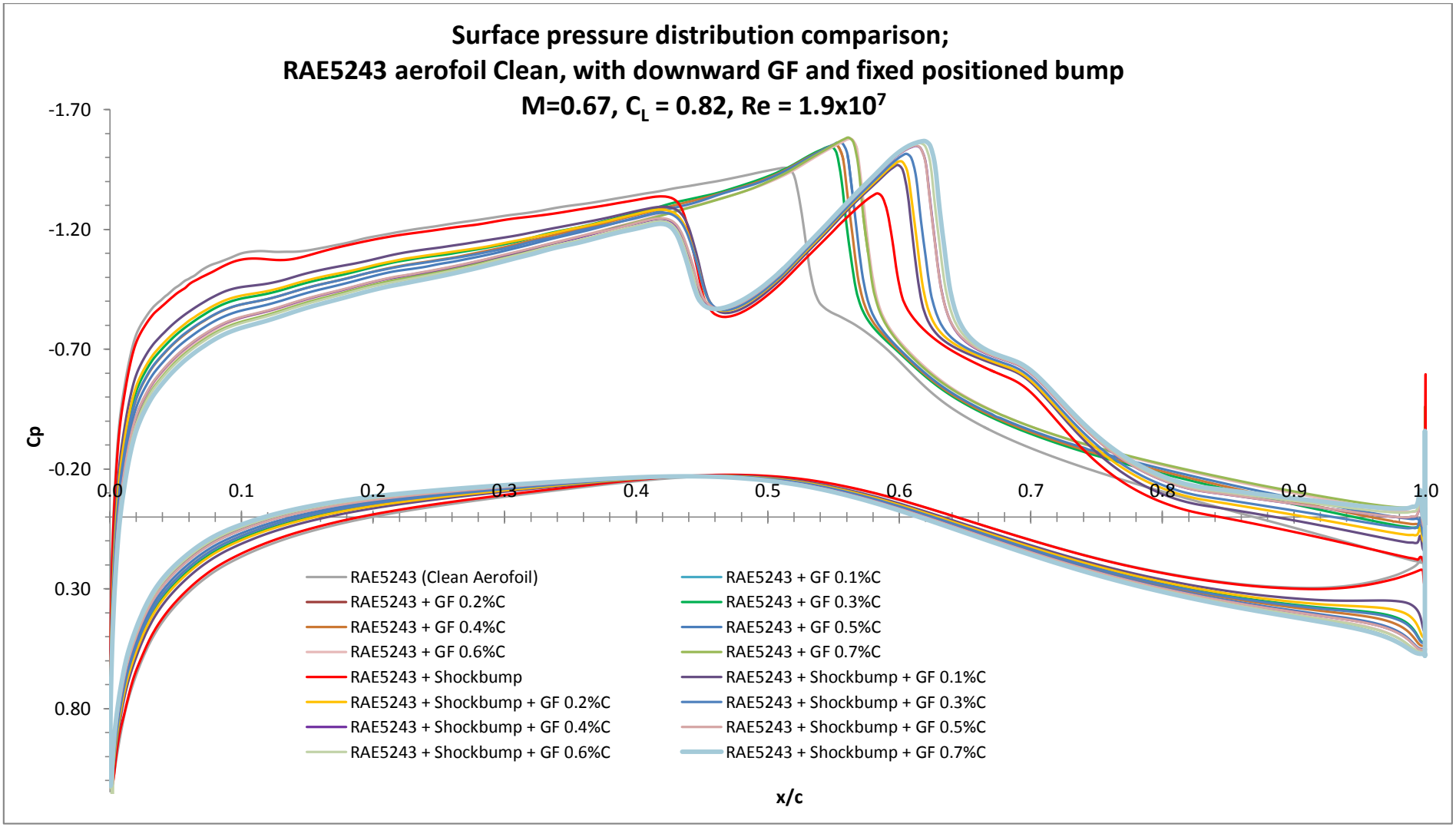

Figure 4.4.1a C_p, Surface pressure distribution RAE5243 with flow control devices **a)** @M = 0.67

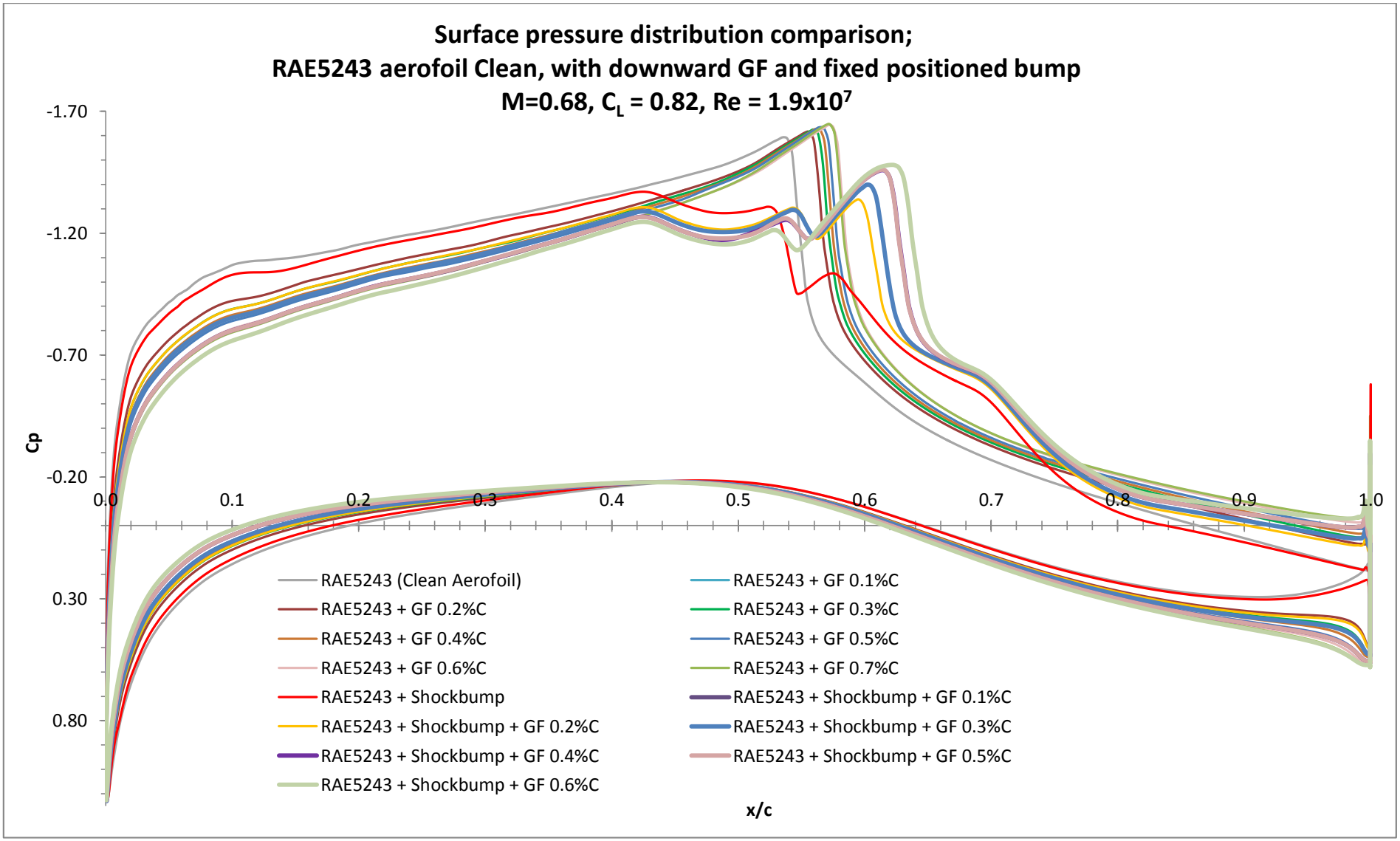

Figure 4.4.1b C_p, Surface pressure distribution RAE5243 with flow control devices **b)** @M = 0.68

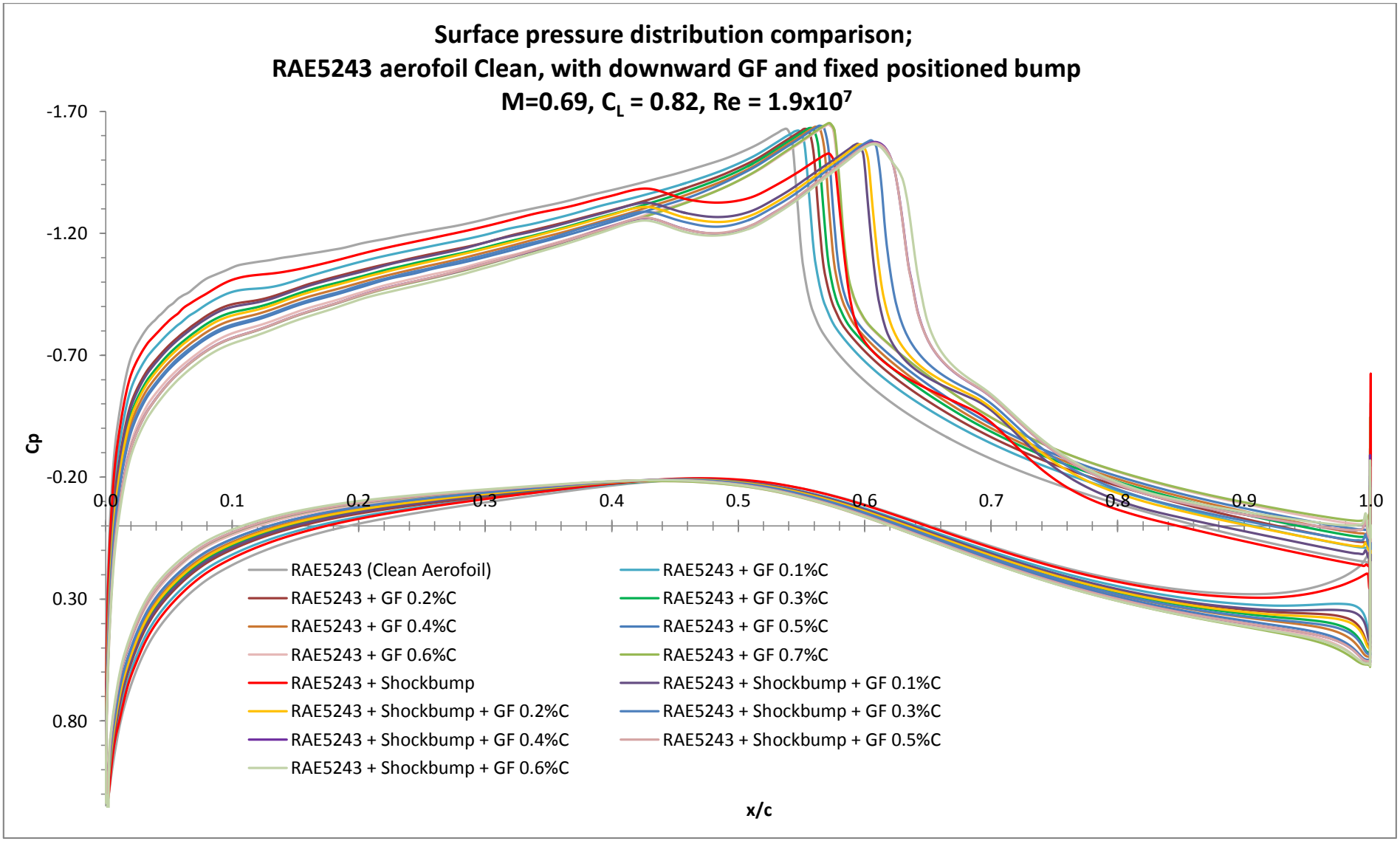

Figure 4.4.1c C_p, Surface pressure distribution RAE5243 with flow control devices **c)** @M = 0.69

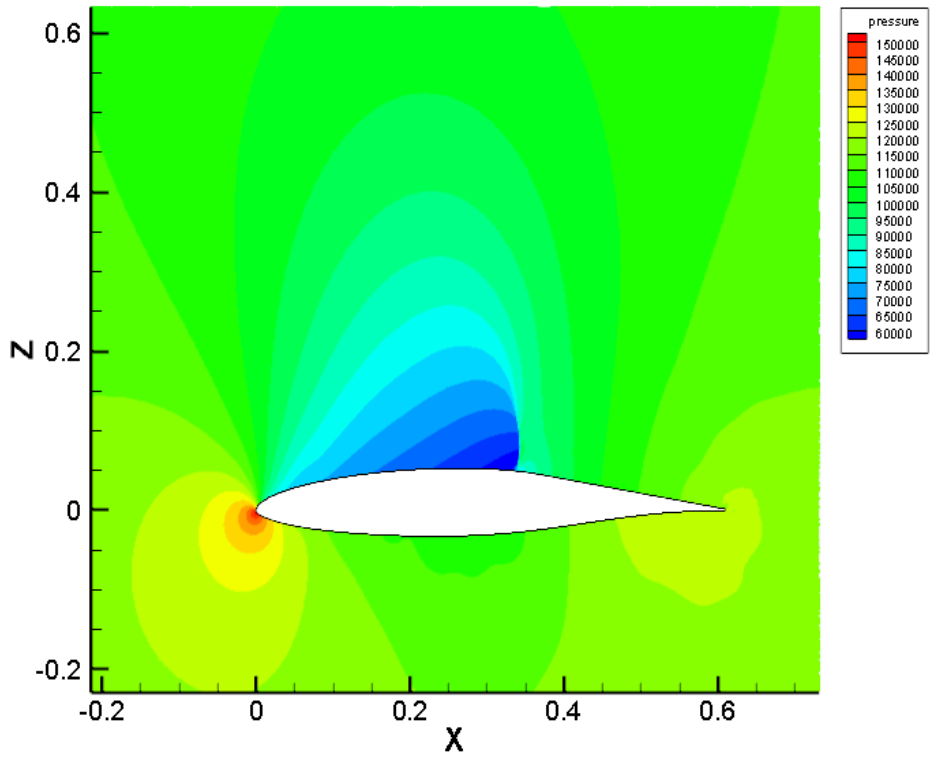

Figure 4.4.2a **Pressure Contour plots, RAE5243 @M = 0.67, C_L = 0.82, Re = 19 x 10^6 (a) overview**

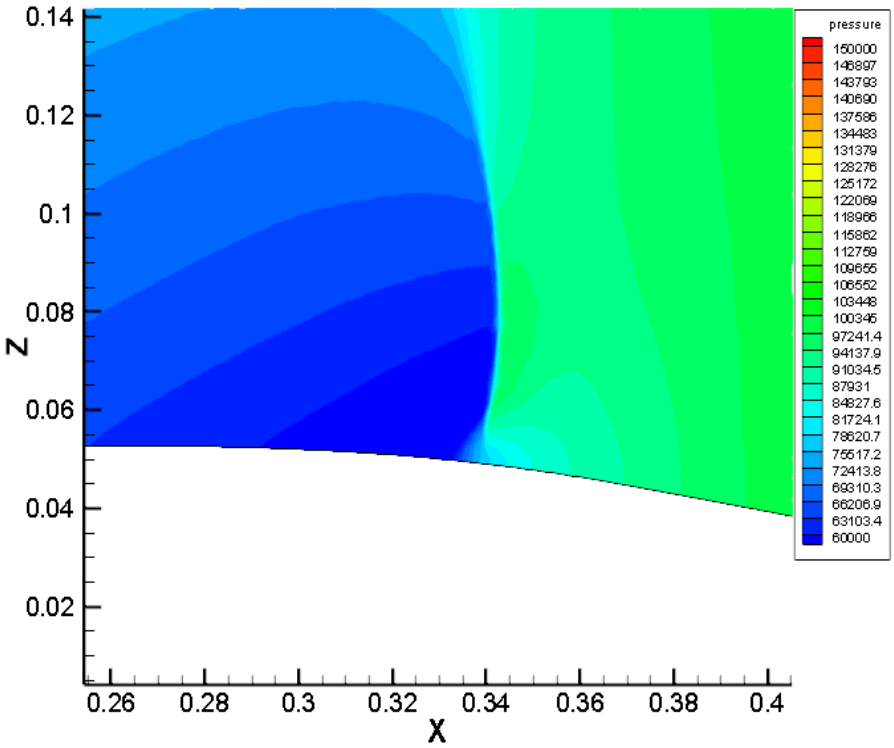

Figure 4.4.2b **Pressure Contour plots, RAE5243 @M = 0.67, C_L = 0.82, Re = 19 x 10^6 (b) shock location**

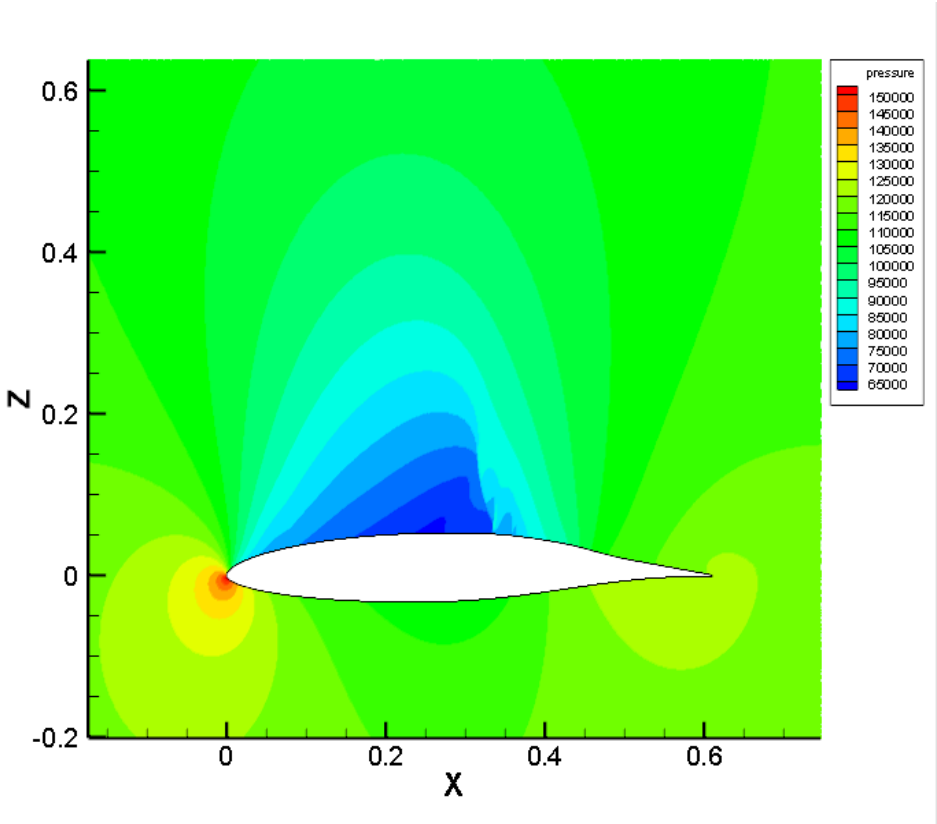

Figure 4.4.3a Pressure Contour plots, RAE5243 with Shockbump @M = 0.67, C_L = 0.82, Re = 19 x 10^6 (a) overview

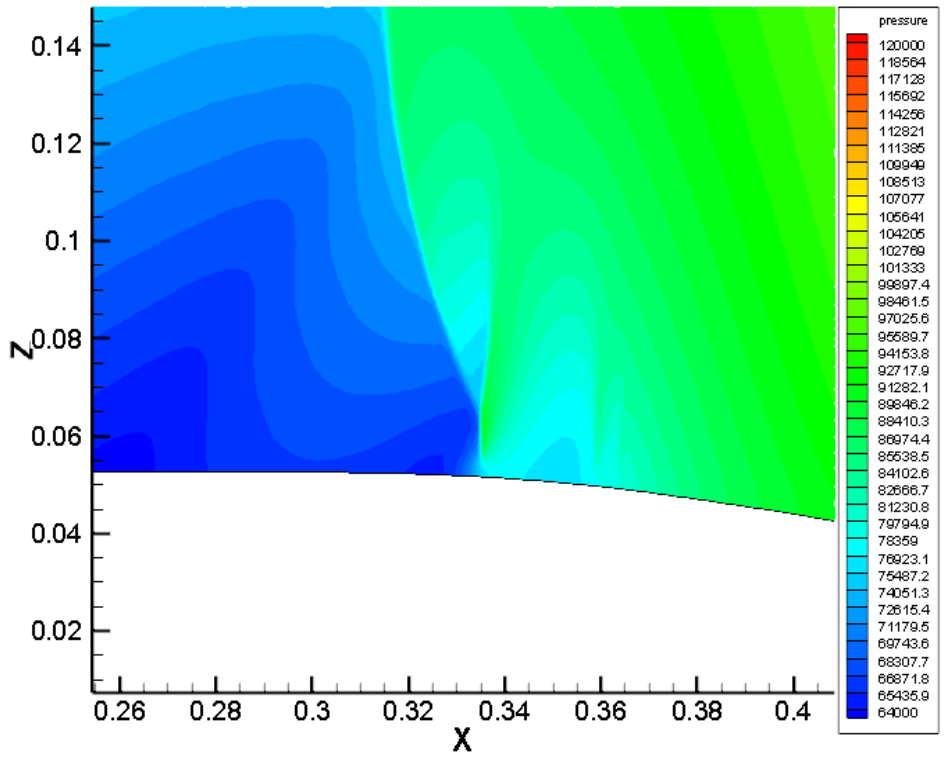

Figure 4.4.3b Pressure Contour plots, RAE5243 with Shockbump @M = 0.67, C_L = 0.82, Re = 19 x 10^6 (b) shock location

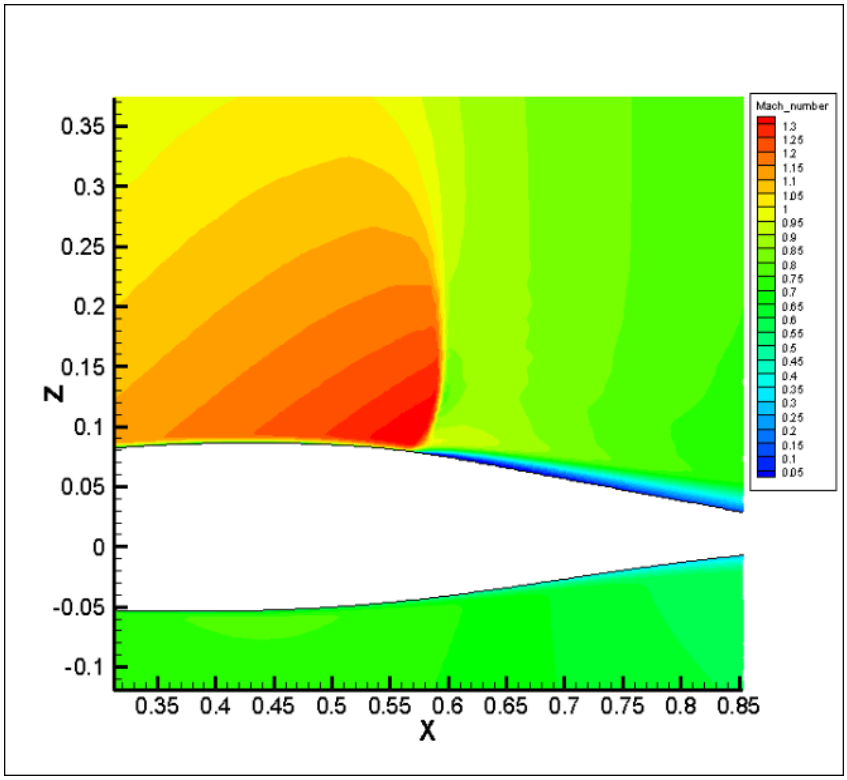

Figure 4.4.4a Mach Contour plots RAE5243 Clean @M = 0.69, C_L = 0.82, Re = 19 x 10^6

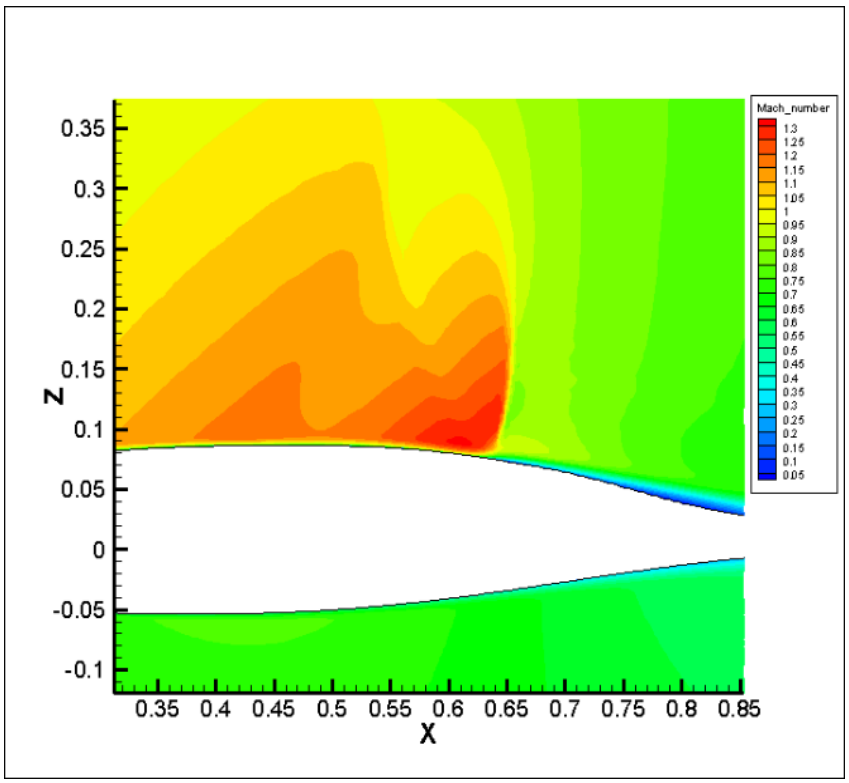

Figure 4.4.4b Mach Contour plots RAE5243 + 0.4%C GF + SB @M = 0.69, C_L = 0.82, Re = 19 x 10^6

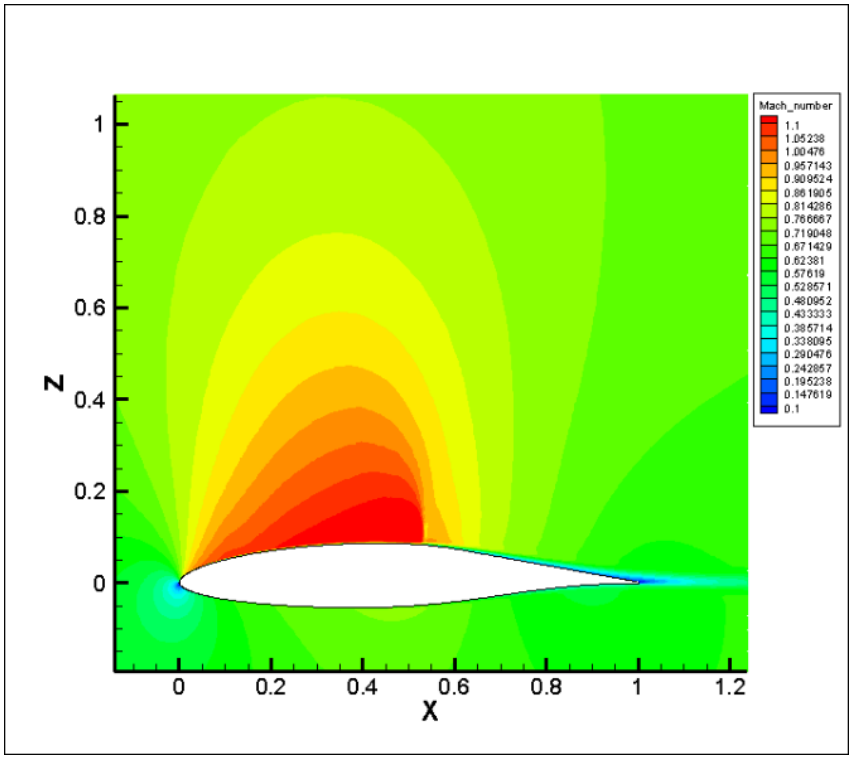

Figure 4.4.5a Mach number Contour plots, RAE5243 Clean @M = 0.67, C_L = 0.82, Re = 19 x 10^6

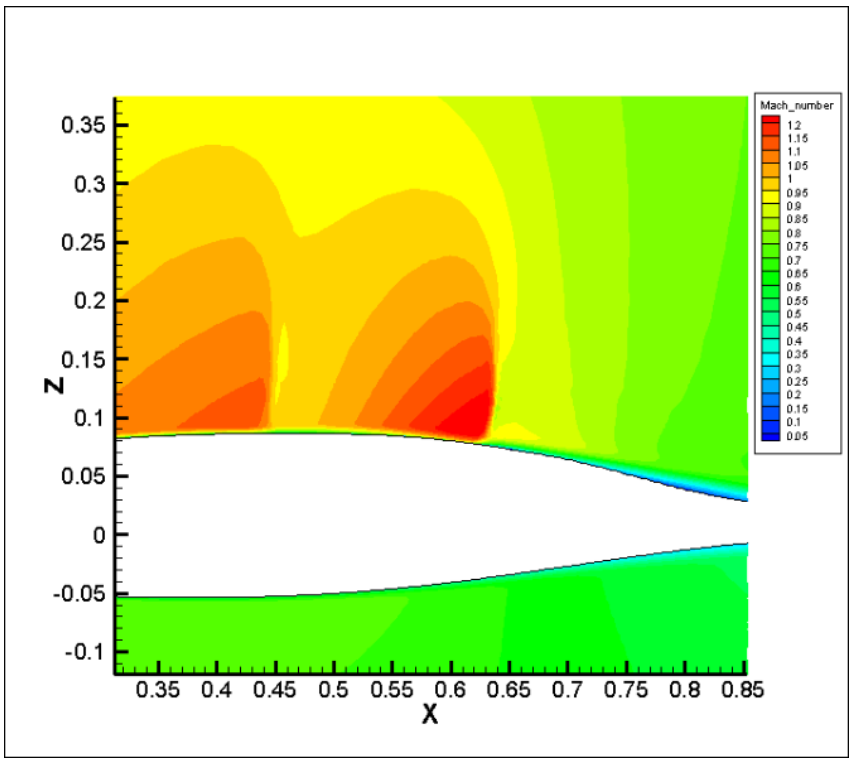

Figure 4.4.5b Mach number Contour plots, RAE5243 with Shockbump @M = 0.67, C_L = 0.82, Re = 19 x 10^6

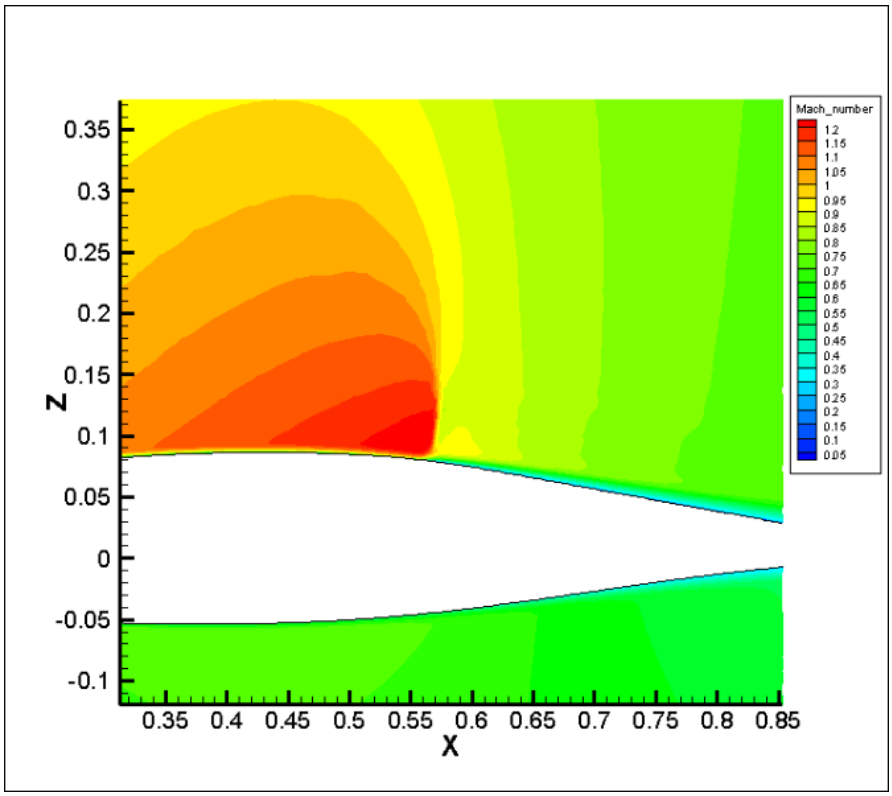

Figure 4.4.5c Mach number Contour plots, RAE5243 with GF 0.4%C @M = 0.67, C_L = 0.82, Re = 19 x 10^6

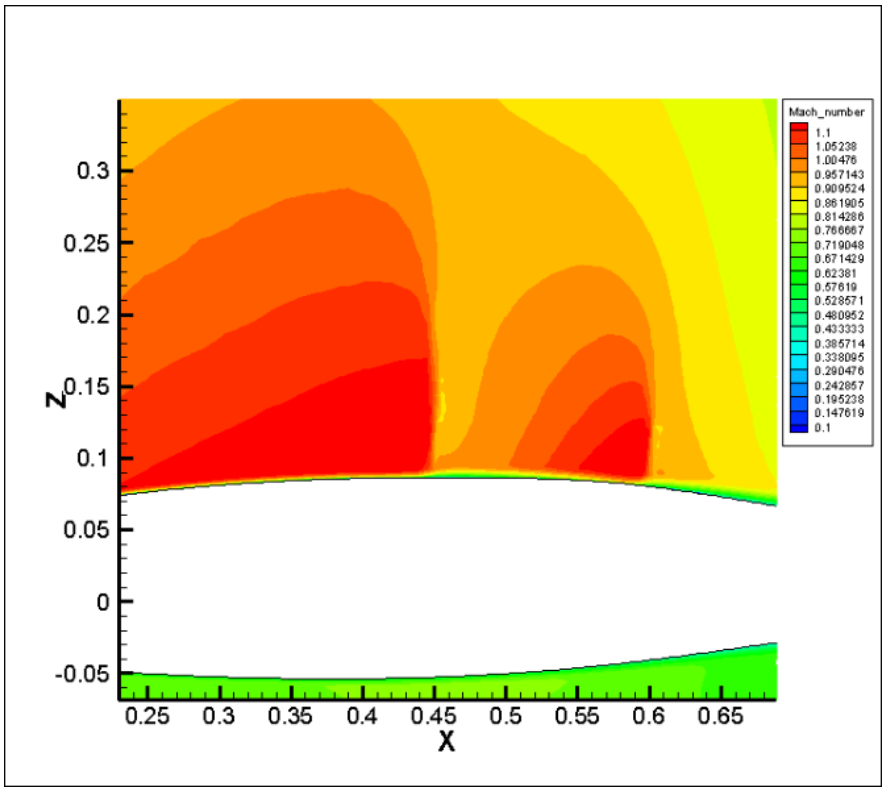

Figure 4.4.5d Mach number Contour plots, RAE5243 with shockbump + GF 0.4%C @M = 0.67, C_L = 0.82, Re = 19 x 10^6

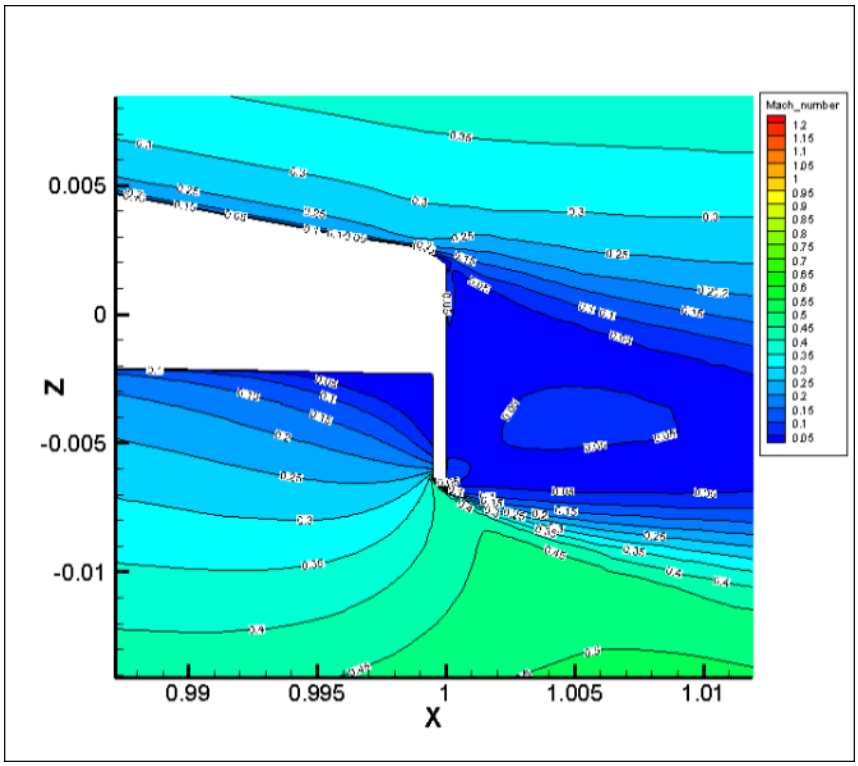

Figure 4.4.5e **Mach number Contour plots at trailing edge, RAE5243 with GF 0.4%C @M = 0.67, C_L = 0.82, Re = 19 x 10^6**

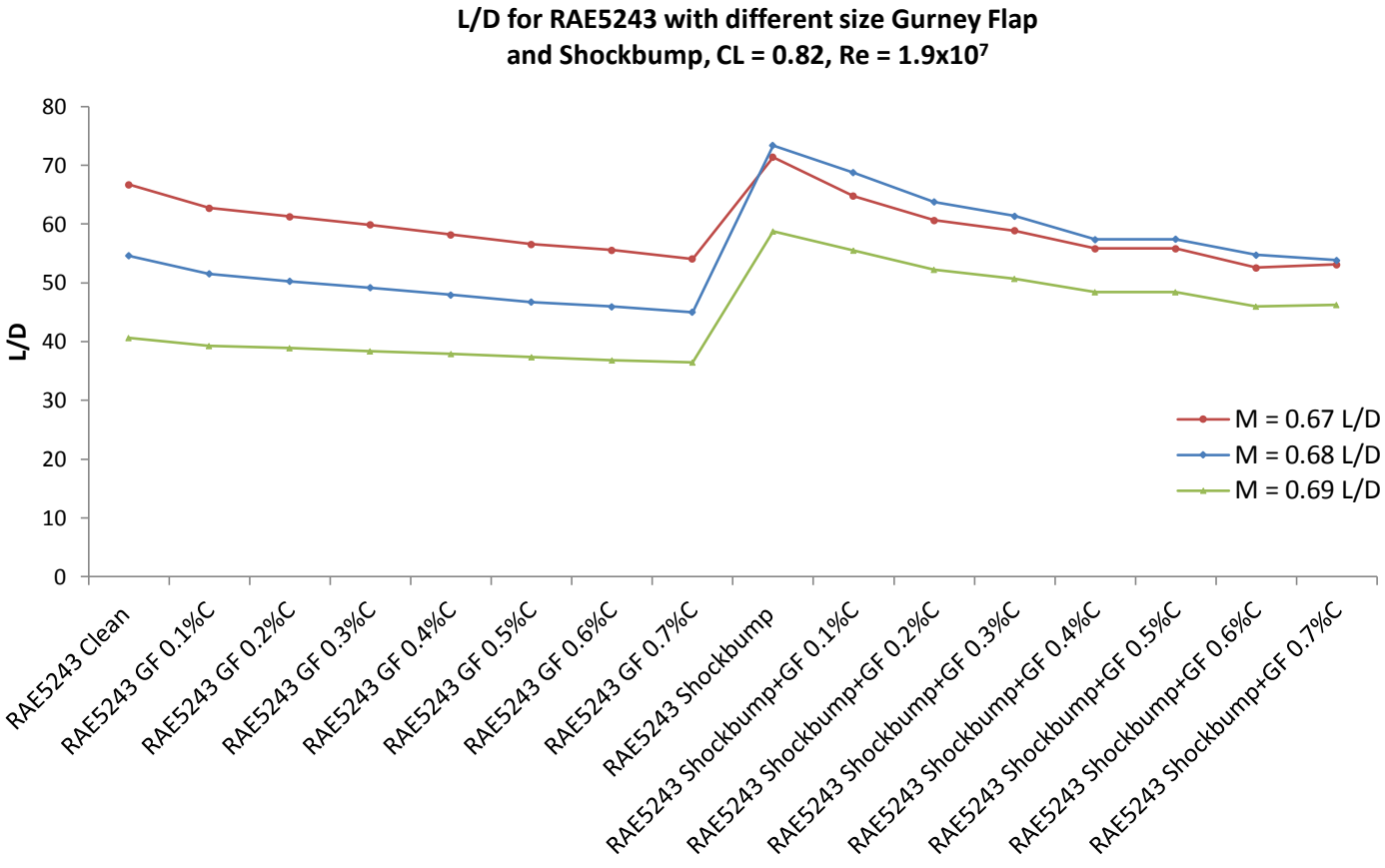

Figure 4.4.4 L/D for RAE5243 with GF, Shockbump, and Shockbump + GF at M = 0.67, 0.68 and 0.69.

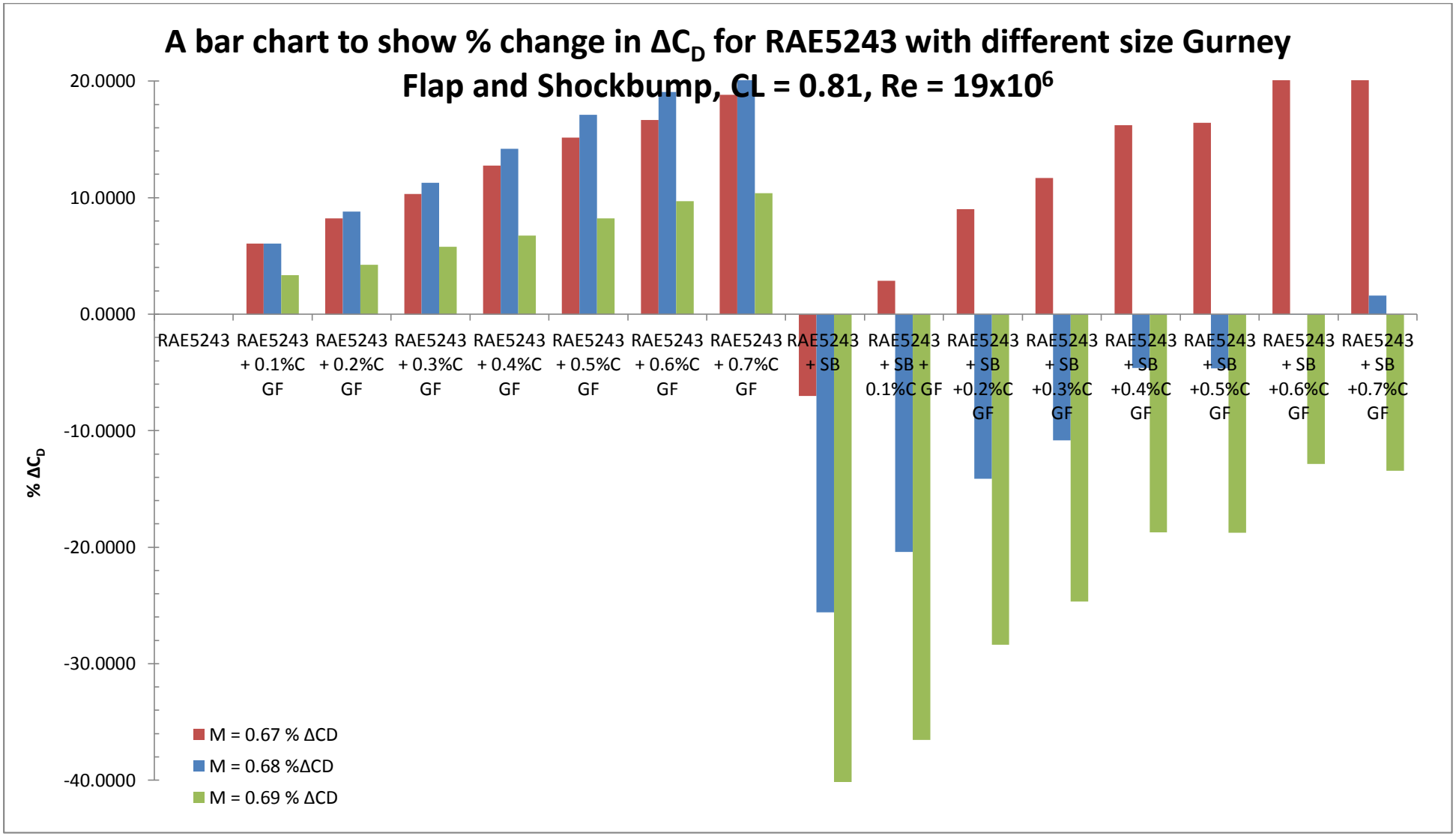

Figure 4.4.6 Percentage change in drag with additional flow control devices in comparison with the Clean aerofoil

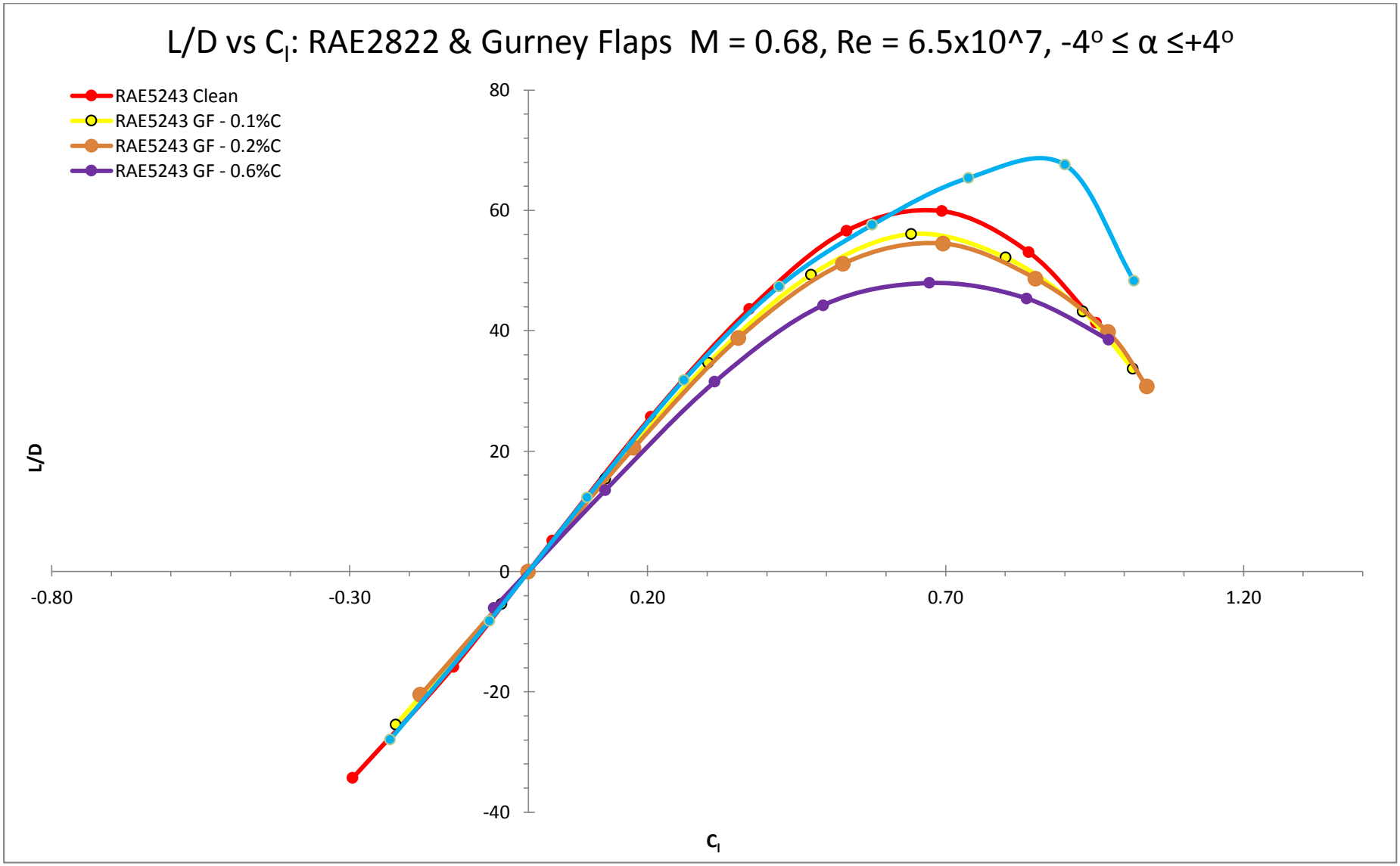

Figure 4.4.7 Lift-to-drag ratio vs C_L for RAE5243, M=0.68, Re = $6.5x10^6$, $-4^o \leq \alpha \leq +4^o$

5. Conclusion

In both Supercritical and NLF aerofoil studies, it was identified that the addition of a Gurney flap during transonic conditions will result in an increase of lift and delay the shock occurrence location on the aerofoil. The delay of shock is caused by the effective camber alteration induced by the Gurney flap (i.e. it changed the effective angle of attack), this will ultimately lead to a reduction in pressure drag. However, the lift force is increased due to the increased surface. This implies the potential of bigger shockwaves. Therefore, a shockbump may be a good solution in attempting to reduce the negative factors from a Gurney flap. However, the shockbump used in this study was pre-determined and optimised for a clean aerofoil.

The effect of a Gurney Flap also suggests a nose down pitching moment and this function is caused by the alteration of the effective camber. In the Supercritical aerofoil case, a Gurney Flap with a height as small as 0.1%C can lead to substantial benefits in drag reduction. In the Natural Laminar Flow aerofoil scenario, the addition of a Gurney flap alone to the aerofoil shows no benefits in drag reduction at all. Although the shockwave moves downstream by the GF, the strength of the shock was in fact increased.

The positive effects (drag reduction benefits) can only be achieved during high C_L conditions of supercritical aerofoil; at low C_L conditions the drag penalty is higher than the benefits created. However, in terms of drag reduction benefits, an effective camber modification towards to trailing edge may be more effective than a retro-fit Gurney Flap. Nevertheless, the modification of the camber to an existing aircraft may be impossible, but a retro-fit Gurney flap may be the solution.

To summarise, the GF is not aerodynamically beneficial on NLF aerofoil as it induces a substantial drag penalty. On the other hand, a GF is beneficial on the supercritical aerofoil and reduces the pressure drag caused by the normal shockwave, which lead to improved aerodynamic performance. The data suggests the single point designed shockbump can be rather robust for NLF in comparison to supercritical aerofoil, as drag improvement was recorded in the previous case. For supercritical aerofoil the shockbump only provides the improved feature during designed or higher Mach numbers. It was believed that a GF's shockwave 'delay/moving' feature is beneficial in conjunction with a single point designed SB during off-design. However, this report signifies that during off-designed condition, the addition of a GF demonstrates no improvement in aerodynamic performance at all, but in turn causes further substantial drag penalty.

Based on the results obtained, the authors have reason to believe that the static GF will cause no aerodynamic benefits if applied to a supercritical aerofoil with multi-point optimised shockbump. However, by taking into account the effective camber alteration and shockwave delaying features of the Gurney flap, a variable angle GF can feature the mentioned functions and provide the user with more control and flexibility. The variable angle GF is predicted to improve the robustness and improve flow characteristics on supercritical aerofoil features shockbump. This is because at the off-designed condition, the shockwave is either in front of or after the bump, which induced further drag penalty, whereas the addition of a variable angle GF can alter its angle to change its effective camber, this can shift the shockwave to a desirable location.

6. Future Work

The future work will include optimisation of Gurney flaps (multi parameter), further investigation with shockbump and Vertical Tail Plane analysis. The study will begin at a specific design condition, then gradually move onto a several off-design conditions to create a more robust system, e.g. multi-point optimisation (various Mach + Reynolds condition). The distinctive "shock moving" feature of Gurney flaps will be combined with the shock weakening feature of Shockbump. This attempts to further reduce shock penalties. In general, Shockbump devices are usually rigid and optimised at a specifically designed cruise condition. However, in off-design conditions, the shock position would differ and the effects of the shockbump will be removed. This report shows the Gurney flap has the ability to adjust shock position and strength. The robustness and feasibility of the shockbump device would increase when integrated with a movable Gurney flap. Also, shockbump may tackle the negative effect of a Gurney flap in transonic conditions.

The application of Gurney flaps and Divergence Trailing Edge on a vertical stabilizer is expected to enhance rudder performance. Therefore, investigations on such a topic would be beneficial. Mini flaps are installed at the trailing edge of both upper and lower surfaces (as it is symmetrical aerofoil). This is an attempt to reduce the surface area of a vertical tail plane whilst retaining its rudder performance. If successful, this will reduce weight and cost penalties. With current findings, it is expected that the side force would increase (side force can be represented as lift). Typical aircraft may only require a specific force produced by the vertical stabilizer to balance/ control the yaw motion. This means with additional Gurney flaps or trailing edge modification, the effectiveness of the rudder would increase. As a result, a smaller vertical stabilizer with tailing edge modification can provide the same effectiveness, but with less weight and less material used. This in turn means that

smaller fin will be needed to provide the same force, and weight will be reduced. Hence, this will provide financial gain to the aircraft operators.

Other geometry or alternative forms (i.e. jets, plasma actuator) of Gurney flap will be investigated in the future. The use of active Gurney flaps in conjunction with shockbump is also an interesting topic, as both can have positive benefits in shock reduction. The feasibility of such a study and multi-point optimisation will be looked at in due course.

7. References

[1] Houghton, E.L., Carpenter, P.W., Collicott, S.H., Valentine, D.T. Aerodynamics for Engineering Students (6th Edition). Butterworth-Heinemann: Elsevier Ltd; 2013. ISBN 978-0-08-096632-8

[2] Liebeck R.H. Design of subsonic airfoils for high lift. AIAA Journal of Aircraft 1978;15(9): 547-61

[3] Jeffrey D, Zhang X, Hurst DW. Aerodynamics of Gurney flaps on a single-element high-lift wing. AIAA Journal of Aircraft 2000; Vol. 37(2):295-301.

[4] Jeffrey D, Zhang X, Hurst DW. Some aspects of the aerodynamics of Gurney flaps on a double-element. ASME, Journal of Fluids Engineering 2001;123:99-104

[5] Storms B.L., Jang C.S., Lift Enhancement of an Airfoil Using a Gurney Flap and Vortex Generators. AIAA Journal of Aircraft 1994; Vol. 31(3)

[6] Myose R, Papdakis M, Heron I. Gurney Flap Experiements on Airfoils, Wings, and Reflection Plane Model. AIAA Journal of Aircraft 1998; Vol. 35(2)

[7] Meyer R., Hage W., Bechert D.W., Drag Reduction on Gurney Flaps by Three-Dimensional Modifications. AIAA Journal of Aircraft 2006; Vol. 43(1)

[8] Bloy A.W., Tsioumanis N., Mellor N.T., Enhanced Aerofoil Performance Using Small Trailing- Edge Flaps. AIAA Journal of Aircraft 1997; Vol. 34(4) – Engineering Notes

[9] Neuhart D.H., Pendergraft O.C., A Water Tunnel Study of Gurney Flaps. NASA Technical Memorandum 4071, November 1988

[10] Schuele C.Y., Greenblatt D., Combined Plasma and Gurney Flap Flow Control at Low Flight Reynolds Numbers. AIAA Journal 2010; Vol. 48(11)

[11] Zhang P.F., Liu A.B., Wang J.J., Aerodynamic Modification of a NACA 0012 Airfoil by Trailing-Edge Plasma Gurney Flap. AIAA Journal 2009; Vol. 47(10)

[12] Traub L.W. and Agarwal G.,Aerodynamic Characteristic of Gurney/ Jet Flap at Low Reynolds Numbers. AIAA Journal of Aircraft 2008; Vol 45(2)

[13] Cook, P. H., McDonald, M. A., and Firmin, M. C. P., Aerofoil RAE-2822 Pressure Distribution and Boundary Layer and Wake Measurements, AGARD Advisory Report 138, 1979

[14] Yu, T., Wang, J.J. and Zhang, P.F., Numerical Simulation of Gurney Flap on RAE2822 Supercritical Airfoil. 2011, AIAA Journal of Aircraft Vol. 48, No. 5

[15] Zaparka E.F., US Patent US1893064, AIRCRAFT, 3rd Jan,1933

Zaparka E.F., US Patent USRE19412 E, Aircraft and Control Thereof, 1st Jan, 1935

[16] Gregg R.D. and Henne P.A., US Patent EP0373160 B1, Divergent trailing-edge airfoil, 25th May, 1994

[17] Rosemann H., Richer K., Gurney Flaps in Transonic Flows, IUTAM Symposium Transsonicum IV, Fluid Mechanics and its Applications Volume 73, 2003, pp 165 -170

[18] Boyd J.A., Lockheed Corporation, Calif., US Patent 452868, Trailing Edge Device for an Airfoil, 24th September, 1985

[19] Wilcox D.C., Turbulence modelling for CFD, DCW Industries Inc., 1993

[20] Gad-el-Hak M. Flow Control: Passive, Active and Reactive flow management. Cambridge: Cambridge University Press; 2000. ISBN 0-521-7706-8

[21] http://quizlet.com/13250967/3d-lift-and-drag-flash-cards/

[22] Kroo I.M., Aerodynamic Concepts for Future Aircraft. AIAA Applied Aerodynamics Conference 1999, AIAA Paper No 99-3524

[23] Bloy A. W., Durrant M.T., Aerodynamic Characteristics of an Aerofoil with small Trailing Edge Flaps. Wind Engineering 1995, Vol 19(3)

[24] Giguere P., Lemay J., Dumas G., Gurney Flap Effects and Scaling for Low-Speed Airfoils. AIAA Paper 1995, No 95-1881

[25] Niu Y.Y., Hsu T.S., Hsieh C.T., Chang C.C., Chu C.C., How Does a Gurney Flap Enhance the Aerodynamics Forces. AIAA Journal 2010; Vol 48(11)

[26] Myose R., Papadakis M., Heron I., Gurney Flap Experiments on Airfoils, Wings, and Reflection Plane Model. AIAA Journal of aircraft 1998; Vol 35(2)

[27] Maughmer M.D., Bramesfield G., Experimental Investigation of Gurney Flaps. AIAA Journal of Aircraft 2008; Vol 45(6)

[28] Lee T., Aerodynamic Characteristics of Airfoil with Perforated Gurney-Type Flaps. AIAA Journal of Aircraft 2009; Vol 46(2)

[29] Lovely D, Haimes R., Shock Detection from Computational Fluid Dynamics Results. 1999, AIAA Paper 99-3285

[30] Yu H.C.R, Qin N., Effects of Gurney Flap and Shock Bump on Supercritical and NLF Transonic Aerofoil, RAeS Applied Aerodynamics Conference, UK, 2014

[31] DLR, TAU-Code Release 2012.1.0, Technical Report, Institute of Aerodynamics and Flow Technology, Braunschweig

[32] Spalart, P.R., Allmaras, S.R., A One-Equation Turbulence Model for Aerodynamic Flows, AIAA Paper 1992-0439, 1992

[33] Spalart, P.R., and Rumsey, C.L., Effective Inflow Conditions for Turbulence Models in Aerodynamics Calculations, AIAA Paper 2007-2544, 2007

[34] The Supercritical Airfoil, NASA Technology Facts, TF-2004-13 DFRC, http://www.nasa.gov/pdf/89232main_TF-2004-13-DFRC.pdf

[35] Qin, N., Wong, W.S., and Le Moigne, A., 3D contour bumps for transonic wing drag reduction, IMechE Proc. Part G: J. Aerospace Engineering, Vol. 222, (2008)

[36] Fulker, J.L. and Simmons, M.J. An experimental study of shock control methods. DRA/ AS/ HWA /TR94007/1,199

[37] Lee D. and Periaux J., TA5: Shock control Bump Optimization on a transonic laminar flow airfoil. Database Workshop for Multiphysics Optimization Software Validation, University of Jyvaskyla, December 3-2, 2009

[38] Wong, W.S., Qin, N., Sellars, N., Holden and H., Babinsky, H., A combined experimental and numerical study of flow structures over 3D shock control bumps, 2008, Aerospace Science and Technology 12 (2008) 436-447

[39] Rathakrishnan, E. Theoretical Aerodynamics, John Wiley & Sons, 2013, ISBN: 978-1-118-47937-7

[40] Abbott, I. H., Von Doenhoff A. E., Theory of Wing Sections Including a Summary of Airfoil Data, Dover Publications, 1959, Standard Book number: 486-60586-8